MINISTÉRIO DA EDUCAÇÃO
UNIVERSIDADE FEDERAL DO RIO GRANDE DO SUL
PROGRAMA DE PÓS-GRADUAÇÃO EM ENGENHARIA MECÂNICA

ANALYTICAL DEVELOPMENT OF A MECHANICAL MODEL FOR THREE DIMENSIONAL RODS USING THE SPATIAL BEAM THEORY

por

Filipe Paixão Geiger

Dissertação para obtenção do Título de
Mestre em Engenharia

Porto Alegre, Agosto de 2016.

Desenvolvimento Analítico de um Modelo Mecânico para Membros Esbeltos Tridimensionais Utilizando a Teoria de Vigas Espaciais

por

Filipe Paixão Geiger

Engenheiro Mecânico

Dissertação submetida ao Corpo Docente do Programa de Pós-Graduação em Engenharia Mecânica, PROMEC, da Escola de Engenharia da Universidade Federal do Rio Grande do Sul, como parte dos requisitos necessários para a obtenção do Título de

Mestre em Engenharia

Área de Concentração: Mecânica dos Sólidos

Orientador: Prof. Dr. Rogério José Marczak

Aprovada por:

Prof. Dr. Felipe Tempel Stumpf ..... FURG/ Rio Grande

Prof. Dr. Jakson Manfredini Vassoler ..... PROMEC - UFRGS/ Porto Alegre

Prof. Dr. Ignacio Iturrioz ..... PROMEC - UFRGS/ Porto Alegre

Prof. Dr. Jakson Manfredini Vassoler
Coordenador do PROMEC

Porto Alegre, 31 de Agosto de 2016.

ACKNOWLEDGEMENTS

I would like first to thank my professor advisor Prof. Dr. Rogério José Marczak for the time invested in me in every answer and for steering me in the right direction whenever needed.

I thank the CNPQ for the financial support during the master's degree, the Universidade Federal do Rio Grande do Sul for the opportunity to obtain this title and the evaluation board Prof. Dr. Felipe Tempel Stumpf, Prof. Dr. Jakson Manfredini Vassoler and Prof. Dr. Ignacio Iturrioz for the comments and contributions during the work review.

My gratitude to my family and friends for the support, encouragement and patience throughout this work development. A special thanks to my colleges from GMAp for the help. Without you this would never be possible.

Finally my profound gratitude to Eng. Ana Carolina Langone for being on my side in every moment no matter how difficult. You are an example to me. Thank you for every thing you did to make this venture become true.

ABSTRACT

A high number of structures uses cables due to their ability to bear large load in the longitudinal direction, for example, prestressed concrete, offshore systems and bridges. Its basic structure is formed by a central straight element surrounded by strands laid helically. A variety of geometries can be used, as well as the number of layers. Using the theory of spatial beams and parameterizing the geometry, the center line of only one of these helixes was analyzed analytically, since contact and slip are not included in this theory, obtaining a first approach in order to model these structures and to determine its mechanical behavior. Thus, the equilibrium equations were deduced and the differential system was solved with the objective of representing the mechanical behavior of the structure. Using the Frenet-Serret triad to define a local coordinate system, the boundary conditions were applied aiming the determination of the integration constants. The expressions obtained were compared with results obtained by the Finite Element Method (FEM) for validation applying concentrated and distributed loads. All cases presented good agreement FOR forces, moments, rotations and displacements. Considering the arc case, its radius was increased until a straight beam. The proposed model was also used to simulate a spring under compression.

Keywords: Spatial Beam Theory; Curve Parameterization; Differential Geometry; Rod.

RESUMO

A principal característica de cabos é a sua capacidadede suportar grande carga na direção longitudinal e são utilizadas em, por exemplo, concreto comprimido, plataformas e pontes. Usualmente, sua estrutura básica é formada por um elemento central (núcleo) e reto juntamente com outros componentes dispostos ao seu redor em forma de hélice. Existe uma variedade de geometrias que podem ser utilizadas, assim como número de camadas. Seguindo a teoria de vigas espaciais e parametrizando a geometria, a linha média de apenas uma dessas hélices foi analisada analiticamente. Essa simplificação é valida visto que o contato e deslizamento não são incluídos nesta teoria, produzindo uma primeira abordagem ao problema da modelagem dessas estruturas. Sendo assim, as equações de equilíbrio foram deduzidas e seu sistema diferencial foi resolvido com o objetivo de representar o comportamento mecânico da estrutura. Utilizando a tríade de Frenet-Serret para definir um sistema de coordenadas local, as condições de contorno foram aplicadas buscando determinar as constantes de integração resultantes da solução analítica das equações diferenciais. Essa solução foi comparadas com resultados numéricos obtidos pelo Método dos Elementos Finitos (FEM) para validação dos casos de carga concentrada e distribuída em duas geometrias, o arco plano e a hélice. Em ambos os casos resultados apresentaram boa concordância para forças, momentos, rotações e deslocamentos. Considerando o caso do arco, o seu raio foi aumentado, de forma que a geometria se aproximasse de uma viga reta. O modelo proposto também foi utilizado para simular uma mola sob compressão.

Palavras-chave: Teoria Espacial de Vigas; Parametrização de Curvas; Geometria Diferencial; Cabos.

CONTENTS

LIST OF FIGURES

LIST OF TABLES

ABBREVIATION LIST

BC	Boundary Condition
FEM	Finite Element Method
FS	Frenet- Serret

LIST OF SYMBOLS

$\boldsymbol{b}(S)$	Binormal vector
$\frac{d(\boldsymbol{b}(S))}{dS}$	Binormal vector variation
C_1	Force constant of integration, N
C_2	Force constant of integration, N
C_3	Force constant of integration, N
C_4	Moment constant of integration, Nm
C_5	Moment constant of integration, Nm
C_6	Moment constant of integration, Nm
C_d	Relation between diameters D_i and d
d	Wire diameter, m
D_i	Internal diameter of the spring, m
E	Elastic modulus, MPa
$\mathbf{F}$	Applied load vector, N
F_{arc}	Arc local load, N
F_{helix}	Helix local load, N
F_{local}	Local applied load, N
G	Shear modulus, GPa
I	Moment of inertia, m^4
J	Polar moment of inertia, m^4
$m(S)$	Distributed moment, Nm/m
M_{arc}	Arc moments, Nm
M_{BC_L}	Reaction moments, Nm
M_{helix}	Helix moments, Nm
M_1	Moment component acting in $\boldsymbol{t}$, Nm
m_1	Distributed moment aligned to $\boldsymbol{n}$, Nm/m
M_2	Moment component acting in $\boldsymbol{n}$, Nm
m_2	Distributed moment aligned to $\boldsymbol{n}$, Nm/m

M_3	Moment component acting in $\boldsymbol{b}$, Nm
m_3	Distributed moment aligned to $\boldsymbol{b}$, Nm/m
$\boldsymbol{n}(S)$	Normal vector
N_{arc}	Arc forces, N
N_{helix}	Helix forces, N
N_1	Force component aligned to $\boldsymbol{t}$, N
N_2	Force component aligned to $\boldsymbol{n}$, N
N_3	Force component aligned to $\boldsymbol{b}$, N
N_a	Internal force acting in point a, N
N_b	Internal force acting in point b, N
$\frac{d(\boldsymbol{n}(S))}{dS}$	normal vector variation
P	Pitch, m
$\mathbf{q}$	Distributed load vector, N/m
$q(S)$	Global distributes load, N/m
q_1	Distributed load aligned to $\boldsymbol{t}$, N/m
q_2	Distributed load aligned to $\boldsymbol{n}$, N/m
q_3	Distributed load aligned to $\boldsymbol{b}$, N/m
Q_x	Distributed load reaction aligned to $\boldsymbol{t}$, N/m
Q_y	Distributed load reaction aligned to $\boldsymbol{n}$, N/m
Q_z	Distributed load reaction aligned to $\boldsymbol{b}$, N/m
R	Cable radius, m
r	Strand radius, m
$\boldsymbol{r}(S)$	Parameterization position vector, m
R^{GLOBAL}	Global generalized effect
R^{LOCAL}	Local generalized effect
R_c	Core radius, m
R_e	Eccentricity of applied load, m
S	Helix local coordinate, m
S_{max}	Maximum local coordinate, m
$\boldsymbol{T}$	Transformation matrix
$\boldsymbol{t}$	Tangent vector

$\boldsymbol{T}_{arc}$	Arc transformation matrix
$\boldsymbol{T}_{FS}$	Frenet-Serret geometric properties matrix, m^{-1}
$\boldsymbol{T}_{helix}$	Helix transformation matrix
$\frac{d(\boldsymbol{t}(S))}{dS}$	Tangent vector variation
$\boldsymbol{u}_0$	Displacement constant of integration vector, m
u_1	Displacement component in the x_1 direction, m
u_2	Displacement component in the x_2 direction, m
u_3	Displacement component in the x_3 direction, m
V_x	Applied load aligned to x_1, N
V_y	Applied load aligned to x_2, N
V_z	Applied load aligned to x_3, N
$x_1(S)$	Parameterized position in the x_1 axis, m
$x_2(S)$	Parameterized position in the x_2 axis, m
$x_3(S)$	Parameterized position in the x_3 axis, m
y	Stress calculated position in the cross section, m
α	helix angle, $^\circ$
$\boldsymbol{\eta}$	Forces vector, N
κ	Curvature, m^{-1}
$\boldsymbol{\nu}$	Moments vector, Nm
$\boldsymbol{\phi}_0$	Rotation constant of integration vector, $^\circ$
ϕ_1	Rotation component in the x_1 direction, $^\circ$
ϕ_2	Rotation component in the x_2 direction, $^\circ$
ϕ_3	Rotation component in the x_3 direction, $^\circ$
ψ_{23}	Position matrix in equilibrium equation
ρ_1	Deflection component acting in $\boldsymbol{t}$
ρ_2	Deflection component acting in $\boldsymbol{n}$
ρ_3	Deflection component acting in $\boldsymbol{b}$
σ_{sh}	Spring maximum shear stress, MPa
θ	Angle in x_1x_2 plane, $^\circ$
θ_{max}	Angle in the final position S_{max}, $^\circ$
ε_1	Torsion Strain

ε_2	Strain in the x_2 direction
ε_3	Strain in the x_3 direction
ξ	Curvature adjustment

1. INTRODUCTION

1.1 Motivation

The capacity to support a great amount of axial load combined with the high flexibility are cables properties. The efficient material appliance, i.e., the satisfactory force per weigh relation is another characteristic that can be highlighted. Therefore, several applications use these components in different engineering areas, either in mechanical or civil, as stayed bridges, lifts, prestressed concrete cranes and others. Such components, during their lifespan, are subjected not only to static loads, but also to dynamic, or cyclic, forces that can lead to premature degradation and cracks associated to corrosion and fatigue. As a result, determining the mechanical behavior of cables is necessary to predict operation conditions. The correct design, hence, is fundamental to ensure the safety of users and avoid failure during its employment. Due to this versatility, different geometries can be used, thus there are several variables to be determined to set the best configuration for every function.

For a certain period, the theories evolution applied to the determination of the cable design was based in experiences and experiments, through observation, leading to empirical formulations, according to Cardou e Jolicoeur, 1997. Therefore, mathematical and mechanical approaches are essential to decrease the need for experiments, since they are not only expensive but also specific, i.e., every parameter or work condition are a variable of the test. This kind of structure can have a large scale factor which means that specific and overpriced equipment, that may not exist, is necessary [Ghoreishi et al., 2007b]. Furthermore, every geometry must be studied together with the working condition.

In this context, the analysis using numerical tools as the Finite Element Method (FEM) is a viable alternative in an early step of the project. However, complex models may have a high computational cost. In order to perform appropriate and precise simulations may be necessary to consider some requirements, such as nonlinear effects. As a consequence, mesh generation and other aspects could have a higher computational cost, increasing significantly the time of analysis [Páczelt e Beleznai, 2011].

Once again, in this case, analytical expressions are tools used to avoid this inconveniences. These equations reduce the time of analysis of one geometry, and specially for many cases in a row, also could be used to validate experiments or FEM models which support the

concept project, that is, allows to indicate the mechanical behavior before starting complex studies.

Analytical solutions based *a priori* in kinematics and other hypothesis are available in the literature. Some of these works are described in the next section. Nonetheless, such theories are not fully appropriate to describe the mechanical behavior of application conditions that are subjected to bending and/or torsion, [Argatov, 2011].

In this work an analytic expression is proposed based on the curved beam theory differential system solution. Modeling the cable central element as a straight beam and the strands with the proposed methodology results in an approximate solution for these structures.

1.2 Literature Review

During the last years many developments have been performed in the study of cables. Different theories either friction, contact, Poisson's effect, multi-layers and other hypothesis were considered to model these structures. Also, various approaches were used considering experiments, kinematics, Finite Element Method (FEM), spatial beam theory, etc.

Experimental data is limited and difficult to obtain as highlighted by Spillers et al., 1983. The desired geometry is hard to generate and, even when is reached, several measurements must be performed for each configuration.

Results were obtained by Utting e Jones, 1985, for experiments in a rope with a single layer. Strain gauges were used together with a developed instrument, called by the authors as extrometer, to measure extension and rotation simultaneously.

Utting e Jones, 1987, also performed experiments in straight single steel strands subjected to axial load with different end conditions and lay angles. Also, a model was proposed to represent the change of helix angle, Poisson's effect, flattening and friction presenting good agreement specially for small lay angles.

Analytic expression were obtained by several authors considering different theories. A strand with twisted wires, forming a spring, was analyzed with the proposed theory by Costello e Phillips, 1979, considering large deflections. A small non linearity in tension or compression springs were found for large strains and negligible end condition dependence.

A theory to determine stresses, without friction, in multilayered cables due to axial,

torsion and bending loads were proposed by Costello, 1983. Superposition effects are used to determine stresses due to axial and bending. The center wire endures the maximum tensile stress due to the larger radius and the straight geometry according to the authors.

A model for helical structures based on the spatial beam theory was proposed by Ramsey, 1988. Cases for uniform bending with and without friction, besides uniform extension and twist, were analyzed.

As an evolution from the previously model by Ramsey, 1990, an individual wire in a multilayered cable was treated as a helical structure. The equilibrium equations were used, together with kinematics, as a uniform extension and twisting. Results demonstrated that the only friction possible leads to a radially directed couple.

Geometry called 6×19, consisting in three layer, was studied, by Velinsky, 1985, using the nonlinear equilibrium equations for frictionless bending and twisting. Variables to simulate the strand and each individual wire were used, thus the nonlinear resulting system. This extension of the linear theory did not demonstrate an improvement in results despite the higher computational cost.

A helical wire subjected to bending on a frictionless cylindrical surface was studied by Østergaard et al., 2012. The equilibrium equations of the spatial beam theory were considered to obtain the response of steel cables. Tangential wire rotation is assumed to be governed only by the underlying surface. Bending and tension trend to eliminate the geodesic curvature, i.e., the configuration without it is the limit state.

Axially loaded metallic cables with one layer was investigated and according to Labrosse et al., 2000, the energy dissipated from the friction, determined from the coulomb friction, was used to model the friction between a strand and the core. Friction and wear were shown as negligible. The pivoting model proposed generated results close to other theories where this phenomena is not considered.

Slippage between the considered layer of the cable was investigated near the terminations when subjected to a bending moment. According to Raoof, 1990, results demonstrated the fatigue occurring in the socket and that the first structure to fail was the strand that entered in the neutral bending axis.

Elastic wave propagation in prestressed helical waveguides were analyzed by Treyssède et al., 2013. The translational invariant property was used to reduce the 3D elastody-

namic problem into a two dimensional posed on the deformed cross-section. Results demonstrated that prestressed effect was more significant at low frequencies. The semi-analytical finite element (SAFE) model was used.

Similarlly, static behavior for axial loads were studied by Frikha et al., 2013, using an asymptotic expansion. Three dimensional elasticity problems were reduced, by this methodology, into a 2D microscopic problem in the cross-section and the well-known macroscopic spatial beam problem on the helix. The two dimensions solution was implemented to be used by FEM and proved to be efficient according to the authors.

An independent wire rope core model was proposed by Elata et al., 2004. Axial load and torque were applied in the structure that considers two layers of helices surrounding the straight core. Experimental data was obtained to validate the two kinematics alternative. The methodology can be used for global features determination such as force between wires, rope stiffness and fatigue.

Another approach to study these structure is the Finite Element Method. With the development of computational resources this methodology became highly used. Complex geometries as cables demand the use of a numerical tool without mathematical simplifications [Stanova et al., 2011], specially for non linearities as contact.

Transverse contraction from Poisson's effect along contact was investigated by Argatov, 2011. Local elastic contact deformations considering angles lower than 15° are small, while the flattening is dominant over the Poisson's effect for $\alpha > 25^\circ$. The asymptotic model applied to determine contact between strand-strand and core-strand resulted in a FEM analysis with good results.

According to Jiang et al., 1999, a complete model capable of representing localized non-linearity behaviors, as contact, residual stresses, friction and plastic deformations was developed. Symmetry and precise boundary conditions were applied to simulate tension, shear and torsion in a wire rope.

One layer of helical wires, in contact with the core and other wires, was analyzed using a similar approach by Jiang et al., 2008, with the same $\frac{1}{6}$ symmetry methodology allowing a much more complex model, as mentioned before, with an acceptable computational cost, according to the authors. Contact can happen simultaneously in both places and local deformations should be accounted in theories were conclusions. Also elliptical helix

cross-sectional shape was accurate for lay angles smaller than 20°.

Jiang, 2012, applied the model again considering effects of torsion, shear, bending, torsion, contact, friction and local plastic yielding. Results were compared to analytic solutions and experimental data available, reaching good agreement for global behavior of stress distribution. The simplified model, according to the authors, can provide information regarding nonlinear effects aforementioned.

Large displacements and rotations on curved beans were studied using updated Lagrangian and Total Lagrangian formulations by Bathe e Bolourchi, 1979. A geometric nonlinear element was proposed and both methodologies yield identical element stiffness matrices. However, the first proved to be computationally more effective.

The model proposed by Nawrocki e Labrosse, 2000, allowed the evaluation of all the interwire motions, according to the authors. Contact between strands when subjected to axial load and to axial and bending effects simultaneously, was investigated. Pivoting proved to govern the response for axial load while sliding affects the bending.

Interwire motion, contact and dry friction was analyzed by Páczelt e Beleznai, 2011, using FEM. A p-extension method was applied to obtain a nonlinear formulation in the normal direction. Tension, torsion and bending were considered in the kinematics together with Hertz-theory. A special nonlinear spring element and spring foundation were developed to study the proposed cases.

A comparison between theories was performed by Ghoreishi et al., 2007b. Different methodologies have been proposed to determine the mechanical response of cables. Nine of them were tested considering a stiffness matrix obtained from the coupling between torsion and tension. Results showed a good agreement from the models and 3D FEM analysis for α up to 20°. The difference from the approach increases significantly for higher helix angles. Although Poisson's effect raise the response accuracy, it turns the matrix asymmetric.

1.3 Objectives

In this work it is proposed a model to determine the mechanical behavior of one wire of a cable based on the spatial beam theory.

The mechanical behavior of one helix is analyzed in order to define the model, since the structure is symmetric and the rotation of the results can define the other strands and

the contact between elements is disregarded. Hence, it is necessary to fulfill some specific objectives to obtain the analytic model:

- Characterize one strand by its center line, geometrically defined by the helix parametrization;
- Define a local system to analyze the stress equivalents (force/moment) using the differential geometry;
- Solve the differential equilibrium equations for forces, moments, rotations and displacements;
- Determine the integration constants by the application of the boundary conditions;
- Validate the obtained expressions with FEM.

To complete these objectives the work was divided into sections as follows.

1.4 Work Organization

Differential geometry was used in order to build a helix parameterization. This simplifies the analysis and allows the application of a local system. The transformation to a global system, and back, was also achieved using this theory. The second chapter explores these concepts.

Equilibrium equations of three dimensional spatial beam to be solved are introduced in the third chapter. The parameterized strand, as a helix, was analyzed according to the forces and moments acting on an infinitesimal portion of a spatial beam. With the strains and stresses determined, by applying the kinematics in the Principle of Virtual Work (PVW), another system of equilibrium equations with respect to displacements and rotations were obtained.

With these simplifications, the proposed model was stabilished. Chapter 4 presents the solved system of equations, not only for forces and moments but also for displacements and rotations. This model considered the parameterized geometry obtained previously.

The cable mechanical behavior from the proposed model were compared to numerical results obtained from the Finite Elements Method (FEM). Applying the boundary conditi-

ons, the constants of integration were calculated and then used in the derived expressions. The fifth chapter presents the results.

2. DIFFERENTIAL GEOMETRY

The study of local properties of curves and surfaces is known as differential geometry. The geometric characteristics are those that depend only on the behavior of the structure near a given point. The methodology used to perform this study comes from the differential calculus, according to Do Carmo, 1976. Therefore, the planes and curves analyzed with this technique must be differentiable, or smooth, a certain number of times so that no discontinuity is generated in the region of interest.

The concepts of parameterization are introduced in the following sections along with the necessary properties to completely define and analyze a spatial curve. Then, an example of this theory application is presented for the particular form of a helix.

2.1 Parametrization of Curves

Two points in a space $\mathbb{R}^2$ must necessarily be assigned to define one line in a coordinate system. The well-known first order equation for a straight line that characterize it algebraically is then described. However, the definition of these parameters in a three-dimensional space, or $\mathbb{R}^3$, cannot be straightforward obtained, since the system is not contained in a plane anymore.

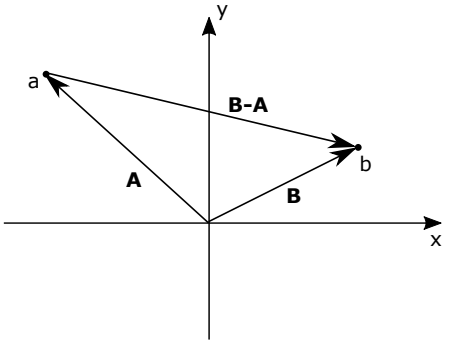

Figure 2.1 – Parameterized line between two points

Initially, two vectors (**A** and **B**) can be used to describe a line between two points. These vectors define where the points are placed in the two-dimensional space, x and y, as shown in Figure 2.1. The subtraction of these entities produce a new vector pointing from a to b. Setting a new parameter S which defines the distance along the line, and considering

a as the initial position, one can obtain:

$$\alpha(S) = \mathbf{a} + S(\mathbf{B} - \mathbf{A}). \tag{2.1}$$

Hence, the straight line $\alpha(S)$ is parameterized as a function of S. In general, a curve in any space can be defined by mapping $\alpha : I \to \mathbb{R}^n$, with I determining the interval of interest and α the differentiable curve in this gap. Then, one can write the function

$$\boldsymbol{r}(S) = [x_1(S) \quad x_2(S) \quad x_3(S)] \tag{2.2}$$

where $x_1(S), x_2(S), x_3(S)$ is a one dimensional triplet in which the differential calculus can be used. Therefore, to parameterize a curve can be defined as to represent its behavior through one or more parameters [Kobayashi e Nomizu, 1963]. Analyzing geometries with this methodology is a procedure that streamline the process, facilitating the derivatives and the reproduction in the $\mathbb{R}^n$, for example.

One can write the derivative of $\boldsymbol{r}(S)$ as $\dfrac{d(\boldsymbol{r}(S))}{dS}$ and the function rate of change is indicated by it. This can also be interpreted as a particle speed traveling through the curve [Pressley, 2010]. Applying the derivative on the components of $\boldsymbol{r}(S)$ results in,

$$\frac{d(\boldsymbol{r}(S))}{dS} = \left[\frac{d(x_1(S))}{dS} \quad \frac{d(x_2(S))}{dS} \quad \frac{d(x_3(S))}{dS}\right]. \tag{2.3}$$

This variation results in an important vector pointed to the tangent direction of the curve, denoted from now on as the tangent vector $\boldsymbol{t}(S)$. This entity is one component of the Frenet-Serret triad, the other two elements are described in the following section.

2.2 Frenet-Serret Triad

To completely describe the curve geometry it is necessary to analyze the parametrization behavior ($\boldsymbol{r}(S)$) near a given point. Hence, not only the parameter S, but also a local system that moves along the curve as the position changes, prospecting its trends and variations.

The vector defined previously, and represented from now on as $\boldsymbol{t}$, is set as the parametrization derivative and represent one axis of this local system. Applying the differentiation again on $(\boldsymbol{r}(S))$, that is, on the tangent vector, the rate of change of the direction is set. Since $\boldsymbol{t}$ is a unitary vector, one can demonstrate that the result is perpendicular to the first entity [Do Carmo, 1976] as:

$$\begin{aligned} \frac{d(\boldsymbol{t}\cdot\boldsymbol{t})}{dS} &= 0 \\ \frac{d(\boldsymbol{t})}{dS}\cdot\boldsymbol{t} + \boldsymbol{t}\cdot\frac{d(\boldsymbol{t})}{dS} &= 0 \\ 2\boldsymbol{t}\cdot\frac{d(\boldsymbol{t})}{dS} &= 0 \\ \boldsymbol{t}\cdot\frac{d(\boldsymbol{t})}{dS} &= 0, \end{aligned} \tag{2.4}$$

therefore, as expected, the vectors $\frac{d(\boldsymbol{t})}{dS}$ and $\boldsymbol{t}$ are orthogonal. This rate has the opposite direction of the radius formed by a circle between two neighbors points. Consequently, a new parameter, called the curvature κ, can be defined. It denotes not only the tangent vector direction change, but also indicates the curvature radius of the curve at S:

$$\kappa(S) = \left|\frac{d(\boldsymbol{t}(S))}{dS}\right|. \tag{2.5}$$

Although the vector derived is unitary, no information is given that implies κ to be unitary as well, since it is calculated as the tangent vector norm. From now on this geometric property is written only as κ.

Hence, one can see that $\boldsymbol{t}$ can change direction rapidly or slowly, depending on the radius. As an example, the two-dimensional system is used, so that for a small circular radius the change rate is high and considering a large arc the variation is low. Therefore, the curvature κ is calculated as the inverse of the arc radius formed by two points sufficiently near. That way, the differentiation of the tangent vector forms a new vector, perpendicular to the original, however not unitary. Using a constant to scale a normalized entity, and setting it as the curvature, a new axis of the local system can be defined. The second derivative of the parameterization represents the normal vector, $\boldsymbol{n}$, pointing to the center of the arc formed for two close points, or in other words, to the change of $\boldsymbol{t}$ and is written as:

$$\mathbf{n}(S) = \frac{d^2(\boldsymbol{r}(S))}{dS^2}\frac{1}{\kappa} = \frac{d(\boldsymbol{t})}{dS}\frac{1}{\kappa}. \tag{2.6}$$

From these definitions, a few important properties can be highlighted. The first shows that for a null curvature, a circle with infinity radius is formed, i.e. a straight line. Therefore, the local system is one dimensional and all information required to define a geometry is known, since:

$$\boldsymbol{r}(S) = dS + e, \tag{2.7}$$

$$\frac{d(\boldsymbol{r}(S))}{dS} = \boldsymbol{t}(S) = d, \tag{2.8}$$

$$\frac{d^2(\boldsymbol{r}(S))}{dS^2} = \frac{d(\boldsymbol{t}(S))}{dS} = \kappa = 0. \tag{2.9}$$

Also, as one can note, for a constant curvature, that is, if κ does not depend on S, the vector change of the tangent direction is always the same, consequently the geometry analyzed forms a circle in a plane, which is defined by $\boldsymbol{t}$ and $\boldsymbol{n}$. This is called osculating and determines the direction and the plane of the change.

One more entity is needed to complete the local system, knowing that the last two vectors are orthogonal and unitary, the cross product can be performed. Hence, the result is also a vector with the same properties. Calling this as the binormal vector ($\boldsymbol{b}$), the procedure:

$$\boldsymbol{b}(S) = \boldsymbol{t}(S) \times \boldsymbol{n}(S), \tag{2.10}$$

determines the final axis. Therefore, the local coordinate system is accomplished and established as $[\boldsymbol{t}, \boldsymbol{n}, \boldsymbol{b}]$ (although, not explicit, all depending on S). Moreover, two more planes are defined: rectifying, between $\boldsymbol{t}$ and $\boldsymbol{b}$, and normal, containing $\boldsymbol{n}$ and $\boldsymbol{b}$. Nevertheless, to completely define the geometry behavior, the variation of the two last vectors must be explored. Starting by the latter, the chain rule needs to be used in the cross product so,

$$\frac{d(\mathbf{b}(S))}{dS} = \frac{d(\boldsymbol{t}(S))}{dS} \times \boldsymbol{n}(S) + \boldsymbol{t}(S) \times \frac{d(\boldsymbol{n}(S))}{dS}, \tag{2.11}$$

with the property from Equation 2.6, where $\frac{d(\boldsymbol{t})}{dS}$ is defined as $\boldsymbol{n}$, the cross results in zero, hence, the first term on the right hand side is defined.

Since the normal vector variation is not defined yet two possibilities can be considered: a result aligned to $\boldsymbol{t}$ or $\boldsymbol{b}$. The first option implies $\boldsymbol{t} \times \boldsymbol{t}$ which is zero. So, $\frac{d(\boldsymbol{n})}{dS}$ is already defined as aligned to $\boldsymbol{b}$ [Kreyszig, 1968] and the cross product with the tangent vector results in a scalar combination with the normal vector (since it does not need to be unitary) written as:

$$\frac{d(\boldsymbol{b})}{dS} = -\tau \boldsymbol{n}(S), \tag{2.12}$$

where τ is defined as the torsion on the position S. This parameter indicates the tangent vector trend to deviate from the osculating plane (the variation stays in the rectifying plane), just as κ defines the variation from the rectifying. So, the geometry and the tendencies of any curve, being smooth during the interest interval, can be studied by the application of the derived equations.

Equation (2.12) shows that if the torsion is zero, $\frac{d(\boldsymbol{b})}{dS}$ is also null and, consequently, the system remains in the osculating plane, which means that the curve is contained in $\mathbb{R}^2$.

One may conclude that the curvature indicates the tendency of the curve not to be a line, i.e., the lowest the value the straighter is the geometry, while the torsion demonstrate the propensity to be contained in a plane, or, to have two or even one dimension.

The last entity to be defined is the variation of the normal vector that, according to what was presented before, is orthogonal to $\boldsymbol{n}$ and written as

$$\frac{d(\boldsymbol{n})}{dS} = \frac{d(\boldsymbol{t})}{dS} \times \boldsymbol{b}(S) + \boldsymbol{t}(S) \times \frac{d(\boldsymbol{b})}{dS}, \tag{2.13}$$

Once again, using the properties defined in Equations (2.6) and (2.12) and knowing the characteristic of the cross product $\boldsymbol{n}(S) \times \boldsymbol{b}(S) = -\boldsymbol{t}(S)$ and $\boldsymbol{n}(S) \times \boldsymbol{t}(S) = -\boldsymbol{b}(S)$, the

last variation of the canonical vectors is

$$\frac{d(\boldsymbol{n})}{dS} = -\kappa \boldsymbol{t}(S) + \tau \boldsymbol{b}(S). \tag{2.14}$$

Finally, the local system is determined and is called the Frenet-Serret triad (FS). In a matrix form, FS can be written as

$$\begin{bmatrix} \dfrac{d(\boldsymbol{t})}{dS} \\ \dfrac{d(\boldsymbol{n})}{dS} \\ \dfrac{d(\boldsymbol{b})}{dS} \end{bmatrix} = \begin{bmatrix} 0 & \kappa & 0 \\ -\kappa & 0 & \tau \\ 0 & -\tau & 0 \end{bmatrix} \begin{bmatrix} \boldsymbol{t} \\ \boldsymbol{n} \\ \boldsymbol{b} \end{bmatrix}. \tag{2.15}$$

These equations describe the properties of a differential curve along the local coordinate S, as shows Figure 2.2. The variations of the canonical vectors are always orthogonal to the original and can be represented as a linear combination of the respective entity that has the same orientation.

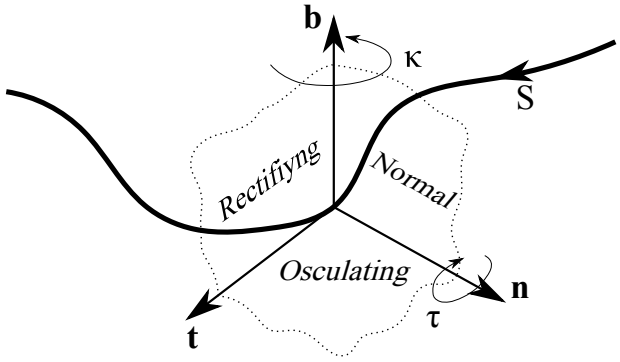

Figure 2.2 – Generic curve containing the local system indicated and the respective planes together with the curvature and torsion.

This theory was used in the example developed next, where the differential geometry is employed to parameterize a helix. This configuration can be used to model different types of structure as springs, strands, etc.

2.3 Cable Geometry

A basic geometry of a cable is presented in Figure 2.3 . It consists in a central straight core and one layer of helical wires as indicated. The central line of one wire is highlighted together with the FS triad (also the geometric parameters κ and τ) and the local coordinate S.

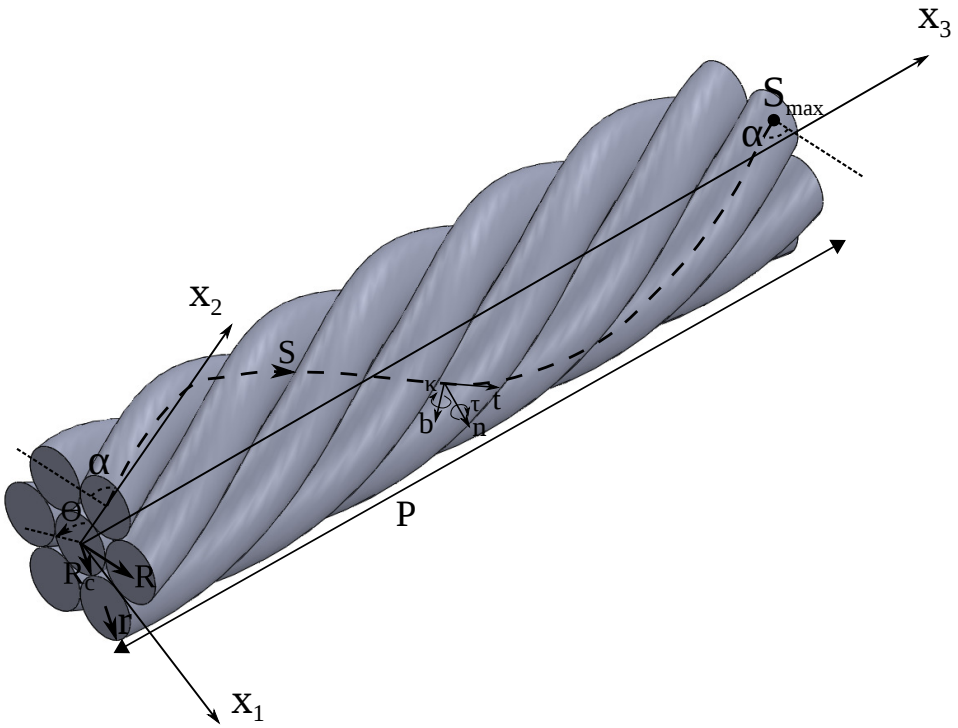

Figure 2.3 – Basic cable structure and the geometric features.

The global system is also indicated by x_1, x_2 and x_3 passing through the center core. α represents the helix angle, formed between the x_1x_2 plane and the central line. Note that this angle is the same at the beginning and the final coordinate (S_{max}) at the end of, in this case, one pitch (P). The angle in the x_1x_2 plane is also indicated as θ. Also, r denotes the wire and R_c the core radius. The central line of the wire has a starting point in the radius indicated by R.

Some simplifications on the geometry, boundary conditions, material and others were made to simplify the study. Therefore, the central line of the wire can be used to study its behavior. An helix parameterization was defined in the next section to allow the structure mechanical response.

2.4 Helix Parametrization

An helix can be parametrized as:

$$x_1 = R\cos\left(\frac{S\cos(\alpha)}{R}\right), \tag{2.16}$$

$$x_2 = R\sin\left(\frac{S\cos(\alpha)}{R}\right), \tag{2.17}$$

$$x_3 = S\sin(\alpha), \tag{2.18}$$

where R corresponds to the radius, S is the position along the curve and α denotes the helix angle, i.e., the angle formed by the helix and the x_1x_2 plane as shown in Figure 2.4, where only one revolution, is represented. Since α is constant, in this particular case, the tangent vector inclination is also unchanged and the angle is also equal to α.

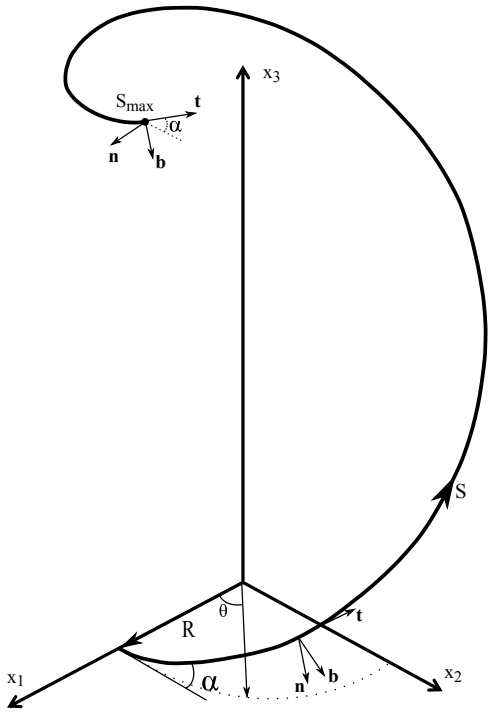

Figure 2.4 – Helix parameterization represented with the Frenet-Serret triad

This parametrization describes an helix with a left hand turn, or counter clockwise. To generate a rotation with a contrary orientation, it is necessary to multiply Equation (2.17)

by -1 (this configuration will not be analyzed here). Thus, writing the geometry in this fashion, it allows understanding not only a point in the coordinate (S), but also to measure the angle formed by this position and starting point in the x_1x_2 plane. Represented by θ, in Figure 2.5, it is calculated as,

$$\theta = \frac{S\cos(\alpha)}{R}, \tag{2.19}$$

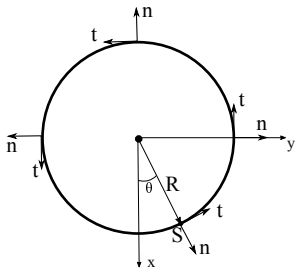

Figure 2.5 – Parameterized helix represented in the osculator plane.

denoted by the Frenet-Serret triad obtained previously, the local system, is also indicated in Figure 2.5. The tangent vector was calculated using the parametrization and the methodology aforementioned.

The geometric parameter κ was determined by the norm of $\boldsymbol{t}$. Using this result and dividing by the derivative of the tangent vector $\boldsymbol{n}$ was obtained.

The binormal vector was generated by the cross product between the other two entities. Therefore, a transformation matrix was formed by these components that allows the transition from the local system to the global. This matrix was written as

$$\mathbf{T} = \begin{bmatrix} -\sin\left(\dfrac{S\,\cos(\alpha)}{R}\right)\cos(\alpha) & \cos\left(\dfrac{S\cos(\alpha)}{R}\right)\cos(\alpha) & \sin(\alpha) \\ \cos\left(\dfrac{S\,\cos(\alpha)}{R}\right) & \sin\left(\dfrac{S\,\cos(\alpha)}{R}\right) & 0 \\ -\sin\left(\dfrac{S\,\cos(\alpha)}{R}\right)\sin(\alpha) & \cos\left(\dfrac{S\,\cos(\alpha)}{R}\right)\sin(\alpha) & -\cos(\alpha) \end{bmatrix}. \tag{2.20}$$

The helix representation is defined by a local system which is not aligned to the

global coordinates. Results obtained in either systems can be used, or analyzed, in a different canonical entity. Therefore, since $\mathbf{T}$ is formed by the local quantities, the multiplication of it by any effect performs the transformation from local to global as:

$$\mathbf{R}^{Global} = \mathbf{T}\mathbf{R}^{Local}, \tag{2.21}$$

hence, the opposite transformation, from the global to local system, $\mathbf{R}^{Global}$ is divided by $\mathbf{T}$

Equations (2.5) and (2.12) were used to obtain κ and τ, respectively. Since the parameterization is n-times differentiable in the chosen interval, the parameters could be determined. Calculating the norm of the vectors $\boldsymbol{t}'$ and $\boldsymbol{b}'$, it is possible to write

$$\kappa = \frac{-cos^2(\alpha)}{R}, \tag{2.22}$$

$$\tau = \frac{sen(\alpha)cos(\alpha)}{R}. \tag{2.23}$$

One important property of these parameters is that, since α and R are geometrical properties and constants, that they are constants throughout the domain as well. Therefore, one pitch, or one revolution, is sufficient to represent the cable complete behavior, due to the parameters repetition. Also, using this parameterization, it implies that it is possible to have curvature without torsion, however the opposite is never true.

The negative sign of the curvature was used to position the global system in the center of the helix. This changes the direction of the local system producing an inside-out normal vector and a downwards $\boldsymbol{b}$. The results are not influenced by this choice, only the sign exchange of the second and third components.

One turn of the helix sets the maximum distance from the beginning to ending point as a function of S. Knowing the parameter θ calculated in Equation (2.19) (defining the angle in the osculating plane) the maximum position is determined when $\theta = 2\pi$, so

$$S_{max} = \frac{2\pi R}{\cos(\alpha)}. \tag{2.24}$$

A particular case of this parametrization is the so-called plane arc. Considering $\alpha = 0$ the equation 2.18 is null. As the variation of the curve in this direction occurs due to this parameter, the geometry becomes contained in a plane. The other two terms are responsible for a circular movement, i.e., an arc in the osculating plane. Thus, if one determine the terms κ and τ, it results in a constant value, equal to $\frac{1}{R}$, and, as explained before, in a null value, respectively. This situation is represented in the Figure 2.6.

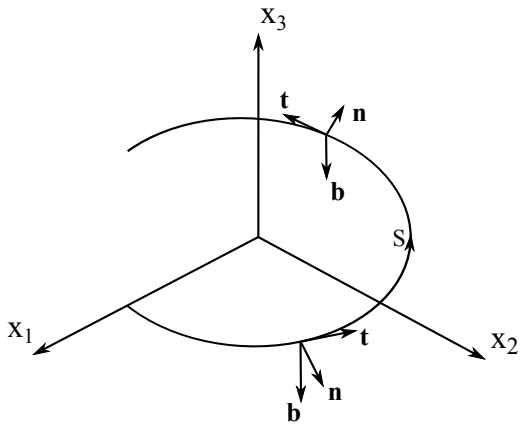

Figure 2.6 – Arc parameterized representation.

3. SPATIAL BEAM THEORY

The mechanical response of a long thin rod can be obtained from the spatial beam theory [Love, 2013]. The equilibrium equations for such theory were obtained considering an infinitesimal portion of the beam.

A curved beam, in a global basis (three dimensional), was modeled according to its center line. Parameterizing the geometry introduced a local coordinate system, the Frenet-Serret triad, and a coordinate S defining the position along the curve [Luongo e Zulli, 2013].

In this chapter, the equilibrium equations were obtained for forces and moments by the analysis of a differential element. The Principle of Virtual Work was also used, with the kinetic assumptions, to determine the expressions for displacements and rotation.

3.1 Equilibrium Equations

The equilibrium equations of the spatial beam theory were obtained considering a generic beam represented spatially by its central line (Figure 3.1) where the Frenet-Serret triad is represented in the central line with the curvilinear coordinate S along the curve. The geometry is subjected to the generic loadings N and M, representing concentrated forces and moments, together with q and m, denoting distributed forces and moments.

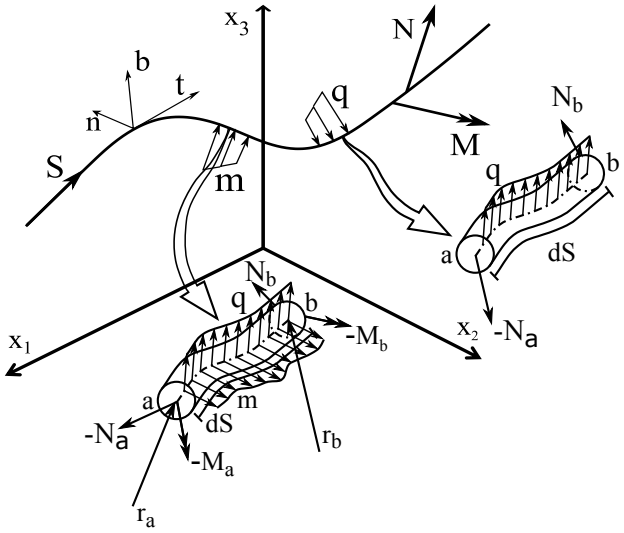

Figure 3.1 – Generic curve and loads applied in the beam central line representation.

A differential element of the curve, dS, represented in Figure 3.1 was verified by the

sum of forces ($\Sigma\mathbf{F} = 0$) and moments ($\Sigma\mathbf{M} = 0$).

The distributed load is integrated from a starting point, a, to the end point, b, and added to the internal forces $\mathbf{N}_a$ and $\mathbf{N}_b$ so that the equilibrium is written as:

$$\Sigma\mathbf{F} = \mathbf{N}_b - \mathbf{N}_a + \int_a^b \mathbf{q}(S)\ dS \tag{3.1}$$

Since it is considered an infinitesimal element, the difference between the components of force is represented as a derivative. The equilibrium is then expressed as

$$\int_a^b \left[\frac{d\mathbf{N}(S)}{dS} + \mathbf{q}(S)\right] dS = 0, \tag{3.2}$$

or

$$\frac{d\mathbf{N}(S)}{dS} + \mathbf{q}(S) = 0. \tag{3.3}$$

Assuming, in a local basis, that the loads produce effects in different directions, the transformation matrix is used to decompose these components, so that $\mathbf{N}$ and $\mathbf{q}$ are expressed as

$$\mathbf{N}(S) = N_1\mathbf{t} + N_2\mathbf{n} + N_3\mathbf{b}, \tag{3.4}$$

$$\mathbf{q}(S) = q_1\mathbf{t} + q_2\mathbf{n} + q_3\mathbf{b}, \tag{3.5}$$

where N_1 represents the normal force while N_2 and N_3 the shear forces, in $\boldsymbol{n}$ and $\boldsymbol{b}$, respectively,

$$\frac{d}{dS}\left(N_1\mathbf{t} + N_2\mathbf{n} + N_3\mathbf{b}\right) + q_1\mathbf{t} + q_2\mathbf{n} + q_3\mathbf{b} = 0. \tag{3.6}$$

expanding Equation (3.6) results in

$$\frac{dN_1}{dS}\mathbf{t} + \frac{d\mathbf{t}}{dS}N_1 + \frac{dN_2}{dS}\mathbf{n} + \frac{d\mathbf{n}}{dS}N_2 + \frac{dN_3}{dS}\mathbf{b} + \frac{d\mathbf{b}}{dS}N_3 + q_1\mathbf{t} + q_2\mathbf{n} + q_3\mathbf{b} = 0, \tag{3.7}$$

and with the components of the triad (properties obtained in Equations (2.5), (2.13) and (2.14)), one can write

$$\left(\frac{dN_1}{dS} - \kappa N_2 + q_1\right)\mathbf{t} + \left(\frac{dN_2}{dS} + \kappa N_1 - \tau N_3 + q_2\right)\mathbf{n} + \left(\frac{dN_3}{dS} + \tau N_2 + q_3\right)\mathbf{b} = 0, \tag{3.8}$$

therefore, the local system of equilibrium equations, obtained in the local system, for each direction of the triad can be written as

$$\begin{aligned} &\frac{dN_1}{dS} - \kappa N_2 + q_1 = 0, \\ &\frac{dN_2}{dS} + \kappa N_1 - \tau N_3 + q_2 = 0, \\ &\frac{dN_3}{dS} + \tau N_2 + q_3 = 0. \end{aligned} \tag{3.9}$$

The equilibrium equations for the moments are obtained using the same approach. The sum of the moments is performed, noticing that the forces also produce moments with the brace $\mathbf{r}$. One can write,

$$\Sigma\mathbf{M} = \int_a^b \mathbf{m} + \mathbf{r} \times \mathbf{q} dS - \mathbf{M}_a + \mathbf{M}_b - \mathbf{r}_a \times N_a + \mathbf{r}_b \times N_b. \tag{3.10}$$

The integral form is expressed as,

$$\int_a^b \left[\mathbf{m} + \mathbf{r} \times \mathbf{q} + \frac{d\mathbf{M}}{dS} + \frac{d}{dS}\left(\mathbf{r} \times \mathbf{N}\right)\right] dS = 0. \tag{3.11}$$

The product rule and the derivative were applied and the expression is now written as,

$$\mathbf{m} + \mathbf{r} \times \mathbf{q} + \frac{d\mathbf{M}}{dS} + \frac{d\mathbf{r}}{dS} \times \mathbf{N} + \frac{d\mathbf{N}}{dS} \times \mathbf{r} = 0, \tag{3.12}$$

applying the property of Equation (2.3), where the derivative of the position vector is equal to the tangent vector $\mathbf{t}$, and manipulating the expression one can write

$$\mathbf{m} + \frac{d\mathbf{M}}{dS} + \mathbf{t} \times \mathbf{N} + \mathbf{r} \times \left(\frac{d\mathbf{N}}{dS} + \mathbf{q} \right) = 0, \tag{3.13}$$

where the component inside the parenthesis is the same as found in the the equilibrium of forces, Equation 3.3, so it is equal to zero. Using the same methodology for the moments, where the local effects are expressed as

$$\mathbf{M} = M_1\mathbf{t} + M_2\mathbf{n} + M_3\mathbf{b}, \tag{3.14}$$

therefore, in terms of components, the equilibrium for moments is written as, after the derivatives,

$$\begin{aligned} &\frac{dM_1}{dS}\mathbf{t} + \frac{d\mathbf{t}}{dS}M_1 + \frac{dM_2}{dS}\mathbf{n} + \frac{d\mathbf{n}}{dS}M_2 + \frac{dM_3}{dS}\mathbf{b} + \frac{d\mathbf{b}}{dS}M_3 + \mathbf{t} \times (N_1\mathbf{t} + N_2\mathbf{n} + N_3\mathbf{b}) + \\ &+ m_1\mathbf{t} + m_2\mathbf{n} + m_3\mathbf{b} = 0. \end{aligned} \tag{3.15}$$

Once again, using the properties of the parametrization in Equations 2.5, 2.13 and 2.14 the expression is now written as,

$$\begin{aligned} &\left(\frac{dM_1}{dS} - \tau M_2 + m_1 \right) \mathbf{t} + \left(\frac{dM_2}{dS} - \kappa M_1 - \tau M_3 - N_3 + m_2 \right) \mathbf{n} + \\ &+ \left(\frac{dM_3}{dS} + \tau M_2 + N_2 + m_3 \right) \mathbf{b} = 0. \end{aligned} \tag{3.16}$$

Therefore, the system of equilibrium equation for moments is given by,

$$\begin{aligned} &\frac{dM_1}{dS} - \kappa M_2 + m_1 = 0, \\ &\frac{dM_2}{dS} + \kappa M_1 - \tau M_3 - N_3 + m_2 = 0, \\ &\frac{dM_3}{dS} + \tau M_2 + N_2 + m_3 = 0. \end{aligned} \tag{3.17}$$

With forces and moments expressions in the local system, geometry parameters were used to determine stresses and the constitutive model can be applied to obtain strains of the structure.

The geometric parameters are defined: A wire cross section area; I moment of inertia; J polar moment of inertia and y rod radius. Therefore, considering an isotropic material, the strains were determined so that six components are written as

$$\varepsilon_1 = \frac{N_1}{EA}, \tag{3.18}$$

$$\varepsilon_2 = \frac{-M_2 y}{EI}, \tag{3.19}$$

$$\varepsilon_3 = \frac{-M_3 y}{EI}, \tag{3.20}$$

$$\rho_1 = \frac{M_1 y}{GJ}, \tag{3.21}$$

$$\rho_2 = \frac{N_2}{GA}, \tag{3.22}$$

$$\rho_3 = \frac{N_3}{GA}, \tag{3.23}$$

where E is the material's elastic modulus and G its shear modulus.

3.2 Kinematics Relations

With the variables described above (forces, moments, strains and stresses), together with the geometric parameters that define the structure, the displacements can also be determined. To obtain these components it is necessary to apply some kinematics assumptions.

Using an admissible field for displacements that can be written as,

$$\boldsymbol{u} = \begin{bmatrix} u_1 & u_2 & u_3 \end{bmatrix}^T \tag{3.24}$$

and for the rotations

$$\boldsymbol{\phi} = \begin{bmatrix} \phi_1 & \phi_2 & \phi_3 \end{bmatrix}^T \tag{3.25}$$

Considering these vectors representing each direction in a global system, the Frenet-Serret triad must be used to analyze the effects in the local system. Therefore, multiplying Equation (2.15) and the local displacements one can express,

$$\mathbf{u} = u_1\mathbf{t} + u_2\mathbf{n} + u_3\mathbf{b}, \tag{3.26}$$

analogously,

$$\boldsymbol{\phi} = \phi_1\mathbf{t} + \phi_2\mathbf{n} + \phi_3\mathbf{b}. \tag{3.27}$$

In order to derive such variables the Principle of Virtual Work (PVW) is applied. The general form of the PVW, considering infinitesimal displacements,

$$\int_V \boldsymbol{\sigma}\delta\boldsymbol{\varepsilon}\ dV = \int_V \boldsymbol{b}\delta\boldsymbol{u}\ dV + \int_S \boldsymbol{t}\delta\boldsymbol{u}\ dS. \tag{3.28}$$

That way, the axial and transverse (ε) and the torsional and bending (ρ) strains, expressing the local effects by the application of the same methodology as for the displacements, must be used.

$$\boldsymbol{\varepsilon} = \varepsilon_1\mathbf{t} + \varepsilon_2\mathbf{n} + \varepsilon_3\mathbf{b}, \tag{3.29}$$

$$\boldsymbol{\rho} = \rho_1\mathbf{t} + \rho_2\mathbf{n} + \rho_3\mathbf{b}. \tag{3.30}$$

Considering that no body force is acting and the one dimensional problem (S), the PVW can be expressed as

$$\int_a^b [\mathbf{N}\delta\boldsymbol{\varepsilon} + \mathbf{M}\delta\boldsymbol{\rho}\,]\,dS = \int_a^b [\mathbf{q}\delta\mathbf{u} + \mathbf{m}\delta\boldsymbol{\phi}]\;\, dS + \mathbf{N}\delta\mathbf{u}\big|_a^b + \mathbf{M}\delta\boldsymbol{\phi}\big|_a^b, \tag{3.31}$$

so, using the results obtained above the right-hand side can be rewritten as

$$\int_a^b \left[\mathbf{q}\delta\mathbf{u} + \mathbf{m}\delta\boldsymbol{\phi} + \frac{d}{dS}\left(\mathbf{N}\delta\mathbf{u}\right) + \frac{d}{dS}\left(\mathbf{M}\delta\boldsymbol{\phi}\right)\right] dS, \tag{3.32}$$

which, after the derivatives and rearranging the terms become,

$$\int_a^b \left[\left(\mathbf{q} + \frac{d\mathbf{N}}{dS}\right)\delta\mathbf{u} + \left(\mathbf{m} + \frac{d\mathbf{M}}{dS}\right)\delta\boldsymbol{\phi} + \frac{d\delta\mathbf{u}}{dS}\mathbf{N} + \mathbf{M}\frac{d\delta\boldsymbol{\phi}}{dS}\right] dS, \tag{3.33}$$

so, using the equilibrium Equation (3.3) the expression in the first parenthesis is zero and manipulating Equation (3.13) the second is equal to $(-\mathbf{t}\times\mathbf{N})$,

$$\int_a^b \left[\left(\mathbf{t}\times\mathbf{N}\right)\delta\boldsymbol{\phi} + \frac{d\delta\mathbf{u}}{dS}\mathbf{N} + \mathbf{M}\frac{d\delta\boldsymbol{\phi}}{dS}\right] dS. \tag{3.34}$$

Therefore, since $(\mathbf{N}\times\mathbf{t})\delta\phi = (\delta\phi\times\mathbf{t})\mathbf{N}$, the Equation (3.31) is written as,

$$\int_a^b [\mathbf{N}\delta\boldsymbol{\varepsilon} + \mathbf{M}\delta\boldsymbol{\rho}\,]\,dS = \int_a^b \left[\mathbf{N}\left(\delta\boldsymbol{\phi}\times\mathbf{t} + \frac{d\delta\mathbf{u}}{dS}\right) + \mathbf{M}\frac{d\delta\boldsymbol{\phi}}{dS}\right] dS, \tag{3.35}$$

and, as long as both sides are equal, consequently the strains are now related to the displacements

$$\delta\boldsymbol{\varepsilon} = \delta\boldsymbol{\phi}\times\mathbf{t} + \frac{d\delta\mathbf{u}}{dS}, \tag{3.36}$$

$$\delta\boldsymbol{\rho} = \frac{d\delta\boldsymbol{\phi}}{dS}. \tag{3.37}$$

The results show that the strains are dependent not only on the displacements but also on the rotations, while the angle is regulated exclusively by the rotations.

Expressing these relations in terms of components, using the same methodology applied to the determination of the equilibrium equations, it is possible to write,

$$\delta\varepsilon_1\mathbf{t} + \delta\varepsilon_2\mathbf{n} + \delta\varepsilon_3\mathbf{b} = \frac{d}{dS}\left(\delta u_1\mathbf{t} + \delta u_2\mathbf{n} + \delta u_3\mathbf{b}\right) + \left(\delta\phi_1\mathbf{t} + \delta\phi_2\mathbf{n} + \delta\phi_3\mathbf{b}\right) \times \mathbf{t}, \tag{3.38}$$

knowing that the vectors of the triad are mutually orthogonal to each other (i.e, $\boldsymbol{t} \times \boldsymbol{t} = 0$, $\boldsymbol{t} \times \boldsymbol{n} = \boldsymbol{b}$ and $\boldsymbol{t} \times \boldsymbol{b} = -\boldsymbol{n}$), after the derivatives and the parameterization properties the products are represented as

$$\begin{aligned}\delta\varepsilon_1\mathbf{t} + \delta\varepsilon_2\mathbf{n} + \delta\varepsilon_3\mathbf{b} = &\left(\frac{d}{dS}\delta u_1 - \kappa\delta u_2\right)\mathbf{t} + \left(\kappa\delta u_1 + \frac{d}{dS}\delta u_2 - \tau\delta u_3 + \delta\phi_3\right)\mathbf{n} + \\ &+ \left(\tau\delta u_2 + \frac{d}{dS}\delta u_3 + \delta\phi_2\right)\mathbf{b},\end{aligned} \tag{3.39}$$

consequently, the system of equations can be described as

$$\begin{aligned}\varepsilon_1 &= \frac{du_1}{dS} - \kappa u_2, \\ \varepsilon_2 &= \frac{du_2}{dS} + \kappa u_1 - \tau u_3 + \phi_3, \\ \varepsilon_3 &= \frac{du_3}{dS} + \tau u_2 + \phi_2.\end{aligned} \tag{3.40}$$

Analogously, the rotations are defined in terms of the components as

$$\delta\rho_1\mathbf{t} + \delta\rho_2\mathbf{n} + \delta\rho_3\mathbf{b} = \frac{d}{dS}\left(\delta\phi_1\mathbf{t} + \delta\phi_2\mathbf{n} + \delta\phi_3\mathbf{b}\right), \tag{3.41}$$

hence, with the derivatives and properties applied the system is formed

$$\begin{aligned}\rho_1 &= \frac{d\phi_1}{dS} - \kappa\phi_2, \\ \rho_2 &= \frac{d\phi_2}{dS} + \kappa\phi_1 - \tau\phi_3, \\ \rho_3 &= \frac{d\phi_3}{dS} + \tau\phi_2.\end{aligned} \tag{3.42}$$

With these expressions, one can analyze mechanically a structure as a beam, either straight or in a spring shape. The solution of the systems of equations provides the required information to determine its behavior independently of the shape.

The boundary conditions (BC), the material model (or constitutive relations) and the geometry must also be set to provide numerical results. Solving the first two systems (Equations 3.9 and 3.17) produce six constants due to the integration that are determined by the BC (reactions).

These steps were used, in the following sections, to built a mathematical model in order to simulate an helical structure.

4. PROPOSAL OF AN ANALYTIC MODEL

The equilibrium equations determined previously were used to model one of the strands of the cable. Considering a cable formed by a straight core surrounded by n helices, with one layer, the mechanical behavior of one strand can be obtained simplifying its geometry regarding the center line through a parametrization [Lee, 1991].

Equations (2.16), (2.17) and (2.18) define the helix geometry and the hypothesis of no contact between strand-core and strand-strand and friction [Labrosse et al., 2000] and no slipping were considered. The results could be used in the remaining structures adding an angle to the starting point $\varphi = \theta + (\frac{2\pi}{n_{dc}})$, where n_{dc} is the number of strands in the structure [Usabiaga e Pagalday, 2008].

Based on this geometric definition, the properties κ and τ were defined as Equations (2.22) and (2.23), respectively. Together with the Frenet-Serret triad and the transformation matrix ($\mathbf{T}$), that allows the transference from a global system to a local system and vice-verse and to apply the boundary conditions.

The equilibrium equations for forces, moments, rotations and displacements (Equations 3.17, 3.9, 3.42 and 3.40, respectively) were solved for two different geometries. With the geometric parameter α indicating the helix angle, it is possible to represent a plane arc, an helix and a straight beam ($\alpha = 0°$, $0° < \alpha < 90°$ and $\alpha = 90°$, respectively). These sets are explored in this chapter.

4.1 Plane Arc

As demonstrated previously, if the helix angle is set as zero, the geometry is contained in a plane. The torsion (τ) becomes null and, consequently, the equilibrium equations of forces are reduced to

$$\frac{dN_1(S)}{dS} - \kappa N_2(S) + q_1 = 0, \tag{4.1}$$

$$\frac{dN_2(S)}{dS} + \kappa N_1(S) + q_2 = 0, \tag{4.2}$$

$$\frac{dN_3\left(S\right)}{dS} + q_3 = 0. \tag{4.3}$$

One can conclude that, in this case, the first two equations are coupled due to the FS, where the decomposition of loads produces effects in both directions. Therefore, the above differential equation system was solved.

Initially, isolating N_2 in Equation (4.1) and substituting in to the Equation (4.2), a second order differential equation emerges $\left(\frac{d^2N_1}{dS^2}\right)$. Solving the homogeneous differential part first, it is produced as a result a complex conjugate pair, thus, a combination of sines and cosines. The non-homogeneous part generates the terms that does not depend on S,

$$N_1\left(S\right) = C_1 \cos\left(\kappa\, S\right) + C_2 \,\text{sen}\, \left(\kappa\, S\right) - \frac{q_2}{\kappa}. \tag{4.4}$$

The resulting equation is derived and the term N_2 was defined as,

$$N_2\left(S\right) = -C_1 \,\text{sen}\, \left(\kappa\, S\right) + C_2 \cos\left(\kappa\, S\right) - \frac{q_1}{\kappa}, \tag{4.5}$$

the solution of the third equation was performed by the integration of the terms, since it is linearly independent of Equations (4.1) and (4.2).Therefore, it is written as,

$$N_3\left(S\right) = -q_3 S + C_3. \tag{4.6}$$

The equilibrium equations that describe the moments are dependent on the forces. Thus, using the expressions obtained in Equations 4.5 and 4.6, the reduced system, due to the null torsion, one can write

$$\frac{dM_1\left(S\right)}{dS} - \kappa\, M_2\left(S\right) + m_1 = 0, \tag{4.7}$$

$$\frac{dM_2\left(S\right)}{dS} + \kappa\, M_1\left(S\right) - \left(-q_3 S + C_3\right) + m_2 = 0, \tag{4.8}$$

$$\frac{dM_3\,(S)}{dS} + \left(-C_1\,\text{sen}\;(\kappa\,S) + C_2\cos(\kappa\,S) - \frac{q_1}{\kappa}\right) + m_3 = 0. \tag{4.9}$$

In order to determine the moments equations, the same methodology is applied, i.e., isolating M_2 in the first equation, replacing it in the second and, once again, solving the homogeneous characteristic equation, M_1 was determined. Consequently, using the derivative, M_2 was set. The term M_3 was obtained by the integration. Hence, it is possible to write

$$M_1\,(S) = C_4\cos(\kappa\,S) + C_5\,\text{sen}\;(\kappa\,S) + \frac{C_1 - m_2 - q_3 S}{\kappa}, \tag{4.10}$$

$$M_2\,(S) = -C_4\,\text{sen}\;(\kappa\,S) + C_5\cos(\kappa\,S) + \frac{m_1\kappa - q_3}{\kappa^2}, \tag{4.11}$$

$$M_3\,(S) = \frac{-C_1\cos(\kappa\,S) - C_2\,\text{sen}\;(\kappa\,S) - q_1 S - m_3\kappa\,S + C_6\,\kappa}{\kappa}. \tag{4.12}$$

From the expression obtained previously, the stresses and strains, on the strand, were determined using the spatial beam theory and the Hooke's law, generating a result considering a linear material. This hypothesis is coherent with the steel cable proposed.

Different materials are currently used to produce this kind of structure. With the reinforced fiber in the direction of interest, composite materials are an alternative vastly applied. Works using this theory are found in the literature in Pan, 1992 (parts I, II, III and IV), Ghoreishi et al., 2007a (parts I and II) and Pidaparti et al., 2001 for example.

The proposed methodology was used and, considering the strand radius (r) as the worst case for the strains, Equations (3.18), (3.19), (3.20), (3.21), (3.22) and (3.23) are rewritten as,

$$\varepsilon_1 = \frac{C_1\cos(\kappa\,S) + C_2\,\text{sen}\;(\kappa\,S) - \dfrac{q_2}{\kappa}}{EA}, \tag{4.13}$$

$$\varepsilon_2 = \frac{-C_1\,\text{sen}\;(\kappa\,S) + C_2\cos(\kappa\,S) - \dfrac{q_1}{\kappa}}{A\,G}, \tag{4.14}$$

$$\varepsilon_3 = \frac{-q_3 S + C_3}{A\,G}, \tag{4.15}$$

analogously, the equations for deflection, in the local system, are defined as

$$\rho_1 = \frac{C_3 \cos(\kappa\, S) + C_4 \,\text{sen}\,(\kappa\, S) + \dfrac{C_1 - m_2 - q_3 S}{\kappa}}{GJ}, \tag{4.16}$$

$$\rho_2 = \frac{(C_1 \cos(\kappa\, S) + C_2 \,\text{sen}\,(\kappa\, S) + q_1 S + m_3 \kappa\, S - C_5\, \kappa)\, r}{\kappa\, EI}, \tag{4.17}$$

$$\rho_3 = \frac{\left(C_3 \,\text{sen}\,(\kappa\, S) - C_4 \cos(\kappa\, S) + \dfrac{q_3 - m_1 \kappa}{\kappa^2}\right) r}{EI} \tag{4.18}$$

In this case, the local areas were calculated as circles, since the variables N_i and M_i were determined in a local basis and the tangent vector is orthogonal to the section.

Therefore, the system in Equation 3.42 can be rewritten, for this case, replacing the values found for strains as

$$\begin{aligned}
&\frac{d\phi_1(S)}{dS} - \kappa\,\phi_2(S) + \frac{-C_3\,\kappa\cos(\kappa\, S) - C_4\,\kappa\,\text{sen}\,(\kappa\, S) - C_1 + m_2 + q_3 S}{\kappa\, GJ} = 0 \\
&\frac{d\phi_2(S)}{dS} + \kappa\,\phi_1(S) + \frac{(-C_1\cos(\kappa\, S) - C_2\,\text{sen}\,(\kappa\, S) - q_1 S - m_3\kappa\, S + C_5\,\kappa)\, r}{\kappa EI} = 0 \\
&\frac{d\phi_3(S)}{dS} + \frac{(-C_3\kappa^2\,\text{sen}\,(\kappa\, S) + C_4\kappa^2\cos(\kappa\, S) - q_3 + m_1\kappa)\, r}{\kappa^2 EI} = 0.
\end{aligned} \tag{4.19}$$

Displacements were calculated after the rotations due to the coupling. Consequently, there is an influence of forces and moments into this variable, so that:

$$
\begin{aligned}
&\frac{du_1\left(S\right)}{dS} - \kappa u_2\left(S\right) + \frac{\left(-C_1\cos\left(\kappa\, S\right) - C_2\,\text{sen}\,\left(\kappa\, S\right) + \dfrac{q_2}{\kappa}\right)}{EA} = 0,\\
&\frac{du_2(S)}{dS} + \kappa u_1\left(S\right) + \int_0^S \frac{\left(C_4\,\kappa^2\cos\left(\kappa\, S\right) + C_5\kappa^2\,\text{sen}\,\left(\kappa S\right) + \kappa m_1 - q_3\right) r}{\kappa^2 EI} dS +\\
&\qquad + \frac{C_1\kappa\,\text{sen}\,\left(\kappa\, S\right) - C_2\kappa\cos\left(\kappa\, S\right) - q_1}{\kappa AG} = 0,\\
&\frac{du_3(S)}{dS} + \int_0^S \kappa\,\phi_1\left(S\right) - \frac{\left(C_1\cos\left(\kappa\, S\right) + C_2\,\text{sen}\,\left(\kappa\, S\right) + \left(q_1 - m_3\kappa\right)S - C_5\,\kappa\right) r}{\kappa\, EI} dS +\\
&\qquad + \frac{q_3 S - C_3}{AG} = 0,
\end{aligned}
\tag{4.20}
$$

The expression to determine u_3 has the rotation ϕ_2 coupled, which also depends on the other components, ϕ_1 and ϕ_3, Consequently, one can not isolate the terms of Equation (4.20) (b), and solving the full system is necessary to describe the displacement as a function of S only.

4.2 Helix Model

As mentioned before, the helix angle defines the parameters κ and τ, i.e., considering the case in which both are different than zero one gets $0^\circ < \alpha < 90^\circ$. This means that the geometry generated by Equations 2.16, 2.17 and 2.18 is an helix.

The equilibrium equations, for this case, are complete. In other words, there is no null term and the equations are coupled:

$$\frac{d\boldsymbol{\eta}}{dS} - \mathbf{T}_{FS}\boldsymbol{\eta} + \mathbf{q} = \mathbf{0}, \tag{4.21}$$

$$\frac{d\boldsymbol{\mu}}{dS} - \mathbf{T}_{FS}\boldsymbol{\mu} - \boldsymbol{\Psi}_{23}\boldsymbol{\eta} + \mathbf{m} = \mathbf{0}. \tag{4.22}$$

where $\mathbf{T}_{FS}$ is the Frenet-Serret geometry properties matrix,

$$\mathbf{T}_{FS} = \begin{bmatrix} 0 & \kappa & 0 \\ -\kappa & 0 & \tau \\ 0 & -\tau & 0 \end{bmatrix}, \ \mathbf{\Psi}_{23} = \begin{bmatrix} 0 & 0 & 0 \\ 0 & 0 & 1 \\ 0 & -1 & 0 \end{bmatrix}, \tag{4.23}$$

$$\boldsymbol{\eta} = \begin{bmatrix} N_1 \\ N_2 \\ N_3 \end{bmatrix}, \ \boldsymbol{\mu} = \begin{bmatrix} M_1 \\ M_2 \\ M_3 \end{bmatrix}, \ \mathbf{q} = \begin{bmatrix} q_1 \\ q_2 \\ q_3 \end{bmatrix}, \ \mathbf{m} = \begin{bmatrix} m_1 \\ m_2 \\ m_3 \end{bmatrix}. \tag{4.24}$$

Differently from the system formed by the equilibrium equations in the plane case, the system from Equation (4.21) presents the different directions components influence. Consequently, it is necessary to solve all the components simultaneously, therefore a third order differential equation. Solving it analogously as performed for the Equations (4.1), (4.2) and (4.3) a negative root of the characteristic equation was found generating sines and cosines terms. Hence, the solution can be written as

$$N_1(S) = -\frac{C_1 \text{ sen}\left(\sqrt{P}S\right) + C_2 \cos\left(\sqrt{P}S\right)}{\sqrt{P}} - ZS + C_3, \tag{4.25}$$

$$N_2(S) = \frac{C_1 \cos\left(\sqrt{P}S\right) + C_2 \text{ sen}\left(\sqrt{P}S\right) - Z + q_1}{\kappa}, \tag{4.26}$$

$$N_3(S) = \frac{-C_1\,\tau \text{ sen}\left(\sqrt{P}S\right) + C_2\,\tau \cos\left(\sqrt{P}S\right)}{\kappa\sqrt{P}} + \frac{\kappa}{\tau}(-ZS + C_3) + \frac{q_2}{\tau}, \tag{4.27}$$

where P and Z are defined as

$$\begin{aligned} P &= \kappa^2 + \tau^2, \\ Z &= \frac{\tau\,(\tau\,q_1 + q_3\kappa)}{P}. \end{aligned} \tag{4.28}$$

Analogously, to obtain the moment equations solution the expressions found for N_2 and N_3, in Equations (4.22), were used producing:

$$
\begin{aligned}
M_1 = &\left(\frac{C_1\,2\,\tau}{\sqrt{P}} - C_2\,\tau\,S - C_4\,\sqrt{P}\right)\frac{\operatorname{sen}\left(\sqrt{P}S\right)}{P} + \\
&+ \left(-C_1\,\tau\,S - \frac{C_2\,\tau}{\sqrt{P}} + C_5\,\sqrt{P}\right)\frac{\cos\left(\sqrt{P}S\right)}{P} + \\
&+ \left(m_3\tau\,\kappa\,P + 2\,\kappa^2 q_1\tau + \tau^2 m_1 P + q_3\kappa\,P\right)\frac{S}{P^2} + C_6,
\end{aligned}
\tag{4.29}
$$

$$
\begin{aligned}
M_2 = &\left(-C_1\,\tau\,P + C_2\,\tau\,SP^{3/2} + C_4\,P^2\right)\frac{\cos\left(\sqrt{P}S\right)}{P^2\kappa} + \\
&+ \left(C_5\,P^2 - C_1\,\tau\,P^{3/2}S\right)\frac{\operatorname{sen}\left(\sqrt{P}S\right)}{P^2\kappa} + \\
&+ \frac{m_1\kappa^2 P - m_3\tau\,\kappa\,P - q_3\kappa\,P - 2\,\kappa^2 q_1\tau}{P^2\kappa},
\end{aligned}
\tag{4.30}
$$

$$
\begin{aligned}
M_3 = &\left(-C_1\tau^2 S + \frac{C_2\kappa^2}{\sqrt{P}} + C_5\tau\,\kappa\sqrt{P}\right)\frac{\cos\left(\sqrt{P}S\right)}{P\kappa} + \\
&+ \left(\frac{C_1\,(\tau-\kappa)\,(\tau+\kappa)}{\sqrt{P}} - C_2\tau^2 S - C_4\sqrt{P}\tau\right)\frac{\operatorname{sen}\left(\sqrt{P}S\right)}{P\kappa} + \\
&+ \frac{\left(-m_1\tau\,P - m_3\kappa\,P - q_1\,(\tau-\kappa)\,(\tau+\kappa) + 2\,q_3\tau\,\kappa\right)\kappa\,S}{P^2} + \\
&+ \frac{-q_2 + m_2\tau + \kappa\,C_6\,\tau - \kappa\,C_3}{\tau^2}.
\end{aligned}
\tag{4.31}
$$

With these equations of N_i and M_i internal forces and moments can be determined for any geometry considering κ and τ constants. Thus, one can determine the wire behavior using the desired geometry and boundary conditions.

Once again, in order to determine the mechanical behavior of the model, the stresses and strains were calculated. Substituting the results obtained previously the strains are written as

$$\varepsilon_1 = \frac{C_1\, P \operatorname{sen}\left(\sqrt{P}S\right) - C_2\, P \cos\left(\sqrt{P}S\right) + C_3\, P^{3/2} + (-\tau\, q_1 - q_3\kappa)\, S\sqrt{P}\tau}{P^{3/2} E A}, \tag{4.32}$$

$$\varepsilon_2 = \frac{\cos\left(\sqrt{P}S\right)\ C1\ P + \operatorname{sen}\left(\sqrt{P}S\right)\ C_2\, P + \kappa\ (\kappa\, q_1 - \tau\, q_3)}{P\kappa\, A\, G}, \tag{4.33}$$

$$\varepsilon_3 = \frac{\dfrac{-C_1\,\tau\ \operatorname{sen}\left(\sqrt{P}S\right) + C_2\,\tau\ \cos\left(\sqrt{P}S\right)}{\kappa\sqrt{P}} - \dfrac{\kappa}{\tau}\left(\dfrac{\tau\ (\tau\, q_1 + q_3\kappa)\, S}{P} - C_3\right) + \dfrac{q_2}{\tau}}{AG}, \tag{4.34}$$

and for the deflections, analogously to the arc case, were calculated as

$$\begin{aligned}
\rho_1 = &\left(\frac{C_1\, 2\,\tau}{\sqrt{P}} - C_2\,\tau\, S - C_4\,\sqrt{P}\right)\frac{\operatorname{sen}\left(\sqrt{P}S\right)}{P\, G\, J} + \\
&+ \left(-C_1\,\tau\, S - \frac{C_2\,\tau}{\sqrt{P}} + C_5\,\sqrt{P}\right)\frac{\cos\left(\sqrt{P}S\right)}{P\, G\, J} + \\
&+ \left(m_3\tau\,\kappa\, P + 2\,\kappa^2 q_1\tau + \tau^2 m_1 P + q_3\kappa\, P\right)\frac{S}{P^2\, G\, J} + \frac{C6}{GJ},
\end{aligned} \tag{4.35}$$

$$\begin{aligned}
\rho_2 = &\left(C_1\tau^2 S - \frac{C_2\kappa^2}{\sqrt{P}} - C_5\tau\,\kappa\sqrt{P}\right)\frac{r\cos\left(\sqrt{P}S\right)}{P\kappa\, EI} + \\
&+ \left(\frac{-C_1\,(\tau-\kappa)\,(\tau+\kappa)}{\sqrt{P}} + C_2\tau^2 S + C_4\sqrt{P}\tau\right)\frac{r\operatorname{sen}\left(\sqrt{P}S\right)}{P\kappa\, EI} + \\
&+ \frac{(m_1\tau\, P + m_3\kappa\, P + q_1\,(\tau-\kappa)\,(\tau+\kappa) - 2\, q_3\tau\,\kappa)\, r\kappa\, S}{P^2\, EI} + \\
&+ \frac{(q_2 - m_2\tau - \kappa\, C_6\,\tau + \kappa\, C_3)\, r}{\tau^2\, EI},
\end{aligned} \tag{4.36}$$

$$\rho_3 = \left(C_1\,\tau\,P - C_2\,\tau\,SP^{3/2} - C_4\,P^2\right)\frac{r\cos\left(\sqrt{P}S\right)}{P^2\kappa\,EI} + \\ + \left(C_1\,\tau\,P^{3/2}S - C_5\,P^2\right)\frac{r\,\mathrm{sen}\,\left(\sqrt{P}S\right)}{P^2\kappa\,EI} + \\ + \frac{\left(-m_1\kappa^2P + m_3\tau\,\kappa\,P + q_3\kappa\,P + 2\,\kappa^2 q_1\tau\right)r}{P^2\kappa\,EI}. \tag{4.37}$$

From this expressions, the rotations were initially determined. Using the equations of equilibrium (3.42) and the results obtained one can write,

$$\frac{d\phi_1\,(S)}{dS} - \kappa\,\phi_2\,(S) = \left(\frac{C_1\,2\,\tau}{\sqrt{P}} - C_2\,\tau\,S - C_4\,\sqrt{P}\right)\frac{\mathrm{sen}\,\left(\sqrt{P}S\right)}{P\,G\,J} + \\ + \left(-C_1\,\tau\,S - \frac{C_2\,\tau}{\sqrt{P}} + C_5\,\sqrt{P}\right)\frac{\cos\left(\sqrt{P}S\right)}{P\,G\,J} + \\ + \left(m_3\tau\,\kappa\,P + 2\,\kappa^2 q_1\tau + \tau^2 m_1 P + q_3\kappa\,P\right)\frac{S}{P^2\,G\,J} + \frac{C6}{GJ}, \tag{4.38}$$

$$\frac{d\phi_2\,(S)}{dS} + \kappa\,\phi_1\,(S) - \tau\,\phi_3\,(S) = \left(C_1\tau^2 S - \frac{C_2\kappa^2}{\sqrt{P}} - C_5\tau\,\kappa\sqrt{P}\right)\frac{r\cos\left(\sqrt{P}S\right)}{P\kappa\,EI} + \\ + \left(\frac{-C_1\,(\tau-\kappa)\,(\tau+\kappa)}{\sqrt{P}} + C_2\tau^2 S + C_4\sqrt{P}\tau\right)\frac{r\,\mathrm{sen}\,\left(\sqrt{P}S\right)}{P\kappa\,EI} + \\ + \frac{\left(m_1\tau\,P + m_3\kappa\,P + q_1\,(\tau-\kappa)\,(\tau+\kappa) - 2\,q_3\tau\,\kappa\right)r\kappa\,S}{P^2\,EI} + \\ + \frac{\left(q_2 - m_2\tau - \kappa\,C_6\,\tau + \kappa\,C_3\right)r}{\tau^2\,EI}, \tag{4.39}$$

$$\frac{d\phi_3\,(S)}{dS} + \tau\,\varphi_2\,(S) = \left(C_1\,\tau\,P - C_2\,\tau\,SP^{3/2} - C_4\,P^2\right)\frac{r\cos\left(\sqrt{P}S\right)}{P^2\kappa\,EI} + \\ + \left(C_1\,\tau\,P^{3/2}S - C_5\,P^2\right)\frac{r\,\mathrm{sen}\,\left(\sqrt{P}S\right)}{P^2\kappa\,EI} + \\ + \frac{\left(-m_1\kappa^2P + m_3\tau\,\kappa\,P + q_3\kappa\,P + 2\,\kappa^2 q_1\tau\right)r}{P^2\kappa\,EI}. \tag{4.40}$$

To determine the complete mechanical response of the strand, the differential system of equations must be solved. Thus, the solution of the rotation system [Zhu e Zhao, 2008] can be obtained as,

$$\boldsymbol{\phi} = \boldsymbol{\phi_0} + \int_0^S \mathbf{T}^{-1}\boldsymbol{\rho}\; dS. \tag{4.41}$$

Each component of deflection, in the local system so far, were represented in the global system, after the multiplication by $\boldsymbol{T}^{-1}$, and then integrated. The result was added to a constant $\boldsymbol{\phi_0}$, result from the integration, and the global response set. To obtain local outcomes, the multiplication by $\boldsymbol{T}$ could be performed.

The displacements were calculated using the same procedure. The expression for the solution of the system (3.40) is written as,

$$\boldsymbol{u} = \boldsymbol{u_0} + \int_0^S \boldsymbol{\phi} + \mathbf{T}^{-1}\boldsymbol{\varepsilon}\; dS. \tag{4.42}$$

The results from the global rotation ($\boldsymbol{\phi}$) were used, therefore, when added to the strains, transformed to the global system as well. Again, $\boldsymbol{u_0}$ denotes the integration constant. Hence, the following set of equation the displacement equilibrium system, was solved:

$$\begin{aligned}
&\frac{du_1\,(S)}{dS} - \kappa\, u_2\,(S) = \\
&= \frac{C_1\, P \operatorname{sen}\left(\sqrt{P}S\right) - C_2\, P \cos\left(\sqrt{P}S\right) + C_3\, P^{3/2} + (-\tau\, q_1 - q_3\kappa)\, S\sqrt{P}\tau}{P^{3/2} E A}, \\
&\frac{du_2\,(S)}{dS} + \kappa\, u_1\,(S) - \tau\, u_3\,(S) - \varphi_3 = \\
&= \frac{\cos\left(\sqrt{P}S\right)\; C1\; P + \operatorname{sen}\left(\sqrt{P}S\right)\; C_2\, P + \kappa\; (\kappa\, q_1 - \tau\, q_3)}{P\kappa\, A\, G}, \\
&\frac{du_3\,(S)}{dS} + \tau\, u_2\,(S) + \varphi_2 = \\
&= \frac{-C_1\,\tau\, \operatorname{sen}\left(\sqrt{P}S\right) + C_2\,\tau\, \cos\left(\sqrt{P}S\right)}{\kappa\sqrt{P}} - \frac{\kappa}{\tau}\left(\frac{\tau\; (\tau\, q_1 + q_3\kappa)\, S}{P} - C_3\right) + \frac{q_2}{\tau}, \\
&\qquad\qquad AG
\end{aligned} \tag{4.43}$$

The expressions obtained were very difficult to handle and demonstrated the complexity of the analyzed theory. Numerical results were generated, in the next chapter, in order to validate the methodology used.

An expression to characterize a wire was obtained analytically using the spatial beam theory. Moreover, this expression present a reference point for other methodologies, to be used either as a validation tool (combined with other methodologies) or a rapidly evaluation of the mechanical behavior. Since the equations depend on the material and geometry, though having some considerations, they could be applied for different cases and applications.

Time of analysis is a relevant parameter to be considered in a study. The computational cost or the experiment difficulty could be used only for complex cases and to if one uses this set of equations for different project demands on distinct cases.

Application of analytic models are necessary in engineering. Every method, either numerical or experimental are dependent on posterior validation before begining complex simulations. Any software, at certain point, was compared to this kind of benchmark solution [Feyrer, 2007]. The solutions obtained allow the mechanical behavior understanding when the application of such structures is considered.

Not only the geometry and material could be modified for a different case, but also the boundary conditions. Since no information regarding the fixation was given, the constants of integration must be determined accordingly. This versatility is one of the great aspects of the proposed methodology. Without mentioning that strains and stresses, formulated here, can be applied in optimization methods, allowing determination of analytic sensibilities.

As any other methodology, there are some limitations imposed to provide these results. It is important to understand that the hypothesis used are

- No body forces;
- No contact or slippage between strands or core;
- Isotropic and linear material;
- A strand parameterized as an helix, or, parameters κ and τ constants;

The expressions were obtained applying the spatial beam theory. Consequently, using these equations are not restricted to model cables. Any structure that can be parameterized as an helix, or a geometry with κ and τ as constants, e. g.,springs are an example.

4.3 Straight Beam

Another particular case of the methodology used is obtained when $\alpha = 90°$. As a result, both curvature and torsion are null. Since Equations (2.22) and (2.23) depend on a cosine, and $\cos(90°) = 0$, they are also zero. Therefore, there is no change in the direction or sense of the tangent vector, i.e., the normal and binormal vector does not exist. Consequently, the parametrization results in a straight line.

With the equations system formed by (2.16), (2.17) and (2.18) and adopting $S = z$, all the parameters needed to study this geometry is known. Consequently, the matrix $\mathbf{T}_{FS} = \mathbf{0}$ and the remaining terms are

$$\frac{d\boldsymbol{\eta}}{dS} + \mathbf{q} = \mathbf{0}, \tag{4.44}$$

$$\frac{d\boldsymbol{\mu}}{dS} - \boldsymbol{\Psi}_{23}\boldsymbol{\eta} + \mathbf{m} = \mathbf{0}. \tag{4.45}$$

The spatial beam theory when reduced to this case represents the Euler-Bernoulli beam equation, that is, not only the parametrization, but also the equilibrium equations can be written for the simplest cases.

This configuration set can be used to analyze the center of the cable, since it is considered straight and may not present curvature and torsion. In this work, the core was not focused due to the triviality of this solution.

To determine the mechanical behavior of the proposed method, the boundary conditions were applied to calculate the constants. Using the Frenet-Serret triad, the loads were applied in the local system. The next chapter presents this methodology and the results validation.

5. RESULTS

With the expressions obtained analytically it is possible to analyze the mechanical behavior of the strand facing several types of loading. In order to determine the validity of the theory, four cases were simulated using FEM and the proposed methodology. To do so, not only the geometry must be informed, but also the constants of integration need to be derived.

The analysis of all the cases start from the clamped end ($S = 0$) and develops to the free edge, where the loads are applied. This chapters explore the results obtained and the comparison with FEM.

5.1 Determination of Constants

The expressions obtained in the solution of the Equations (3.9) and (3.17) with the boundary conditions were used to determine the first three integration constants, generated by the integration of the differential equilibrium equations. In this case, one end is considered clamped and different loads are applied at the other end.

It is important to notice that the equilibrium equations are presented in a local system, i.e., the mechanical response generated by the methodology here presented is not in the same coordinate system that the force and BC are applied (global). Consequently, the calculation of the constants is not direct - the transformation of the BC must be firstly performed. As the Frenet-Serret basis was defined in Equation (2.20), the load vector can be written as,

$$\mathbf{F} = \begin{bmatrix} V_x \\ V_y \\ V_z \end{bmatrix}, \tag{5.1}$$

the multiplication of these entities produce the effect of the applied force in the local system, so

$$F_L = \begin{bmatrix} -\operatorname{sen}\left(\dfrac{S\cos(\alpha)}{R}\right)\cos(\alpha)\,V_x + \cos\left(\dfrac{S\cos(\alpha)}{R}\right)\cos(\alpha)\,V_y + \operatorname{sen}(\alpha)\,V_z \\ \cos\left(\dfrac{S\cos(\alpha)}{R}\right)V_x + \operatorname{sen}\left(\dfrac{S\cos(\alpha)}{R}\right)V_y \\ -\operatorname{sen}(\alpha)\operatorname{sen}\left(\dfrac{S\cos(\alpha)}{R}\right)V_x + \operatorname{sen}(\alpha)\cos\left(\dfrac{S\cos(\alpha)}{R}\right)V_y - \cos(\alpha)\,V_z \end{bmatrix} + \begin{bmatrix} Q_x \\ Q_y \\ Q_z \end{bmatrix}. \tag{5.2}$$

And the second vector is used in case of a distributed load represented as:

$$Q_x = \int_0^{S_{max}} \left[-\operatorname{sen}\left(\frac{S\cos(\alpha)}{R}\right)\cos(\alpha)\,q_1 + \cos\left(\frac{S\cos(\alpha)}{R}\right)q_2 + -\operatorname{sen}(\alpha)\operatorname{sen}\left(\frac{S\cos(\alpha)}{R}\right)q_3 \right] dS \tag{5.3}$$

$$Q_y = \int_0^{S_{max}} \left[\cos\left(\frac{S\cos(\alpha)}{R}\right)\cos(\alpha)\,q_1 - \operatorname{sen}\left(\frac{S\cos(\alpha)}{R}\right)q_2 + \operatorname{sen}(\alpha)\cos\left(\frac{S\cos(\alpha)}{R}\right)q_3 \right] dS \tag{5.4}$$

$$Q_z = \int_0^{S_{max}} \left[\operatorname{sen}(\alpha)\,q_1(S) - q_3\cos(\alpha)\right] dS \tag{5.5}$$

Once the distributed loads q_1, q_2 and q_3 are defined, the integration can be performed in order to define the boundary condition for this case. Therefore, N_1, N_2 and N_3 (expressions obtained for each case in Chapter 4) are set equal to the reaction at the clamped end ($S = 0$). Consequently, the equations have no dependence on S anymore, and the only unknown parameters are C_1, C_2 and C_3.

It is possible to observe that the second term of Equation 5.2 has no influence of the component V_z, consequence from the orthogonality of $\boldsymbol{n}$ and x_3 on every S.

In view of the helix angle, the triad ($\boldsymbol{t}$, $\boldsymbol{n}$, $\boldsymbol{b}$) is also rotated in reference of the global system. Therefore, there is a component of V_z in the x_1 direction, otherwise, there should be only one component in x_3 due to the parallelism of the local and global systems. The boundary conditions for the moments can be obtained adopting the same procedure. The remaining three constants (C_4, C_5 and C_6) from the integration of moments were obtained

similarly.

The position vector, defined by the parameterization in Equations (2.16), (2.17) and (2.18), was used to determine the local length between the force vector in Equation (5.1) and the clamped end. To do so, S is defined as the final position (S_{max} from Equation (2.24)). By the same procedure used to define the Equation(5.2), using the transformation matrix it is possible to analyze the local effects as:

$$M_{BC_L} = \begin{bmatrix} M^1_{BC_L} \\ M^2_{BC_L} \\ M^3_{BC_L} \end{bmatrix} + \begin{bmatrix} M^1_d \\ M^2_d \\ M^3_d \end{bmatrix}. \tag{5.6}$$

where,

$$\begin{aligned} M^1_{BC_L} =& \left[\cos(\alpha)\, S_{max} - \text{ sen }(\theta_{max})\, R\right] \text{sen }(\alpha)\ V_x + \left[\cos(\theta_{max}) - 1\right] \text{sen }(\alpha)\, R\, V_y + \\ &+ \left[1 - \cos(\theta_{max})\right] \cos(\alpha)\, R\, V_z, \end{aligned} \tag{5.7}$$

$$M^2_{BC_L} = -S_{max} \text{sen }(\alpha)\ V_y + R \text{sen }(\theta_{max})\ V_z + R_e V_z, \tag{5.8}$$

$$\begin{aligned} M^3_{BC_L} =& \left[S_{max} - S_{max} \cos^2(\alpha) + \cos(\alpha)\, R \text{sen }(\theta_{max})\right] V_x + \\ &+ \left[1 - \cos(\theta_{max})\right] \cos(\alpha)\, R\, V_y + \left[1 - \cos(\theta_{max})\right] \text{sen }(\alpha)\, R\, V_z. \end{aligned} \tag{5.9}$$

Considering R_e as the eccentricity in case of a load applied out of the helix, producing a resultant, and constant, moment in the component $M^2_{BC_L}$. If the load is acting at the center $R_e = R$ and if the load is at the helix $R_e = 0$.

The second vector is used in case of a distributed load. The transformation matrix was used to obtain the local components, then it was multiplied by the position vector (the lever arm that produces the moment). Finally, the integration was performed to account for all the effect from the clamped end to the free end, so

$$M_d^1 = \int_0^{S_{max}} \Bigg[\left(\cos\left(\frac{S\cos(\alpha)}{R}\right)\cos(\alpha) + R\,\text{sen}\left(\frac{S\cos(\alpha)}{R}\right)\text{sen}\,(\alpha)\right) q_1 + \\ + \text{sen}\left(\frac{S\cos(\alpha)}{R}\right) q_2 + \cos\left(\frac{S\cos(\alpha)}{R}\right) S\,\text{sen}\,(\alpha)^2\, q_3 - \\ - \cos(\alpha)\, R\,\text{sen}\left(\frac{S\cos(\alpha)}{R}\right) q_3 \Bigg] dS, \tag{5.10}$$

$$M_d^2 = \int_0^{S_{max}} \Bigg[\left(R\left(\cos\left(\frac{S\cos(\alpha)}{R}\right) - 1\right) - \text{sen}\left(\frac{S\cos(\alpha)}{R}\right)\cos(\alpha)\, S\right)\text{sen}\,(\alpha)\, q_1 + \\ + \cos\left(\frac{S\cos(\alpha)}{R}\right) S\,\text{sen}\,(\alpha)\;\; q_2 - \text{sen}\left(\frac{S\cos(\alpha)}{R}\right) S\,\text{sen}\,(\alpha)^2\, q_3 + \\ \left(R\cos\left(\frac{S\cos(\alpha)}{R}\right) - R\right)\cos(\alpha)\, q_3 \Bigg] dS, \tag{5.11}$$

$$M_d^3 = \int_0^{S_{max}} \Bigg[\left(1 - \cos\left(\frac{S\cos(\alpha)}{R}\right)\right) R\cos(\alpha)\, q_1 - R\,\text{sen}\left(\frac{S\cos(\alpha)}{R}\right) q_2 \\ \left(1 - \cos\left(\frac{S\cos(\alpha)}{R}\right)\right) R\,\text{sen}\,(\alpha)\, q_3 \Bigg] dS. \tag{5.12}$$

Therefore, one must solve firstly the three equations (N_i) where only C_1, C_2 and C_3 are present, and then the remaining constants. This is due to the couple effect of the moments and forces for any condition, even if the curvature (κ) and/or the torsion (τ) are zero. The constants determination is dependent to the boundary conditions.

5.2 FEM Model

The helix parameterization, Equations (2.16), (2.17) and (2.18), was used to generate the geometry on a commercial finite element software [ANSYS, 2012]. To do so, 100 elements were used since the selected beam element presents a mid node which means the element has a quadratic interpolation function. A sufficient quantity was used to generate the structure and to does not influence the numerical results.

Concentrated forces and moments were applied globally at the last node and the clamped end was set in the first node. Distributed loads were introduced in the model according to the element, or local, system.

Two sets of geometry were analyzed (with different loads), as mentioned before, by changing the helix angle α. The FEM and analytical results are compared in the following sections.

5.3 Concentrated Loads

Results from the proposed methodology were obtained considering the local coordinate S. This parameter defines the position along the parametrized geometry.

5.3.1 The Plane Arc Case

Initially, the arc geometry was defined. To generate the structure, α was defined as zero, so parameters κ (Equation 2.22), τ (Equation 2.23), S_{max} (Equation 2.24), were defined as shown in Table 5.1, which resulted in $\theta_{max} = 360°$. The values for I and J are shown ass well so that the geometry is defined.

Table 5.1 – Plane arc geometric parameters.

α [°]	κ $[m^{-1}]$	τ $[m^{-1}]$	S_{max} $[m]$	I $[m^4]$	J $[m^4]$
0	10	0	0.628316	7.85398×10^{-9}	1.57080×10^{-8}

The material parameters used to obtain the results are shown in Table 5.2.

Table 5.2 – Plane arc material parameters.

ν [ ]	E $[GPa]$	G $[GPa]$
0.3	210	80.7692

Also, the Frenet-Serret basis was completely defined as

$$T_{arc} = \begin{bmatrix} -\text{sen }(10S) & \cos(10S) & 0 \\ \cos(10S) & \text{sen }(10S) & 0 \\ 0 & 0 & -1 \end{bmatrix} \tag{5.13}$$

Equation (5.13) shows that all the values concerning the x_3 axes are constant, that is, the rotation is in this direction and there is no change in the angle formed by the arc and the x_1x_2 plane ($\alpha = 0°$).

So, the boundary condition on the clamped end can be applied. Equation (5.2) are used with the arc geometry (null helix angle), therefore one can write:

$$F_{arc} = \begin{bmatrix} -\text{sen }(10\ S)\, V_x + \cos(10\ S)\, V_y \\ \cos(10\ S)\, V_x + \text{sen }(10S)\, V_y \\ -V_z \end{bmatrix} \tag{5.14}$$

Component V_z is parallel to x_3, consequently, its effect is only present in the last term. Also, once more, because of the orthogonality, the loads contained in the osculating plane affect only $\boldsymbol{t}$ and $\boldsymbol{n}$. Equations (5.13) and, consequently, (5.14) show the decoupling between in-plane and out-plane effects, resulting in the possibility of solving the problem separately, a consequence of the arc's geometry.

At the clamped end S is defined as zero. Therefore, this value was an input in the equilibrium equations. The remaining parameters were calculated as equal to the boundary condition. So, C_1, C_2 and C_3 are expressed as:

$$\begin{aligned} C_1 &= V_y - 0.1\ q_2 \\ C_2 &= V_x + 0.1\ q_1 \\ C_3 &= -\ V_z \end{aligned} \tag{5.15}$$

Analogously, substituting $S = 0$ in Equations (4.10), (4.11) and (4.12) and using the moment boundary condition, defined in Equation (5.6), the remaining constants are found to be:

$$\begin{aligned} C_4 &= -0.1\ V_z - 0.1\ m_2 \\ C_5 &= 0.01\ q_1 + 0.1\ m_1 \\ C_6 &= -0.1\ V_y + 0.01\ q_2 \end{aligned} \tag{5.16}$$

Therefore, the expressions can be compared against the results from FEM (there results are presented as *num* in the plotted graphics.). The full expressions considering the constants are written as

$$N_{arc} = \begin{bmatrix} -\text{ sen }(10S)\, V_x - 0.1\,\text{sen }(10S)\, q_1 + \cos(10S)\, V_y - 0.1\cos(10S)\, q_2 + 0.1 q_2 \\ \cos(10S)\, V_x + 0.1\cos(10S)\, q_1 + \text{ sen }(10S)\, V_y - 0.1\,\text{sen }(10S)\, q_2 - 0.1 q_1 \\ -q_1 S - V_z \end{bmatrix}, \tag{5.17}$$

and the moments

$$M_{arc} = \begin{bmatrix} M_{1arc} \\ M_{2arc} \\ M_{3arc} \end{bmatrix}. \tag{5.18}$$

where

$$\begin{aligned} M_{1arc} = &-0.01\,\text{sen }(10S)\, q_1 - 0.1\,\text{sen }(10S)\, m_1 + 0.1\,\text{sen }(10S)\, V_z - \\ &+ 0.1\cos(10S)\, m_2 + V_z + 0.1 m_2 + 0.1 q_1 S + 0.1 V_z, \end{aligned} \tag{5.19}$$

$$\begin{aligned} M_{2arc} = &\ 0.01\cos(10S)\, q_1 + 0.1\cos(10S)\, m_1 - 0.1\cos(10S)\, V_z - \\ &+ 0.1\,\text{sen }(10S)\, m_2 + V_z - 0.01 q_1 - 0.1 m_1, \end{aligned} \tag{5.20}$$

$$\begin{aligned} M_{3arc} = &-0.1\,\text{sen }(10S)\, V_x - 0.01\,\text{sen }(10S)\, q_1 + 0.1\cos(10S)\, V_y - \\ &+ 0.01\cos(10S)\, q2 - 0.9 q_1 S + 0.01 q_1 - 0.1 V_x. \end{aligned} \tag{5.21}$$

As stated before, with respect to the loading and the local-global transformations matrix, the results for forces and moments follow the expected decoupling: in-plane normal

and shear forces (N_1 and N_2) are coupled and generate M_3; out-plane shear force N_3 develops both M_1 and M_2.

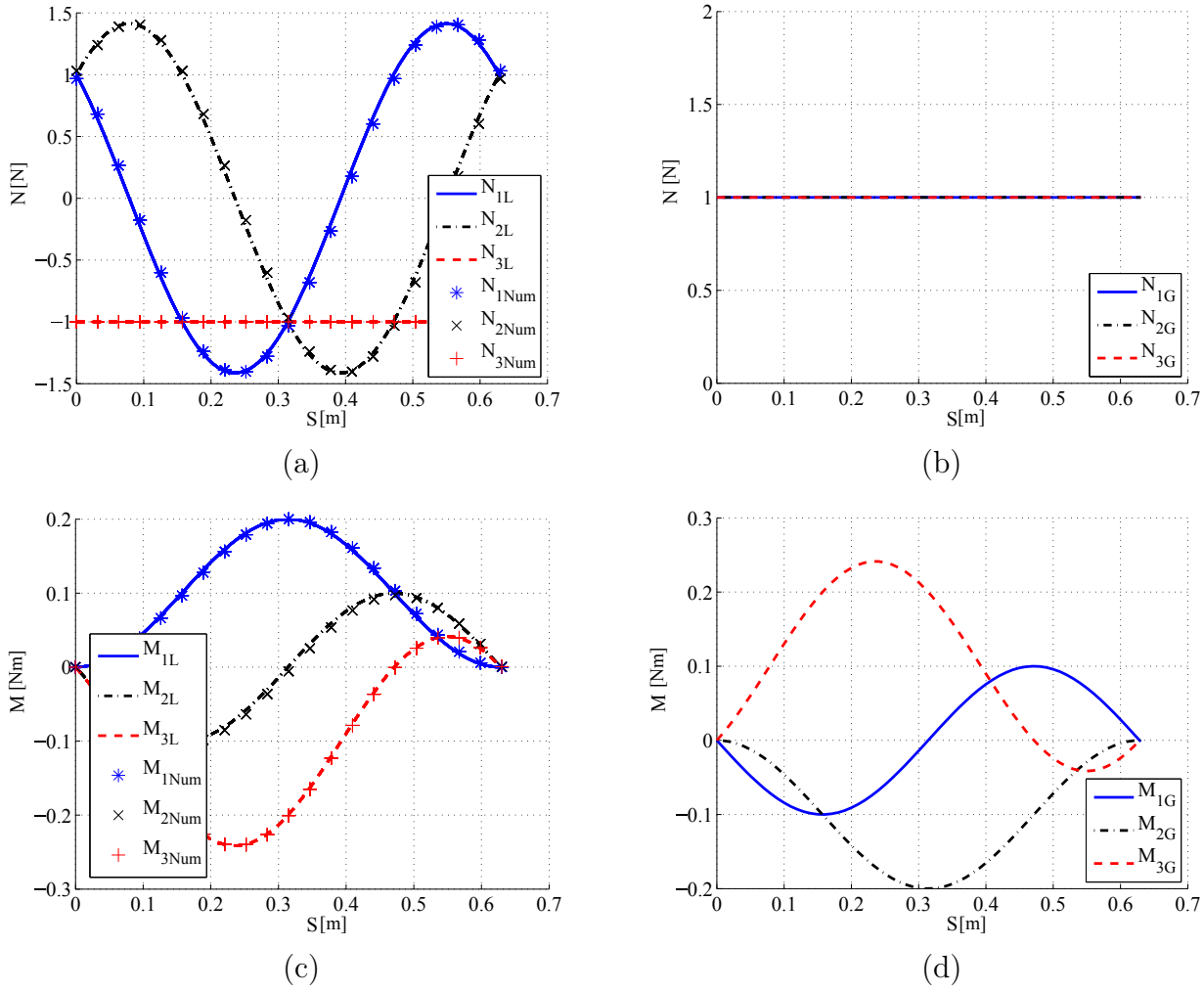

Figure 5.1 – V_x, V_y and V_z applied to the arc with (a) local and (b) global forces and (c) local and (d) global moments.

In Figure 5.1, both local and global results are plotted for concentrated unitary loads V_x, V_y and V_z applied together. The first graphic, Figure 5.1 (a), shows the local force at the clamped end the components are equal to the reaction. As the coordinate S develops, N_1 decreases due to the local decomposition until zero, where it is orthogonal to the load resultant. Once aligned to the applied force the values are maximum, in modulus.

Whenever N_1 is parallel to the load, N_2 is orthogonal, and vice-versa. This means that once one component reaches its maximum the other is zero. Both variables presented

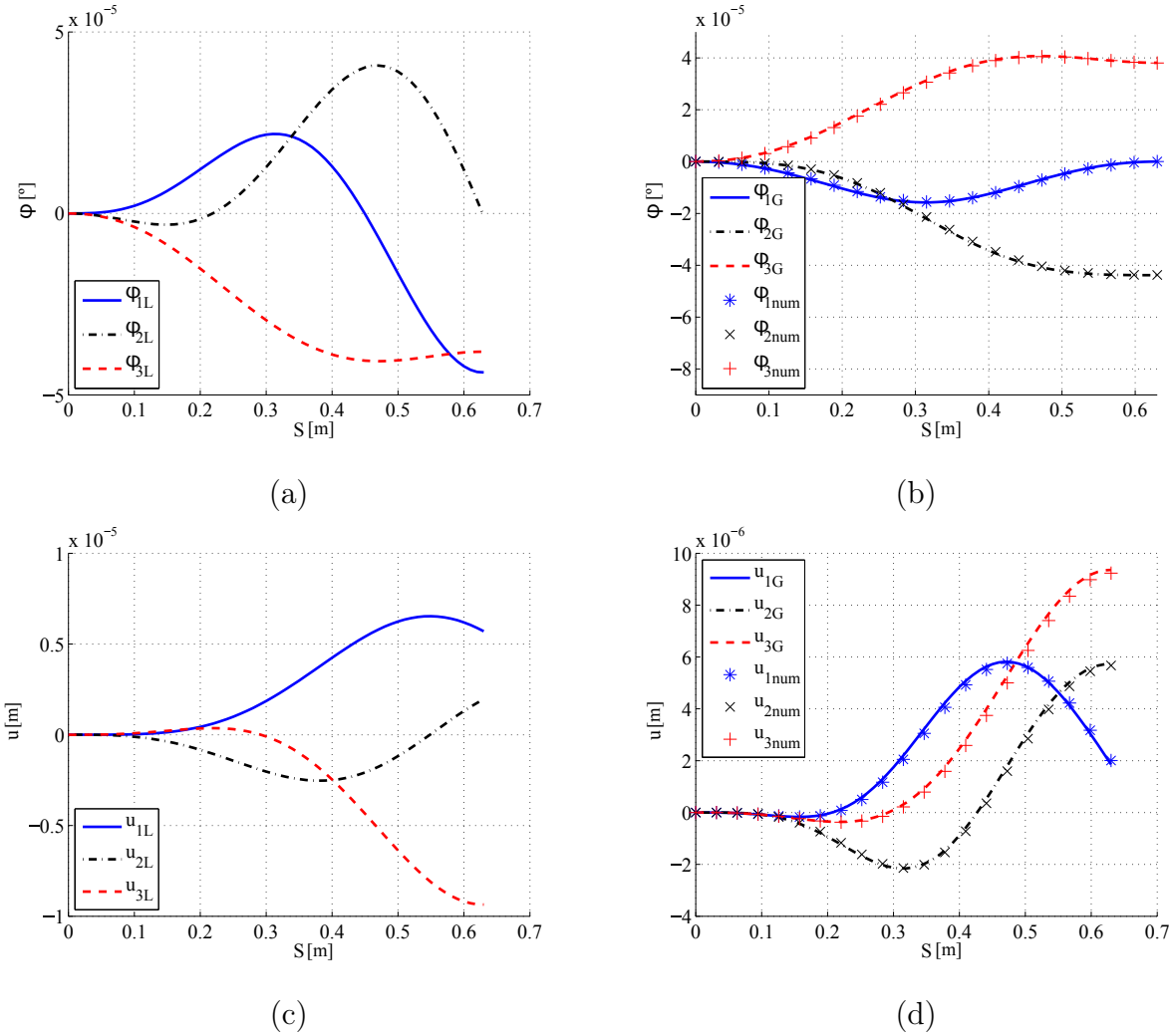

Figure 5.2 – Arc (a) local and (b) global rotations and (c) local displacements and (d) global.

a similar behavior while N_3 is constant or aligned to V_z along the arc.

Global forces were determined as constants in Figure 5.1 (b). No decomposition is needed since the loads are parallel to x_1, x_2 and x_3. Therefore, the effect is constant along S.

Local moments are analyzed in Figure 5.1 (c). The first component reaches the maximum value at the mid point, where the distance from the clamped end is higher ($2R$). At $S = \frac{S_{max}}{4}$ and $S = \frac{3S_{max}}{4}$, M_2 is maximum, though with opposite sign, since the force decomposition results in the unitary load applied in this direction. Three forces together produced a load not aligned to any axis and M_3 is only affected by this lack of parallelism.

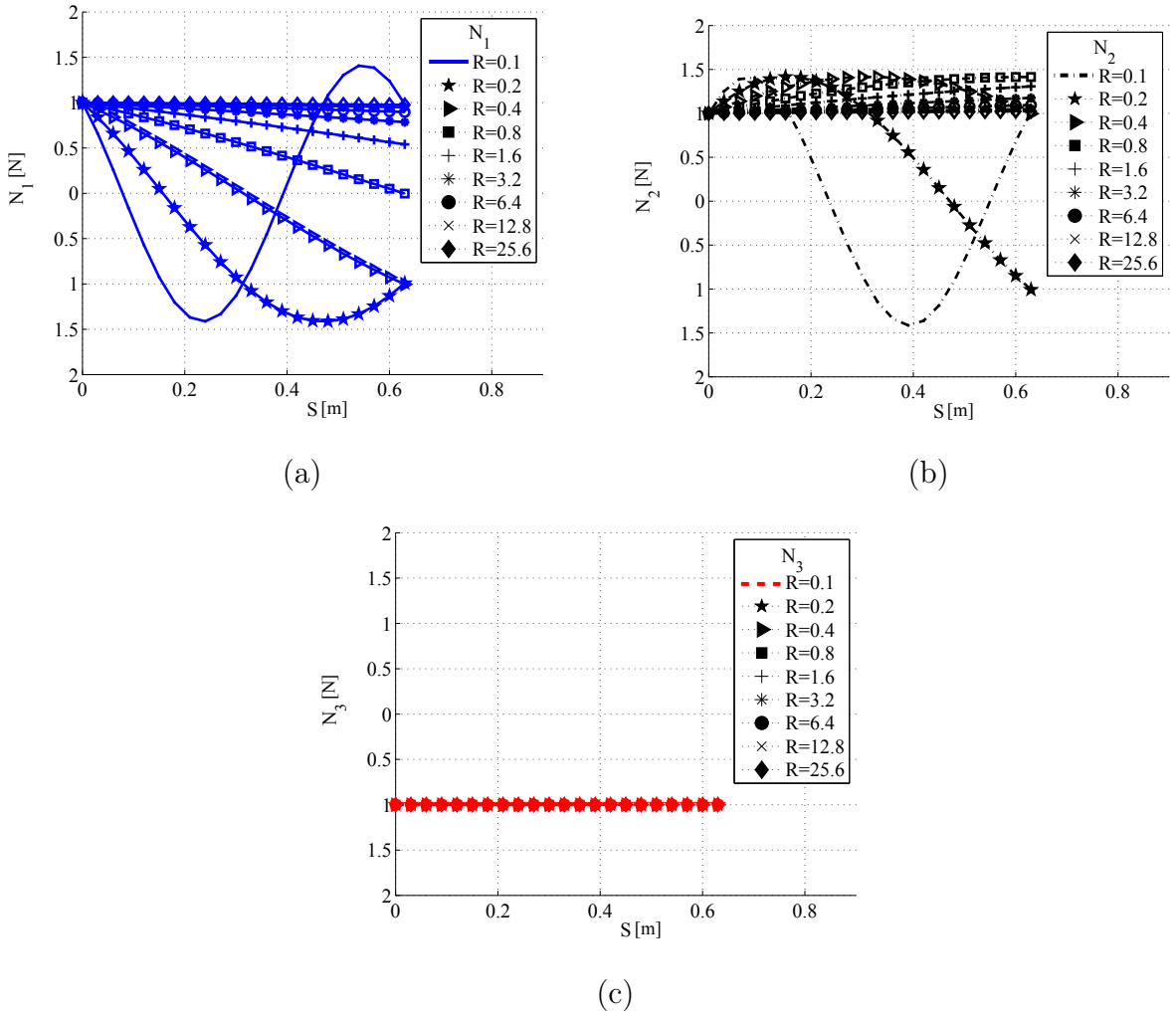

Figure 5.3 – Forces diagram for the arc radius growing (a) N_1 (b) N_2 and (c) N_3.

Therefore its maximum value is not in any quadrant end, but dislocated, and greater than the others.

To determine the global moments the transformation matrix is used. Since $\alpha = 0$ the osculating plane is contained in to x_2x_1 and $\boldsymbol{b}$ is always parallel to x_3. Consequently, the behaviors are similar as shown in Figure 5.1 (d).

Strains and stresses were defined by the presented methodology (Equations (4.13), (4.14), (4.15), (4.16), (4.17) and (4.18)). These values were then applied to determine rotations and displacements. Using these expression in the equilibrium Equations (4.19) the boundary conditions were applied.

As the end is clamped, the value for local and global displacements and rotations

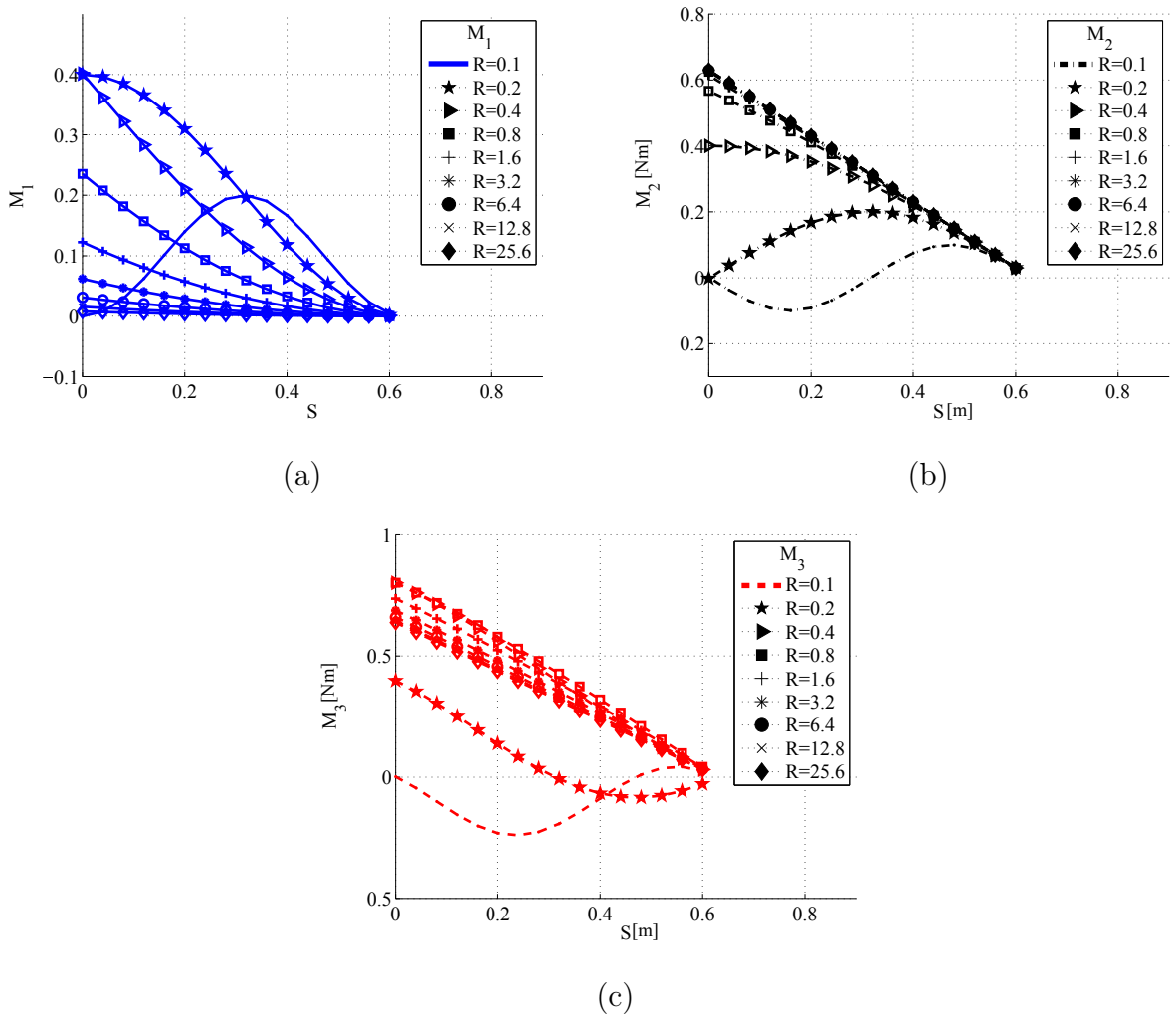

Figure 5.4 – Local moments considering the components (a) M_1, (b) M_2 and (c) M_3.

at $S = 0$ are also zero, as shown in Figure 5.2 (a). The components ϕ_1 and ϕ_3 reach approximately the same maximum, in modulus at the free end while ϕ_2 is zero.

Global rotations are shown in Figure 5.2 (b). While ϕ_2 and ϕ_3 increase from the clamped end to the applied load position, the first component reaches the highest value at the middle of the arc and decreases until zero.

The displacements in local coordinates are plotted in Figure 5.2 (c) while the global response is shown in Figure 5.2 (d). All the cases analyzed were plotted with three loads acting together (V_x, V_y and V_z).

Curvature is responsible for forming the arc. If this parameter was zero the parameterization would be a straight line. Therefore, if the arc radius increases, with a fixed length

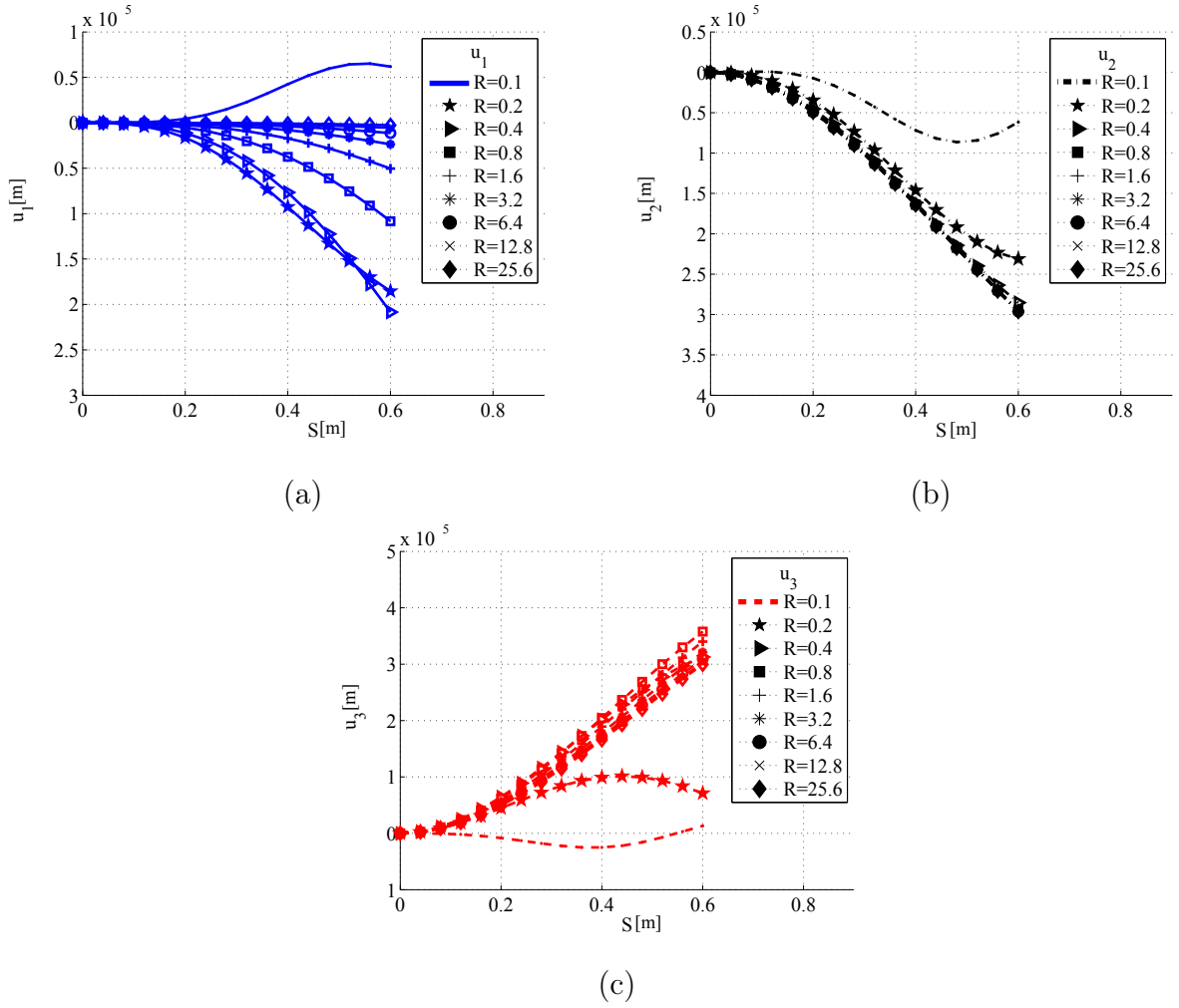

Figure 5.5 – Arc radius growth considering local displacement (a) u_1, (b) u_2 and (c) u_3.

($S_{max} = 0.628316\ m$), the problem tends to be a straight beam. Considering the same case analyzed previously, the term R, initially calculated as $0.1\ m$, was multiplied by two in every new analysis. Thus, local effects were analyzed.

Figure 5.3 (a) demonstrates the evolution of force element N_1 as the arc radius grows, from the results obtained previously to a constant value equal to the applied load. The component N_2 is represented in Figure 5.3 (b). A similar behavior is observed in which the component tends to a constant value. Figure 5.3 (c) represents N_3 that was already constant since the binormal vector is always aligned to V_z.

The same behavior is found for the moments (Figure 5.4). Locally, for the arc case M_1 has the highest value at the middle, as the radius grows the component decreases to zero. This happens because the load becomes aligned to the tangent vector. M_2 and M_3

(Figures 5.4 (b) and (c)) have similar behaviors from the arc result to the linear response once it trends to a straight beam.

Displacement u_1 is plotted in Figure 5.5 (a) which, once the load is aligned to the tangent vector due to the radius growth, decreases to a small value, however different than zero since its a tensile load in the straight configuration.

Figure 5.5 (b) and (c) presents the components u_2 and u_3, respectively. The final analyzed radius is $R = 22.6\ m$ (for every analysis) which, for the defined S_{max} configures, approximately, a straight line.

Another configuration achieved by this parameterization is the aforementioned helix. Cases considering α different than zero are analyzed in the next section.

5.3.2 The Helix Case

The geometry of an helix, obtained with the parametrization in Equations (2.16), (2.17) and (2.18), was analyzed. The constants are determined for the same condition and the geometric parameters detailed in Table 5.3. The material are the same as the arc in Table 5.2.

Table 5.3 – Helix geometry parameters.

α [°]	$\kappa[m^{-1}]$	τ $[m^{-1}]$	S_{max} $[m]$
0.654498	-6.29409	4.82963	0.791978

The FS basis is represented as

$$T_{helix} = \begin{bmatrix} -D\,\text{sen}\,(10DS) & D\cos(10DS) & G \\ \cos(10DS) & \text{sen}\,(10DS) & 0 \\ -G\,\text{sen}\,(10DS) & G\cos(10DS) & -D \end{bmatrix}, \tag{5.22}$$

where $D = 0.793353$ and $G = 0.608761$.

With this result, the expressions can be studied in the global or local system, since this matrix allows the transformation of any variable to both systems (global to local and

vice-versa). Multiplying Equation (5.22) and, once again, the concentrated forces in Equation (5.1) the local forces are written in the local form as

$$F_{helix} = \begin{bmatrix} -D\,\text{sen}\,(10DS)\,V_x + D\cos(10DS)\,V_y + GV_z \\ \cos(10DS)\,V_x + \text{sen}\,(10DS)\,V_y \\ -G\,\text{sen}\,(10DS)\,V_x + G\cos(10DS)\,V_y - DV_z \end{bmatrix} \tag{5.23}$$

Because of the parametrization, the local force acting on the normal direction ($\boldsymbol{n}$) has no influence of V_z. In view of the helix angle the triad is never aligned to the global system, hence this component is present in two directions (as expected, there is an influence in x_3, however, here, the decomposition produces an effect in x_1 as well). Nevertheless, ($\boldsymbol{n}$) is always parallel to the x_1x_2 plane, which is orthogonal to the applied load, thus no reaction is generated.

Assuming, initially, only concentrated loads on the free end, the terms q_1, q_2, q_3, m_1, m_2 and m_3 are equal to zero. In each case analyzed the loads are defined as Figure 5.6, where V_x is applied aligned to x_1, V_y to x_2, V_z to x_3 and all loads together. So all the constants are determined as,

$$\begin{aligned} C_1 &= -6.29409\ V_x, \\ C_2 &= -6.29409\ V_y, \\ C_3 &= \quad 0.608761\ V_z, \\ C_4 &= -0.482962\ V_x + 3.03454\ V_y, \\ C_5 &= -3.03454\ V_x + 0.629409\ V_z, \\ C_6 &= \quad 0.0608761\ V_y, +0.793353\ V_z. \end{aligned} \tag{5.24}$$

Consequently, Equations (4.25), (4.26) and (4.27) are fully defined as a function of S only. The forces in the local coordinates are:

$$N_{helix} = \begin{bmatrix} -D\,\text{sen}\ (10DS)\ V_x + D\cos(10DS)\,V_y + G\ V_z \\ \cos(10DS)\,V_x + \text{sen}\ (10DS)\,V_y \\ -G\,\text{sen}\ (10DS)\,V_x + G\cos(10DS)\,V_y - DV_z \end{bmatrix}. \tag{5.25}$$

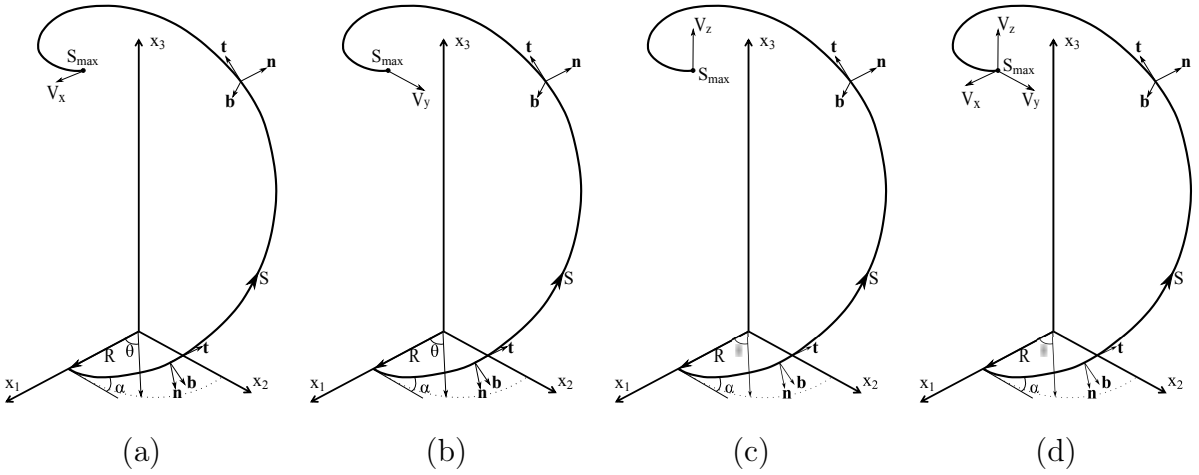

(a) (b) (c) (d)

Figure 5.6 – Concentrated loads applied in the helix considering (a) V_x aligned to x_1, (b) V_y to x_2, (c) V_z to x_3 and (d) all components simultaneously

And the moments (Equations (4.29), (4.30) and (4.31) are written as

$$M_{helix} = \begin{bmatrix} M_{1helix} \\ M_{2helix} \\ M_{3helix} \end{bmatrix}, \tag{5.26}$$

where

$$\begin{aligned} M_{1helix} = {} & 0.1GV_y + 0.1DV_z - 0.1DV_z\cos(10DS) + H\,\text{sen}\ (10DS)\,V_y + \\ & + H\cos(10DS)\,V_x - WSV_x\cos(10DS) - WSV_y\,\text{sen}\ (10DS) + \\ & + 0.1G\,\text{sen}\ (10DS)\,V_x - 0.1G\cos(10DS)\,V_y \end{aligned} \tag{5.27}$$

$$\begin{aligned} M_{2helix} = &-GS\,\text{sen}\,(10DS)\,V_x + G\cos(10DS)\,SV_y - 0.1\,\text{sen}\,(10DS)\,V_z + \\ &+ W\,\text{sen}\,(10DS)\,V_x - W\cos(10DS)\,V_y - 0.1DV_y + 0.1GV_z + \\ &+ L\cos(10DS)\,V_x - KSV_x\cos(10DS) \end{aligned} \tag{5.28}$$

$$\begin{aligned} M_{3helix} = &-0.1GV_z\cos(10DS) - 0.1D\,\text{sen}\,(10DS)\,V_x + 0.1D\cos(10DS)\,V_y + \\ &+ L\,\text{sen}\,(10DS)\,V_y - KSV_y\,\text{sen}\,(10DS) \end{aligned} \tag{5.29}$$

and $H = 0.382496$, $W = 0.482962$, $K = 0.370590$ and $L = 0.293499$. Hence, the forces can be graphically expressed as in Figure 5.7, where four cases are analyzed. The first case, Figure 5.7 (a), is a force aligned to x_1, the second (Figure 5.7 (b)),has a load V_y parallel to x_2, V_z is applied in the x_3 direction in Figure 5.7 (c) and the last case (Figure 5.7 (d)) represents the response when all three unitary loads are present. These four cases are repeated through this section.

Analyzing the figures it is possible to notice the local force behavior acting on the helix. For the first case, Figure 5.7 (a), the load is set parallel to the vector $\boldsymbol{n}$ of the FS triad. This means that all the magnitude is accounted in the N_2 component, since the component is also parallel to it, at the point where the force is applied.

The other forces are zero at the beginning because they are orthogonal to the applied force. Along the local system this behavior changes, i.e., N_2 decrease until zero while the other components reach their maximum.

Since the triad is not coincident to the global system, once the force is orthogonal to the FS basis (at approximately $S = 0, 2m$) the parameter α is responsible to the decomposition of F_x into N_1 and N_3. Performing the vector sum of the components it gives the unit vector. In fact, for all the cases and at any point of the curvilinear coordinate (S), this operation returns the applied load magnitude.

The value change has a cosine function for N_2 and as sine considering N_1 because of the N_{helix} vector, Equation 5.25, caused by the application of only V_x. The alternation of signs is due to the change of orientation with the triad.

In the second case, Figure 5.7 (b), a unitary load is applied parallel to x_2. The same behavior is observed in this case where the load is decomposed in to N_1 and N_3 while

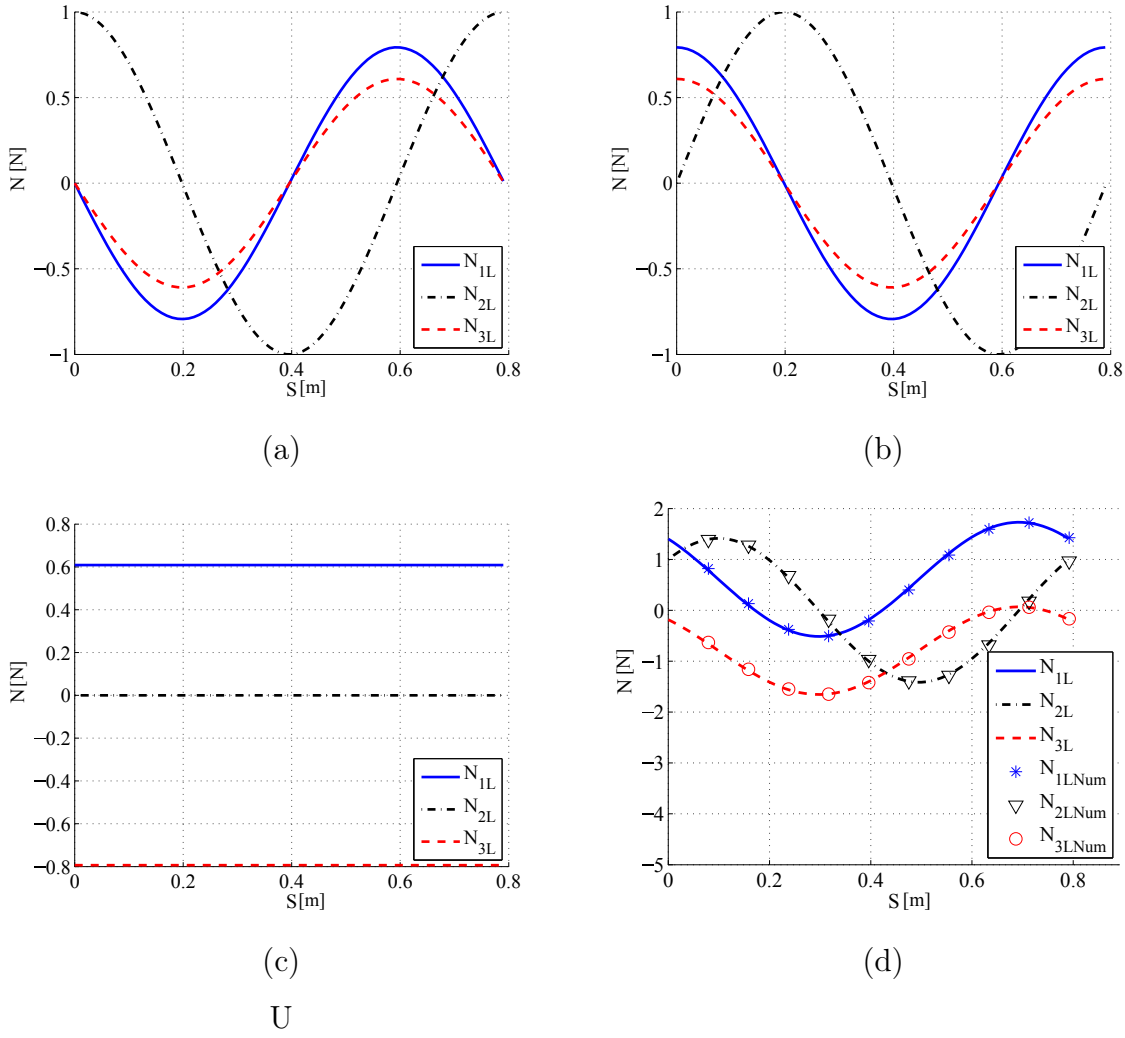

Figure 5.7 – Local forces for the helix case with unitary loads (a) V_x in the x_1 direction, (b) V_y aligned to V_2 axis, (c) V_z parallel to x_3 and (d) all loads applied

N_2 remains zero. Since the triad component $\mathbf{t}$ is positioned aligned to x_2 and the force is orthogonal to it there is no effect in this direction on N_2.

Once more, the maximum of N_2 occurs at the same position as the minimum for the other variables (in modulus). The opposite is also true, this alternation happens due to the local system analysis, which changes with the angle where the section is evaluated.

The third case is a simple case where only V_z is acting. The load is orthogonal to x_1x_2 plane, consequently, there is no decomposition that makes effect on N_2. Likewise, every position has the same outcome, generating a constant value of $N_1 = 0.6N$ and $N_3 = 0.8N$.

The final case, Figure 5.7 (d), is an assembly of the other three. This means that all

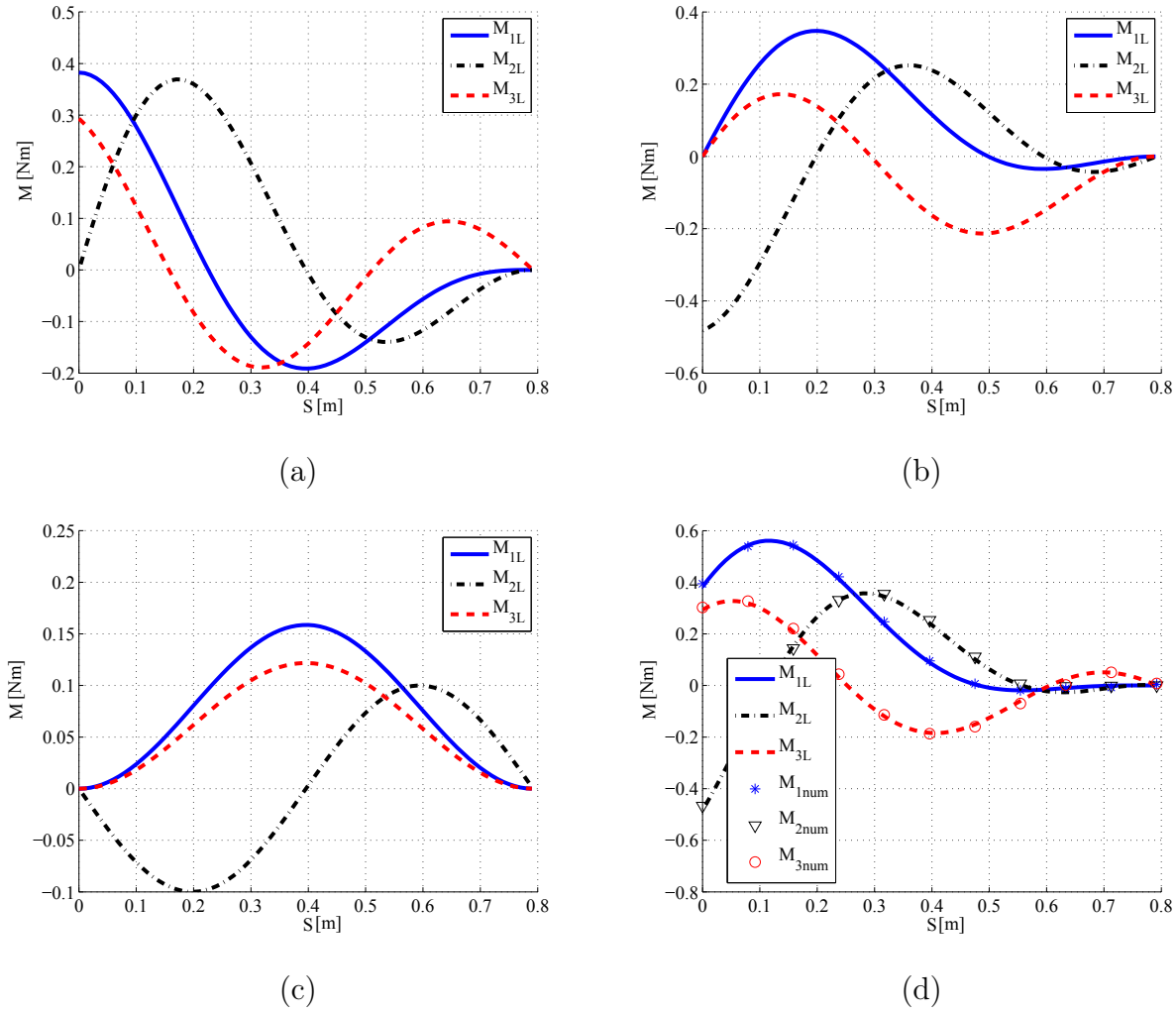

Figure 5.8 – Local moments considering unitary loads (a) V_x in the x_1 direction, (b) V_y aligned to V_2 axis, (c) V_z parallel to x_3 and (d) all loads applied.

the loads, analyzed separately, are now considered together and applied in the same direction as before, in other words the resultant is not aligned to any axis.

Initially (at $S = 0m$), no component is null since the resultant is not orthogonal to any vector of the FS basis. The superposition is also present in this analysis and can be verified in any position of S. Adding the three results obtained previously generates the same effect as applying the forces together, e. g., N_3 at the same beginning point is set as $N_3 = 0 + 0.6N + (-0.8N) = -0.2N$.

One can notice as well that the highest values (in modulus) does not occur at the same points as the previous examples ($S = 0.2m$, $S = 0.4m$, $S = 0.6m$ and $S = 0.8m$ or at

the quadrants), they are now translated to where the planes $\boldsymbol{t} \times \boldsymbol{b}$ and $\boldsymbol{n} \times \boldsymbol{b}$ are orthogonal to the resultant load.

Using the transformation matrix to change the local to the global system (multiplying N_{helix} for the inverse of $\mathbf{T}$), the reacting forces are now constants and equal to the load applied.

Once the forces are determined, the moments can be analyzed. Using the values from the local analysis and multiplying it by the respective lever arm it is possible to calculate each local component.

Again, the same four cases are studied. Figure 5.8 shows the moments for each situation. Initially, only V_x is considered (5.8 (a)) and, according to the local forces, only N_2 is not null. This value, multiplied by the distance between the point of analysis (position of the Frenet-Serret triad), gives the moment. That way, there are 2 components affected by N_2, M_1 and M_3, since the local system is inclined by the helix angle (α).

At the end of the first quadrant one can see the maximum value for M_2, that increased from the clamped end. The top values take place, for the moments, always when the FS is orthogonal to the applied load. The other two components decrease and are equal to zero in different points. For M_1, it occurs in the second quadrant, as the tangent vector is inclined and its axis becomes aligned to the load. As the local system approximate to the position of the applied force all values of moments decline until zero, considering that there is no distance to generate moment.

The second case (V_y applied) has the same behavior of the last case for the same reasons (Figure 5.8 (b)). Starting at the clamped end, the load is contained in the $\boldsymbol{t} \times \boldsymbol{b}$ plane, therefore, it does not produce any effect on these components. The only moment present is M_2, which has the highest value, since the distance is the largest.

At the end of the first quadrant, M_2 decreases to zero, while M_1 reaches its maximum. M_3 grows until the distance between the applied force and the component $\boldsymbol{b}$, which falls down because of the new alignment of the entities (at $S = 0.3$). The correspondent value of this variable for $S = 0.5$ is higher since the projection of $\boldsymbol{b}$ is now pointed in the opposite direction.

If only an upwards force is applied (Figure 5.8 (c)), or V_z, the decomposition into the local system is never aligned to $\boldsymbol{n}$, and although, no force component is generated, the

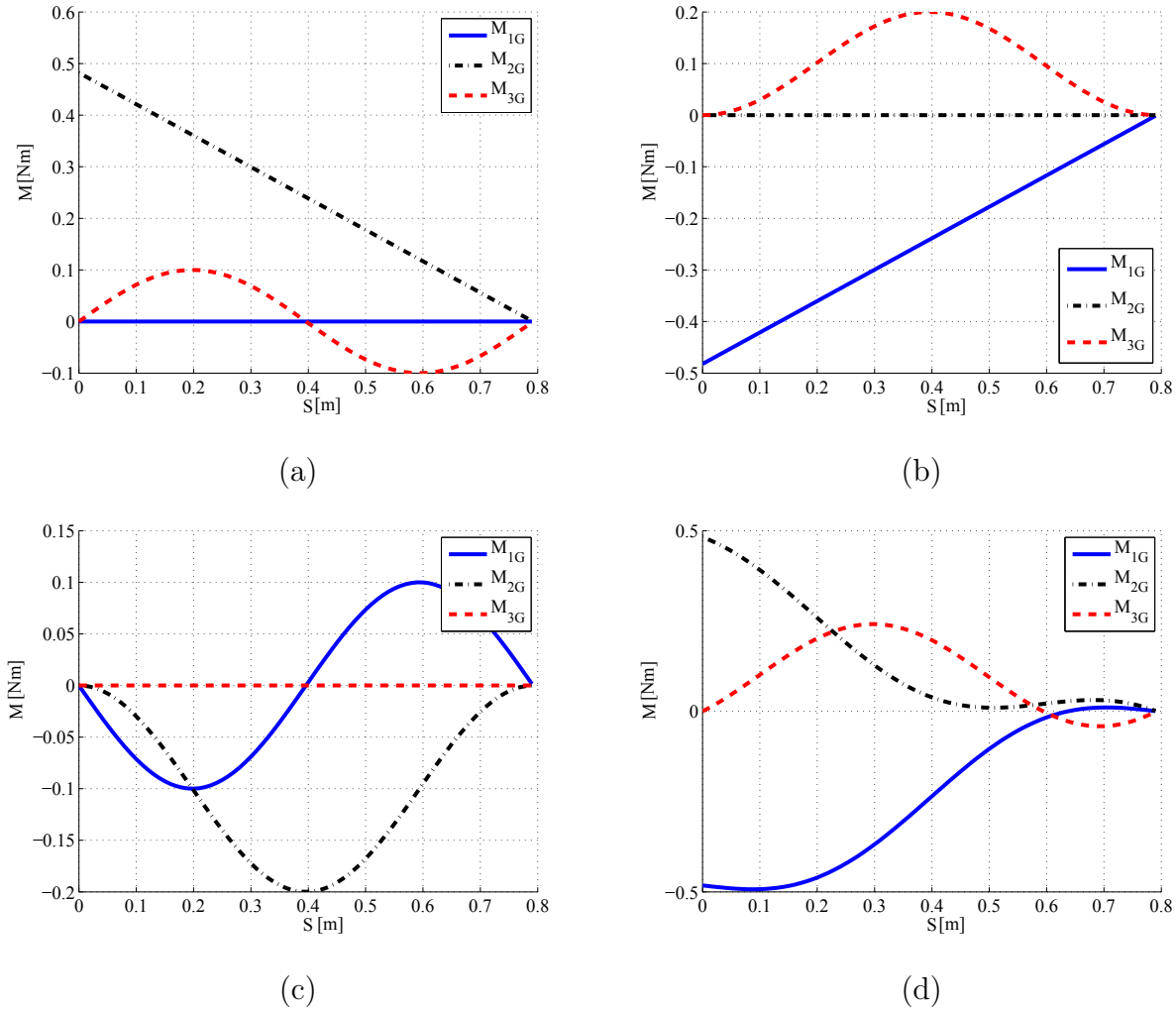

Figure 5.9 – Global moments for the helix case (a) V_x applied aligned to x_1, (b) V_y to x_2, (c) V_z parallel to x_3 and (d) all loads applied.

FS becomes orthogonal to the component and M_2 oscillates as a negative sine (as seen in M_{helix}). The other moments reach their maximum when the distance is equal to two times the radius, since the inclination of the triad does not affect the length used to calculate the moments.

For the last case, where three forces are applied together, Figure 5.8 (d), there is a resultant not contained in or orthogonal to any plane formed in the local or global system. The resultant is, again, a sum of the three cases, as expected. Therefore, either using the superposition or the loads simultaneously applied results in the same outcome.

Since the moments on the third case are significantly smaller than the other two

cases, the effect of the respective loading is barely noticed.

Moments are globally represented in Figure 5.9. The linearity of M_2, in the first case (V_x applied), is due to the constant change in the height and M_3 grows to the maximum and decreases to zero, since the applied force is initially parallel, becomes orthogonal ($S = 0.2$ and $S = 0.6$) and in the end is, again, aligned. The other component is null because in the decomposition the resultant is always orthogonal.

Figure 5.9 (b) represents the global response when the load V_y is applied. An analogous behavior, from the last case analyzed, was expected. The linearity is present as M_1 decreases, in modulus, to zero. The second component is always zero, since it is perpendicular to the force, and M_3 increases from zero to the maximum value (at the end of second quadrant) and back to zero where the force is present.

The last case with only one force, Figure 5.9 (c), showed a moment distribution just in M_1 and M_2. This means that V_z is aligned to the binormal vector. The components change their value according to the distance between the section in analysis and the load position.

With the full set of loads, where all forces are considered together, the global moments have no null component (Figure 5.9 (d)). In this case the resultant is inclined and the projection passes through $S = 0.6m$, consequently this is the only point where any component can have zero value.

The application of more than one load, parallel to an axis, generates a resultant not aligned to the global system. As a consequence, the positions where the largest distances occur change, generating the highest moments elsewhere, and the point of alignment to the global axes.

The cases analyzed were produced by the geometry in Table 5.3. Nonetheless, although the results of each parameter change for other physical sets, the properties of the local system are similar. The loads were also used as unitary because of two reasons: the system is linear and any change in the force affects proportionally all the results.

In order to analyze stresses and strains in the helix, the expressions obtained in Equations (4.32), (4.33),(4.34), (4.35), (4.36) and (4.37) are now written with the geometry in Table 5.3.

With the strains calculated, the second system of differential equations were used

to solve rotations and displacements (Equations 4.38, 4.39, 4.40 and 4.43, respectively). Six more constants were determined from the boundary conditions. The clamped end implies that rotation and displacements are set to be zero.

Local rotations were determined and are shown in Figure 5.10. Analyzing the first case, Figure 5.10 (a), with only one load parallel to x_1 it is possible to notice the similar behavior of ϕ_1 and ϕ_3 because of the local decomposition. After the first quadrant and the third quadrant ϕ_2 reaches two peaks, when the applied force is aligned to the normal vector.

The other two rotations are zero at the same positions, where the load is orthogonal to the rectifying plane. The similar behavior of u_1 and u_3 happens because both are orthogonal to the loading, which means that they are always affected analogously.

In the second case another bending moment produced was applied , however aligned to x_2 (Figure 5.10 (b)). Again, ϕ_1 and ϕ_3 had resembling properties. In fact, due to the decomposition of the loads into the triad, locally, there is always a component affecting both $\boldsymbol{t}$ and $\boldsymbol{b}$. Similar behaviors, though inverted, can be seen in Figure 5.10 (b) where, at $(S = 0.2\ m)$ and $(S = 0.6\ m)$, ϕ_2 is zero and other components show an inflection point.

Figure 5.10 (c) presents V_z as loading. The greatest values for ϕ_1 and ϕ_3 happen in $S = 0.4\ m$ and at the free end since the load is orthogonal to x_1x_2 plane.

When the full load case is considered, Figure 5.10 (d), the positions where the peaks and zero occur change due to the resultant. The reasons are, likewise, the same as in other conditions. The higher the distance between the point of analysis and the load, the greatest is its value. The tensile case (third analysis) is the one that least contributes to the final rotation value, i.e., the cable has small rotations with this kind of load which is the most common in practice. Showing that the structure has its major resistance aligned to x_3 direction.

With the results of local rotations obtained previously, the global effects were determined. Applying the methodology described in section 2.4, using the transformation matrix, the results were plotted in Figure 5.11.

Globally, the load aligned to x_1 produced a small and negative rotation on ϕ_1. The effect in the third component is also small for the same reason. Nevertheless, ϕ_2, due to the bending, increases until the maximum value at the free end $(S = 0.8\ m)$.

Again, even considering only the load V_y (Figure 5.11 (b)), one component increases,

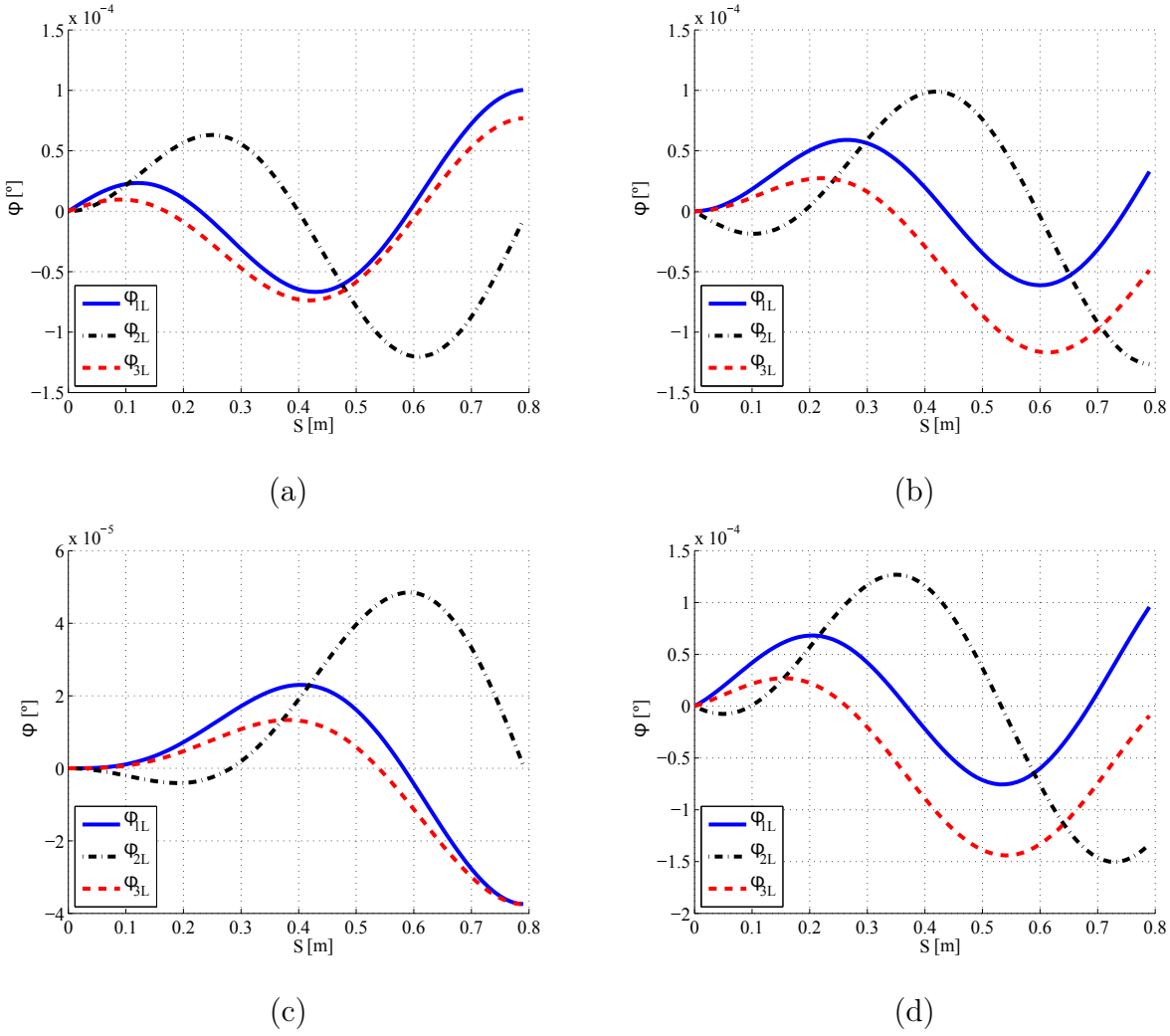

Figure 5.10 – Local rotations generated by unitary loads applied with (a) V_x aligned to x_1, (b) V_y to x_2 axis, (c) V_z to x_3 and (d) all loads applied.

to a similar value as the last case, until its maximum value (ϕ_2). Once more, the bending produced this effect. Although one component is still close to zero, ϕ_3 has a different behavior and grows along the coordinate (S).

A tensile load, in the third case (Figure 5.11 (c)), makes the torsion in the x_2 direction increase, due to the tendency to reduce the helix radius. The component ϕ_1 reaches its maximum in the middle of the S coordinate, due to the distance from the load applications to the clamped end.

When all the loads are considered together, Figure 5.11 (d), the resultant changes its alignment with the axes, so that the quadrants end are no longer a reference point.

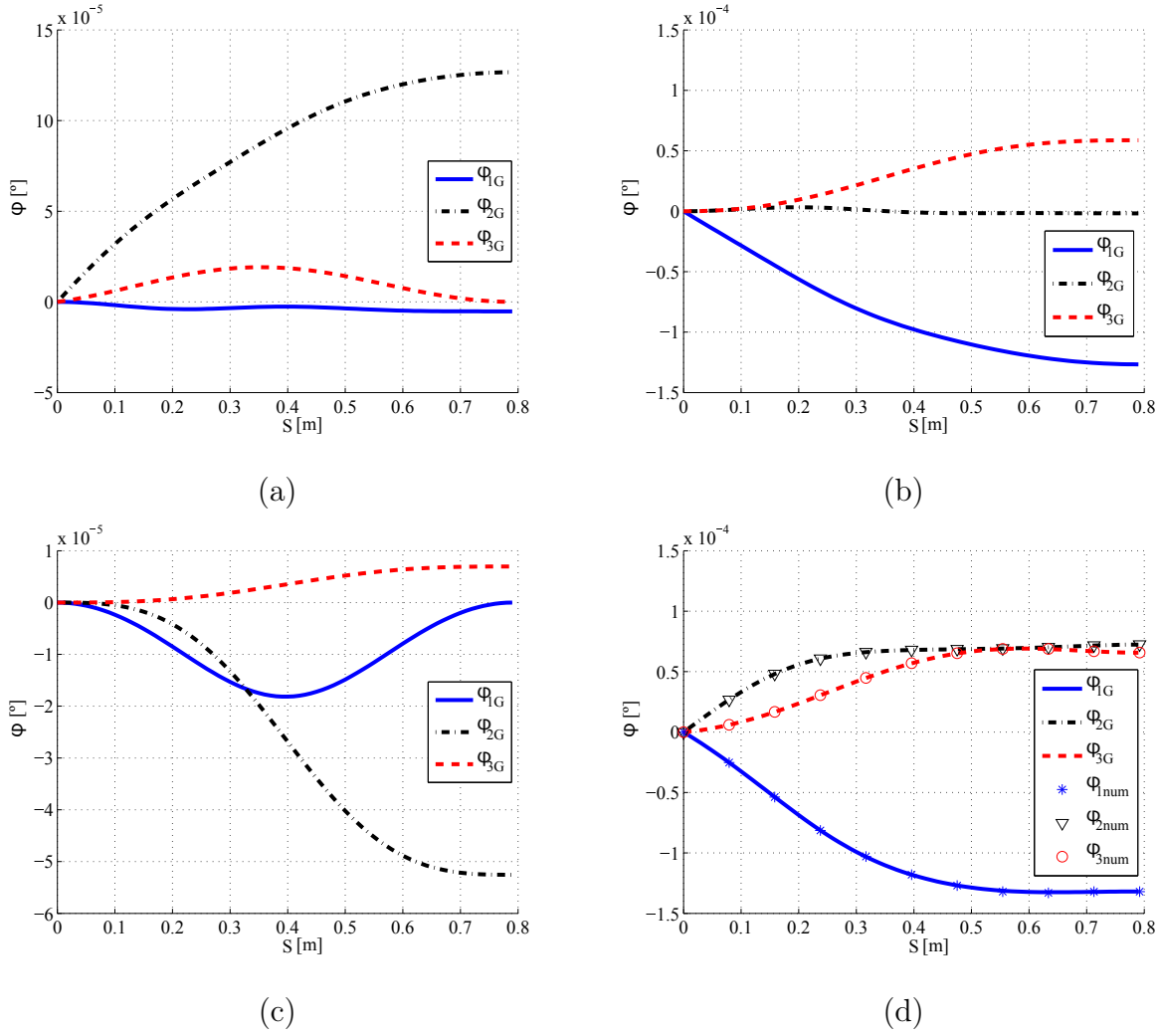

Figure 5.11 – Global rotations determined from a load (a) V_x pointed in the x_1 direction, (b) aligned to x_2, (c) aligned to x_3 and (d) with all the loads applied together.

The components behavior were similar to the second case. Analyzing first ϕ_1, the torsion produced by the decomposition of the force in $\boldsymbol{t}$ is approximately the opposite of the result from the component acting in $\boldsymbol{b}$. Actually, this happens for all rotations.

To generate the last case three, loads are accounted for. No rotation component is null or close to zero. The maximum value was presented by ϕ_1, at the load application, since the bending ant the tension contribute to it. The other variables demonstrated a similar behavior.

Using the methodology demonstrated in Section 4.2 to calculate the displacements, the three last constants of integration must be determined. This implies the application of

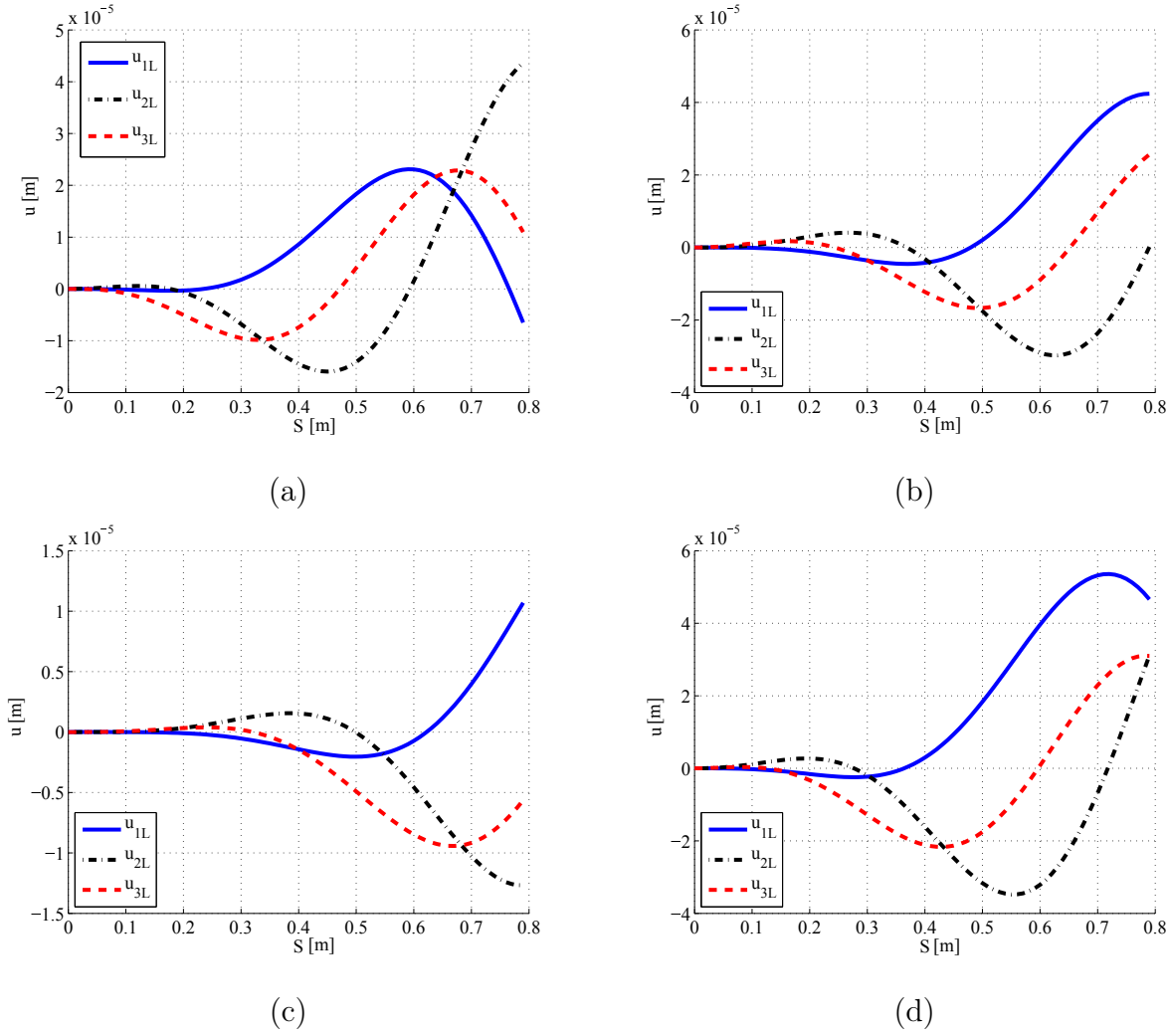

Figure 5.12 – Local displacements for the helix case with unitary loads (a) V_x in the x_1 direction, (b) V_y aligned to V_2 axis, (c) V_z parallel to x_3 and (d) all loads applied

the boundary conditions, still considering a clamped-free case.

Rotations influence directly on the calculation of the displacements, since the effects are coupled. Thus, the components u_1, u_2 and u_3 were determined with the methodology of Equation 4.42. The last three integration constants were determined by the imposition of the aforementioned BC.

Local results are presented in Figure 5.12. The cases presented the same methodology as the other analysis. Starting with the load parallel to x_1 the local displacement are zero, as explained before, at $S = 0$ (Figure 5.12 (a)). The component u_2 presented the highest value, at the free end, since the bending is in this direction. The other compo-

nents reach their maximum close to the end of the third quadrant due to the distance and orthogonality of the load.

In the second case,Figure 5.12 (b), with a load aligned to x_2, the bending occurs in the other direction, compared to the first case, thus the highest value of u_1.

Tensile load applied produced the graphic in Figure 5.12 (c), where the first and second displacements components present, in modulus, the higher values. This is due the curvature and the helix angle, i.e., the load tends to straighten the strand, consequently u_1 and u_2 are the most affected.

With all the loads together, Figure 5.12 (d), the local displacements presented results close to the first two cases, since the third case had values smaller than the others.

To analyze the effects on the displacements produced by the concentrated loads applied to the strand in global coordinates, the transformation must be performed again. The application of a load perpendicular to x_3 and x_2 produce displacements on the first component that increases as the coordinate S develops until the highest value, Figure 5.13 (a). Although never negative, it grows approximately linearly after the middle of the strand, due to the curvature. Along S, the second component remains close to zero. Because of the decomposition of loads, no effect is generated in $\boldsymbol{n}$, so all the calculated displacement is caused by the bending.

With the load aligned to x_2, Figure 5.13 (b), the second component becomes the greatest value at the free end. The other components presented similar behaviors to the first case since the force orientation change did not produce any significantly effect.

For the third case, Figure 5.13 (c), once again the load produced effects in all the components. The highest values were produced at the free end for all the cases, differently than the previous two cases. Even though there is no component meaningfully larger, adding the effects produce a smaller value when compared to the other cases. This result is significant and coherent, since it is considered the study of a cable, and the low displacement of this case shows the expected result for such structure.

Regarding the alignment of the load with x_3, one could expect the largest displacement value (in modulus) from u_3. However the decomposition of the load together with the flexure caused by the geometry contributes to the maximum value of u_1.

The last case, Figure 5.13 (d), shows the initial positive slope of all the components.

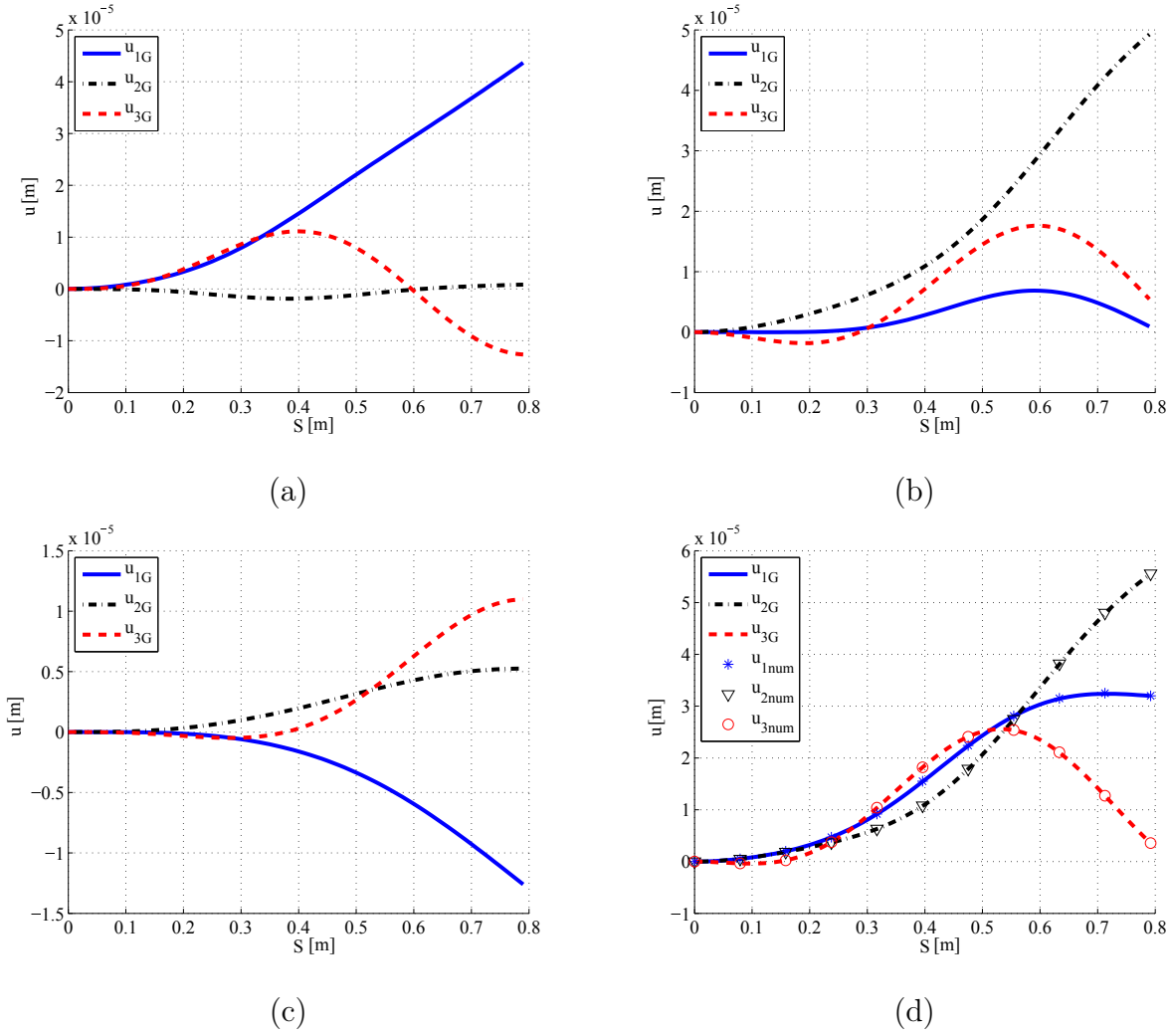

Figure 5.13 – Global displacements of the helix considering (a) V_x aligned to x_1, (b) V_y parallel to x_2, (c) V_z in x_3 direction and (d) all components applied together.

While u_2 reaches the maximum value at the free end u_3 decreases, after the peak, due to the bending in the other directions.

Four cases were analyzed in this sections. Graphics for forces, moments, rotations and displacements were generated and studied. Numerical results were obtained with FEM, presenting good agreement in the local system for forces and moments and globally for rotations and displacements, with the analytical ones.

The theory of spatial beams proved to be efficient to analyze a single strand. The results obtained can be used for the other five similar helix structures that compose the cable analyzed here.

5.4 Distributed Loads

Forces and moments were obtained using, again, the geometry in Table 5.3 for distributed loads. The same appoach was considered, where Equations (4.25), (4.26), (4.27), (4.29), (4.30) and (4.31) were set as the reaction produced by the clamped condition at $S = 0$.

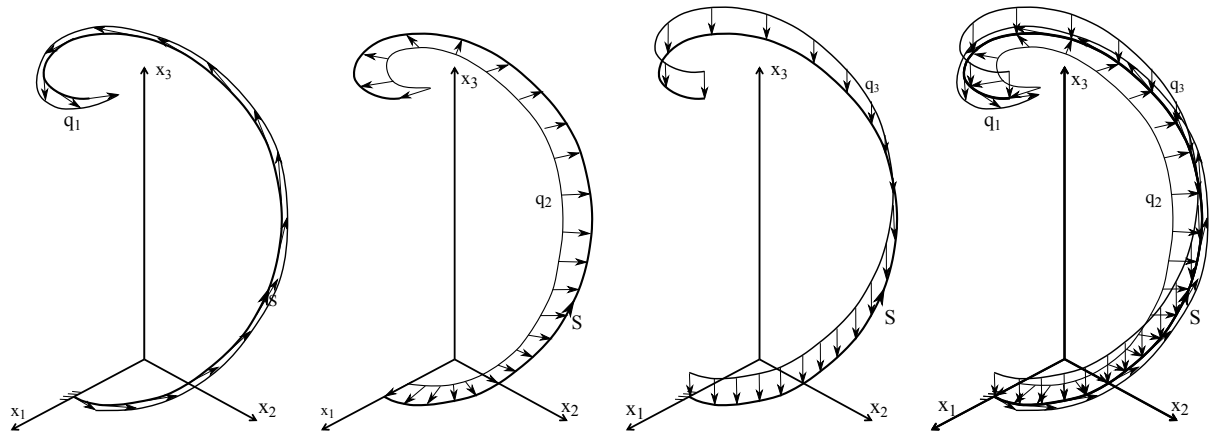

(a) (b) (c) (d)

Figure 5.14 – Distributed loads applied in the helix considering (a) q_1 aligned to $\boldsymbol{t}$, (b) q_2 to $\boldsymbol{n}$, (c) q_3 to $\boldsymbol{b}$ and (d) all components simultaneously

Unitary loads were applied in the local system to simplify the analysis, as shown in Figure 5.14. Constant distributed load was used. Consequently, the boundary condition integrated to account for all its effects. The result was used to calculate the first three constants.

Figure 5.15 presents the force results for the four cases mentioned before. Initially, only a load aligned to the tangent vector is considered (Figure 5.15 (a)).

A normal load is applied in the second case, Figure 5.15 (b). It is interesting to notice that there is no reaction on the clamped end. Since the load is equally distributed radially, the equilibrium is verified without the BC. At $S = 0.2\ m$ N_2 reaches its maximum, since a quarter of the helix is set and the integral of the load account only for the effect in one direction. As one moves along the curve this component decreases and at ($S = 0.4$) half the strand is considered, therefore, there are components in two opposite directions which cancel each other.

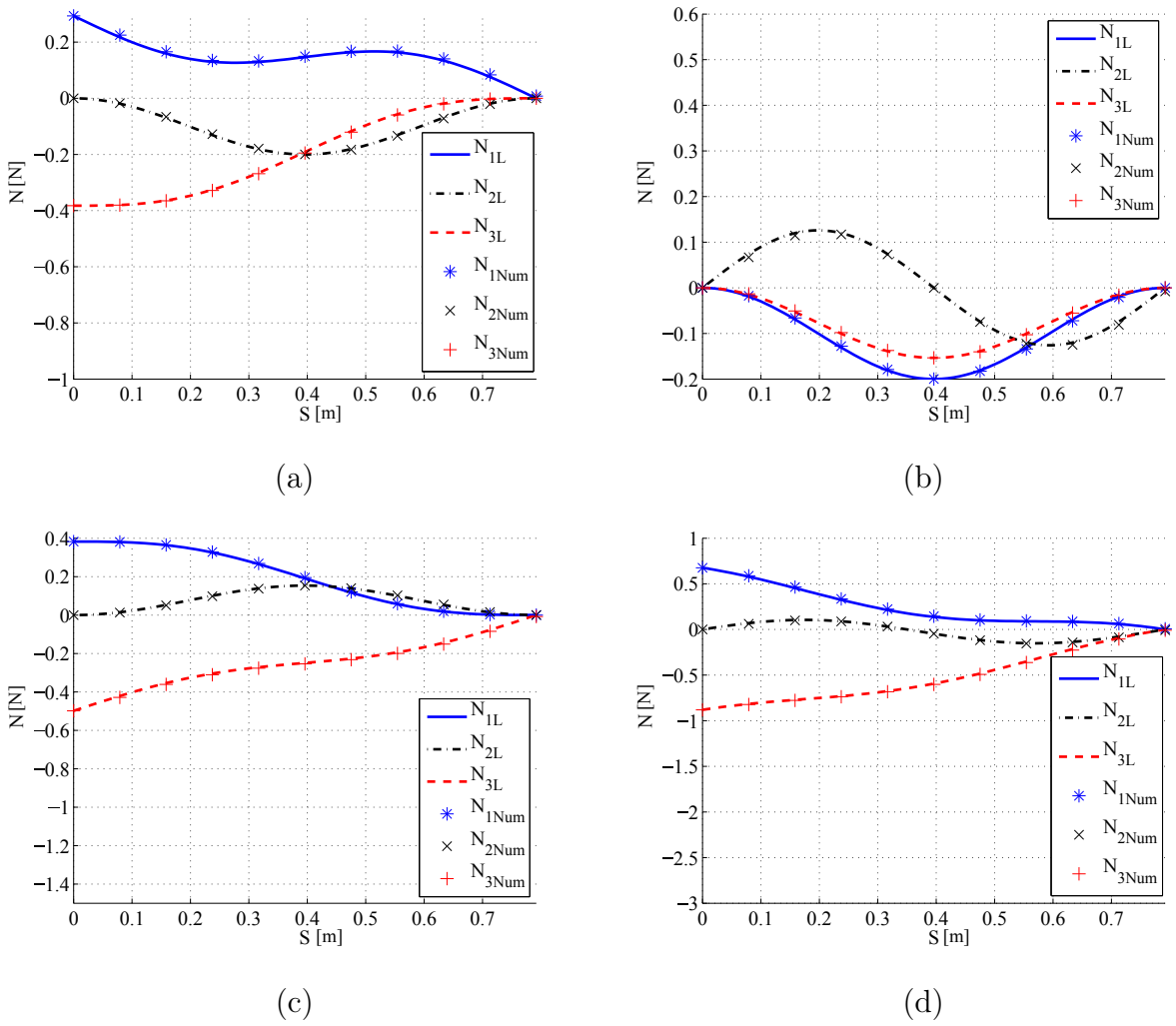

Figure 5.15 – Local forces of the helix considering (a) q_1 aligned to $\boldsymbol{t}$, (b) q_2 to $\boldsymbol{n}$, (c) q_3 to $\boldsymbol{b}$ and (d) all components applied together

Analogously, for N_1 and N_3 their maximum occurs at the middle of the wire and as the position S develops, the components change direction and, when considered the full structure, its effect is consequently annulled.

A load distributed in the binormal direction is represented in Figure 5.15 (c) where, at the clamped end, the integrated load is decomposed. N_2 demonstrate a similar behavior from the last case, where when the effect from the whole strand is considered, its modulus is zero. The other components decrease, in modulus, as the position of analysis approximate to the free end.

Once all the distributed loads are considered together (Figure 5.15 (c)) the superpo-

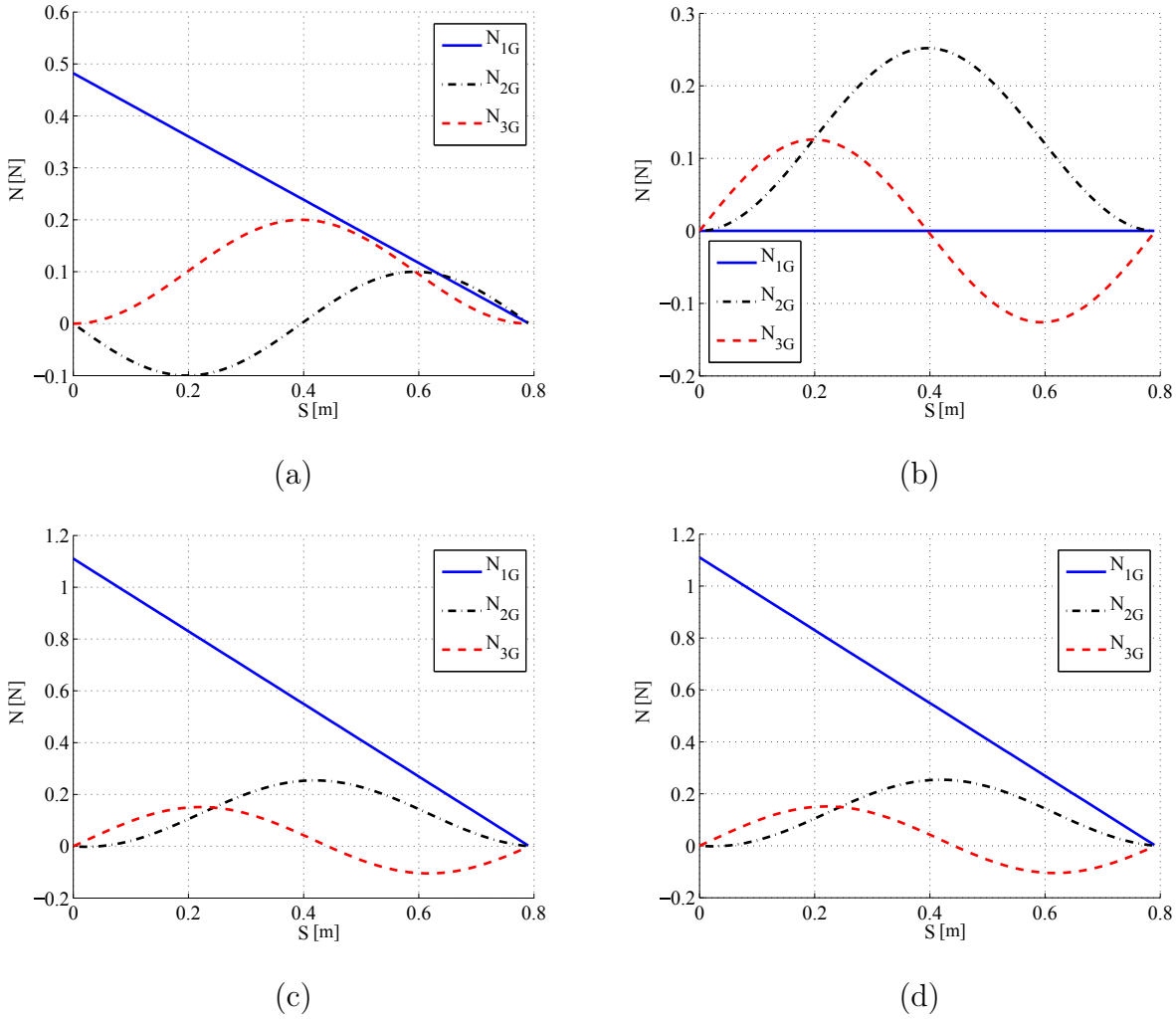

Figure 5.16 – Global forces of the helix with (a) q_1 aligned to $\boldsymbol{t}$, (b) q_2 to $\boldsymbol{n}$, (c) q_3 to $\boldsymbol{b}$ and (d) all components applied together

sition is, once again, verified. The normal vector is the only entity that, when considered the complete effect of the load (or one turn), is null and presents no value at the BC application. The other components have defined reactions due to the helix angle.

The global effects of the distributed load are shown in Figure 5.16. The components N_1 and N_2 do not present any reaction component at the clamped end. In fact, the only value different than zero occurs for N_3. Globally, the first and third cases are similar (Figures 5.16 (a) and (c), respectively), since the tangent and normal vectors are orthogonal, and considering the helix angle, the decomposition in the x_1x_2 plane are in opposite directions with different modulus.

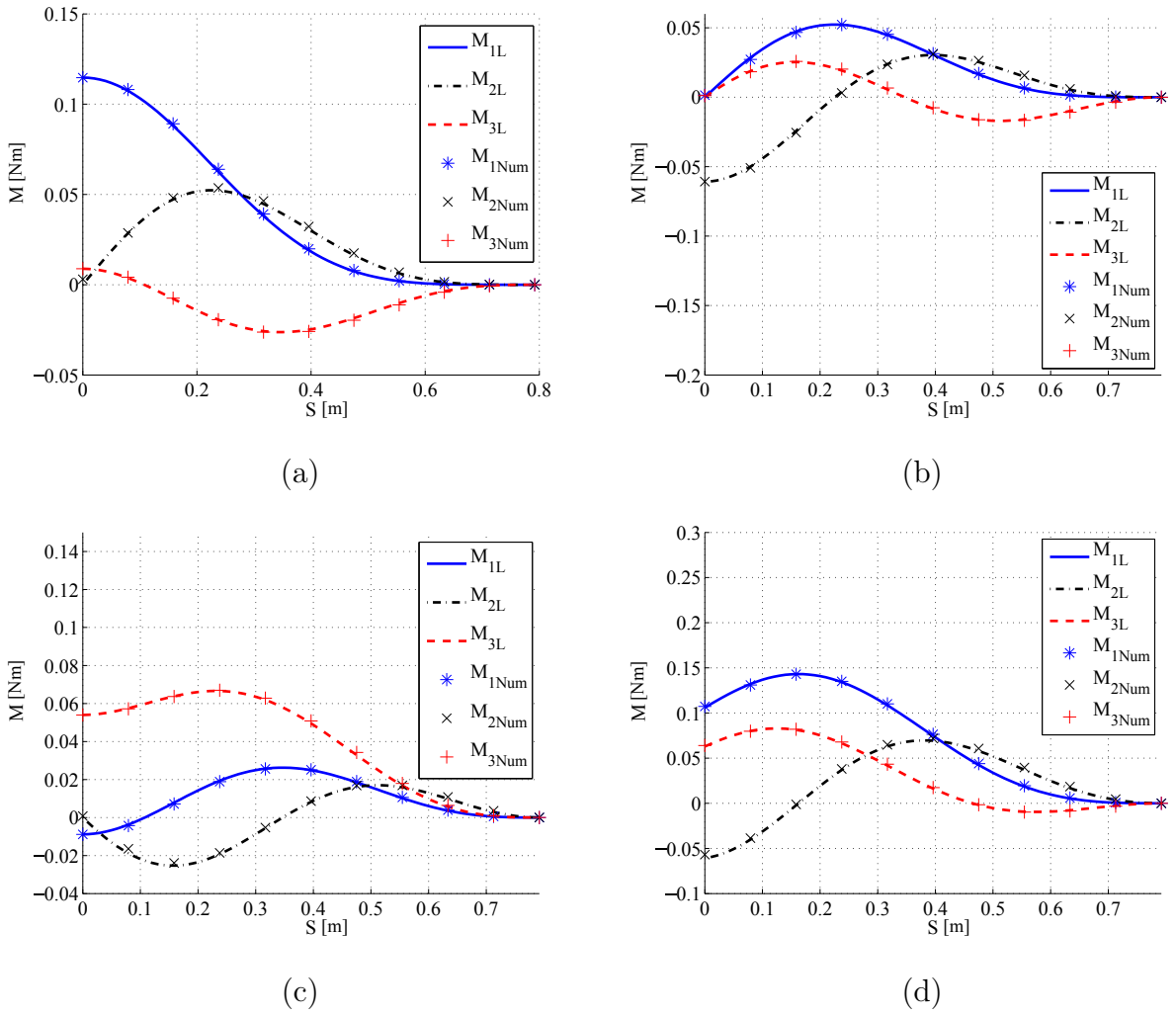

Figure 5.17 – Local moments of the helix considering (a) q_1 aligned to $\boldsymbol{t}$, (b) q_2 to $\boldsymbol{n}$, (c) q_3 to $\boldsymbol{b}$ and (d) all components applied together

When all three loads are applied together, the behavior of N_1 and N_2 are determined mostly by the normal force (Figure 5.16 (b)), which does not influence N_3, since it is orthogonal to it. A uniformly distributed load was applied, consequently the global effect on N_3 increases linearly from the point of application of the force (free end) until the clamped end.

Moments were also determined by multiplying the applied loads by the position vector and then performing the defined integral from zero to S_{max} the boundary condition can be defined. Figure 5.17 presents the local moments components.

The second case is the load distributed aligned to $\boldsymbol{n}$. Although no force was genera-

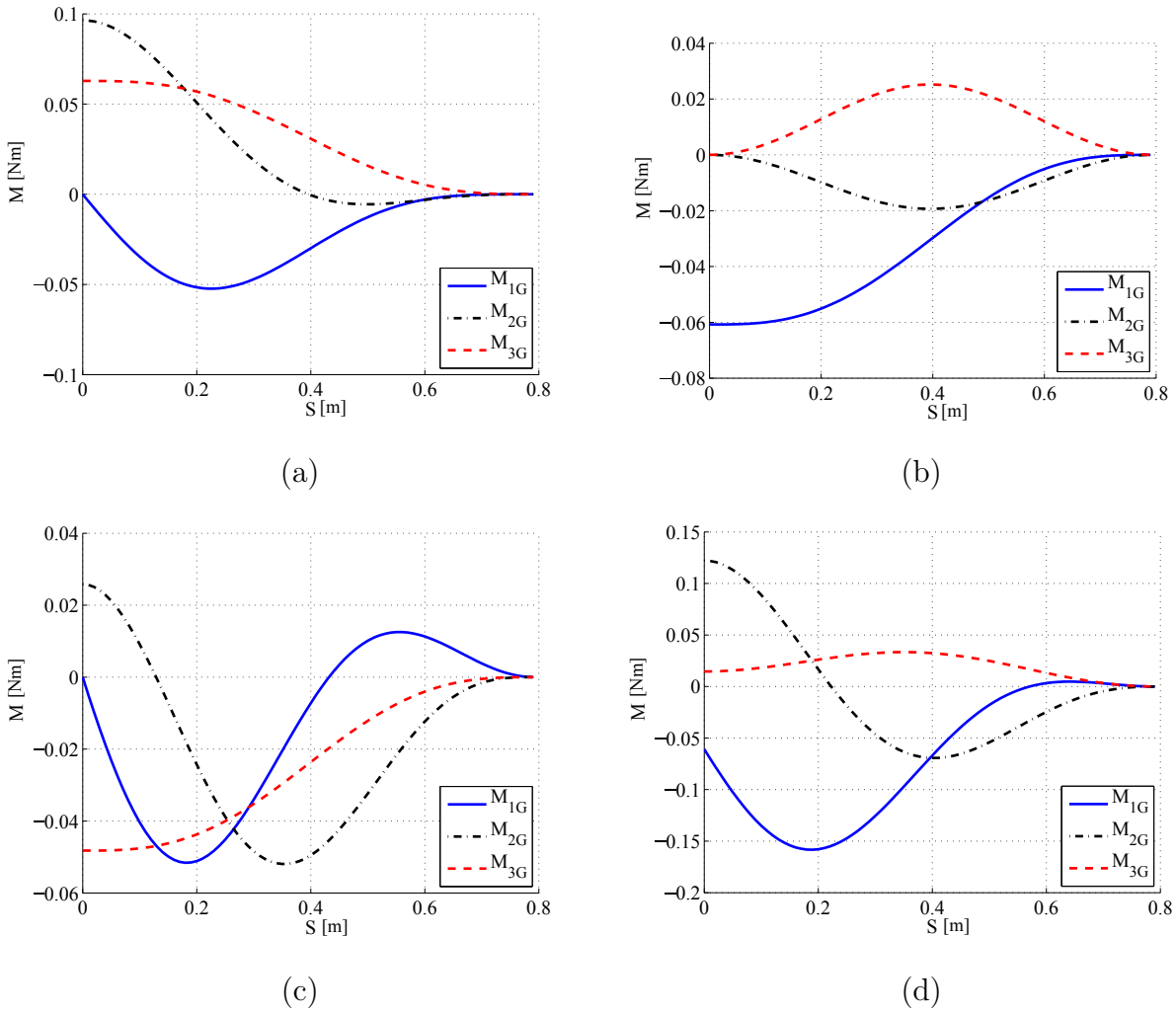

Figure 5.18 – Global moments considering (a) q_1 aligned to $\boldsymbol{t}$, (b) q_2 to $\boldsymbol{n}$, (c) q_3 to $\boldsymbol{b}$ and (d) all loads simultaneously

ted in the clamped end, there is a moment at $S = 0$. The distance considered to determine M_1 and M_2 is the component parallel to x_3 , therefore, they represent the higher values while M_3 depends on the radius.

5.5 Spring Modeling

Springs are an important class of structures that can be modeled with the proposed methodology. In order to simulate one of such cases, two more turns were added to the geometry analyzed before. The same procedure was adopted and initially the boundary conditions were used to define the constants.

One unitary load was applied in the helix main axis, that is, aligned to x_3 in the global system. As a consequence of this eccentricity a moment must be considered in the other end to respect the equilibrium. So, the final configuration is the one presented in Figure 5.19 with the center line indicated by the dotted line.

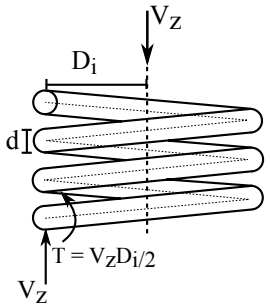

Figure 5.19 – Spring analyzed with a force applied in the center.

Only a moment in the second component was accounted for multiplying the radius R by the force. Once again, the effects were brought to the local system and the solution is represented in Figure 5.20.

Locally, both forces (Figure 5.20 (a)) and moments (Figure 5.20 (c)) diagrams are constants, the first presents the same decomposition as analyzed in Figure 5.7 (c) case. Analogously, the moments are invariant since the distance from the load, which is decomposed in $\boldsymbol{t}$ and $\boldsymbol{b}$, does not change.

Figure 5.20 (d) shows the global moment development. Although the behavior is similar to other cases, its final value (at $S = 2.4\ m$) is different than zero due to the concentrated moment applied.

Strains and stresses were determined using the theory proposed by Shigley et al., 2004. Maximum shearing was also calculated as:

$$\sigma_{sh} = \xi \frac{8 V_z D_i}{\pi d^3}, \tag{5.30}$$

where V_z is the applied load, D_i the internal diameter of the spring ($D_i = 2R$) and d the diameter of the wire ($d = 2r$). The parameter ξ is a curvature adjustment:

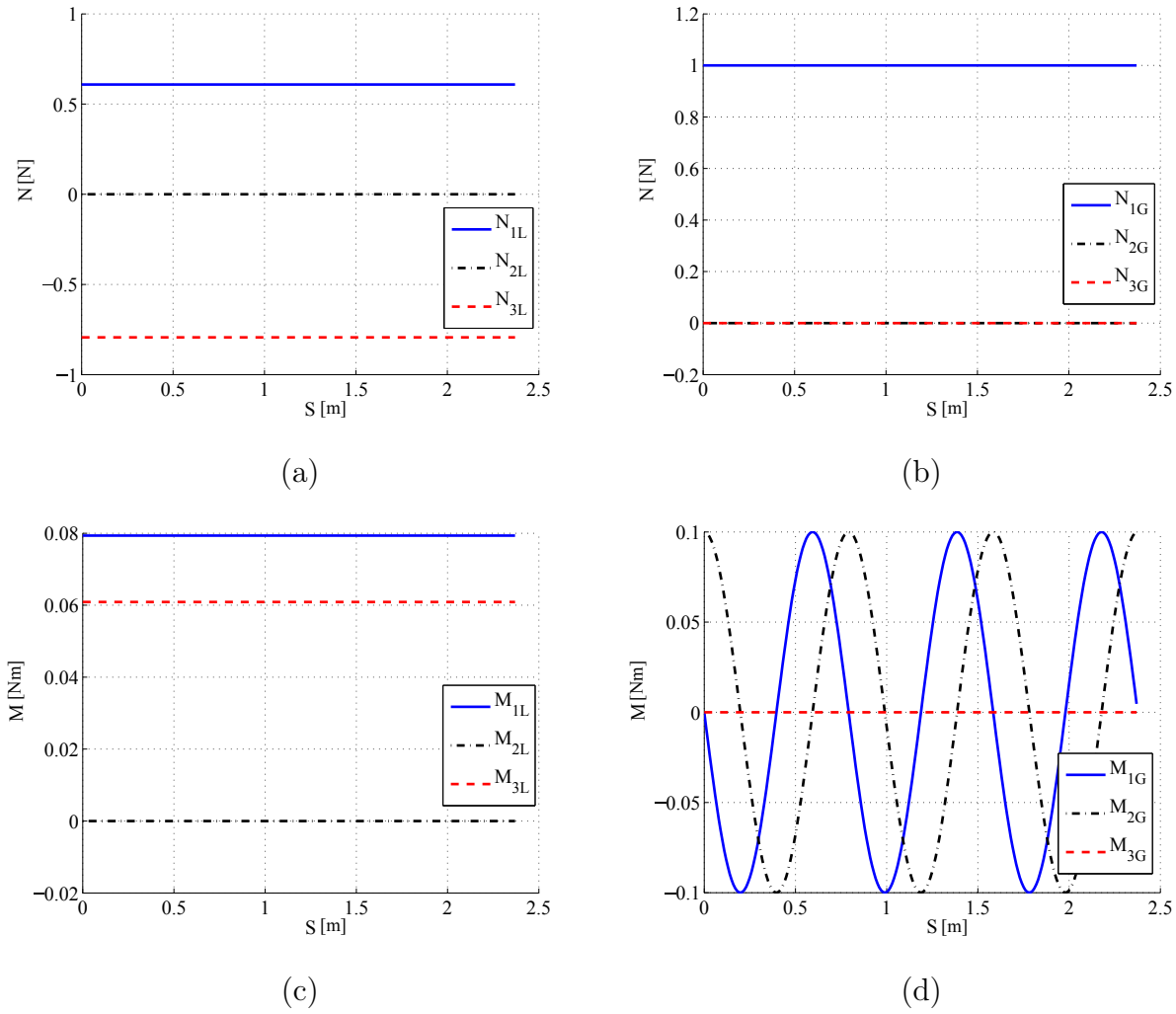

Figure 5.20 – Force diagram (a) local and (b) global for a tensile load and moments (c) local and (d) global.

$$\xi = \frac{2C_d(4C_d + 2)}{(4C_d - 3)(2C_d - 1)}, \tag{5.31}$$

and C_d is the relation between diameters, i.e., $C_d = \dfrac{Di}{d}$. For the geometry used in this case, $C_d = 10$ and the stress is calculated as $\sigma_{sh} = 76068.36\ Pa$.

With the present methodology applied, the stress was 77509.91 Pa for the same analysis. Three turns were considered to obtain the results, however, using larger or smaller length to represent the spring would not affect it. Since the local moments are constants, in this case, so is the stress.

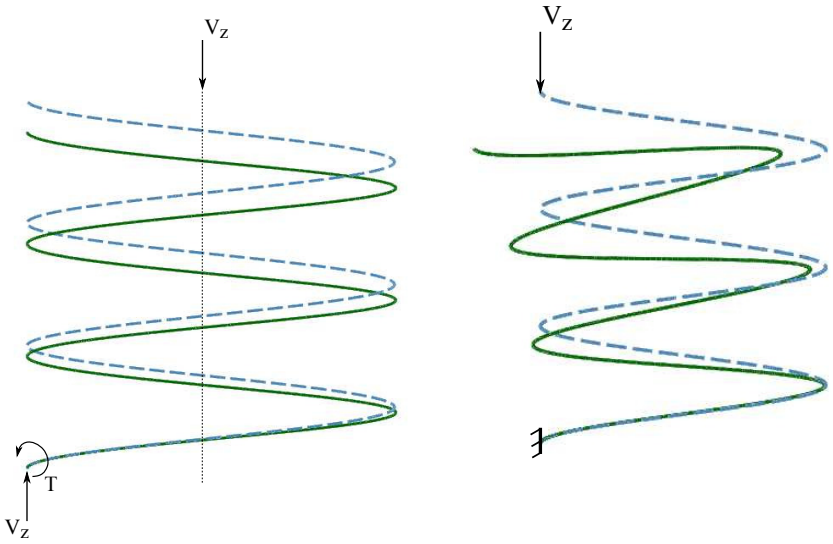

(a) (b)

Figure 5.21 – Deformed (solid line) and undeformed (dashed line) spring considering a load (a) applied in the axis center and (b) at the free end in the helix.

Figure 5.21 (a) shows the deformed shape (dashed line) for the case of a load applied over the helix axis. An amplification factor of five times was used to allow better visualization. As expected, the u_3 component is larger than the other components.

Figure 5.21 (b) shows the counterpart when the load is applied at the free end of the coil. The clamped-free boundary conditions make the bending behavior of the spring more conspicuous than in the pure compression case. Hence, not only u_3 is a noticeable component,but also u_1 and u_2 as already demonstrated in Figure 5.13 (c)

Local and global effects were analyzed for different cases. More spring turns also were explored in this section and presented periodic results or a predicted growth. Other interesting effects are presented in the next section.

5.6 Periodicity

As mentioned previously, the presented structure was analyzed with only one turn. The effects are expected to be repeated when θ (Equation 2.19) reaches values higher than 2π. Five turns were simulated and the results are plotted in Figure 5.22, for bending and tensile loads applied together.

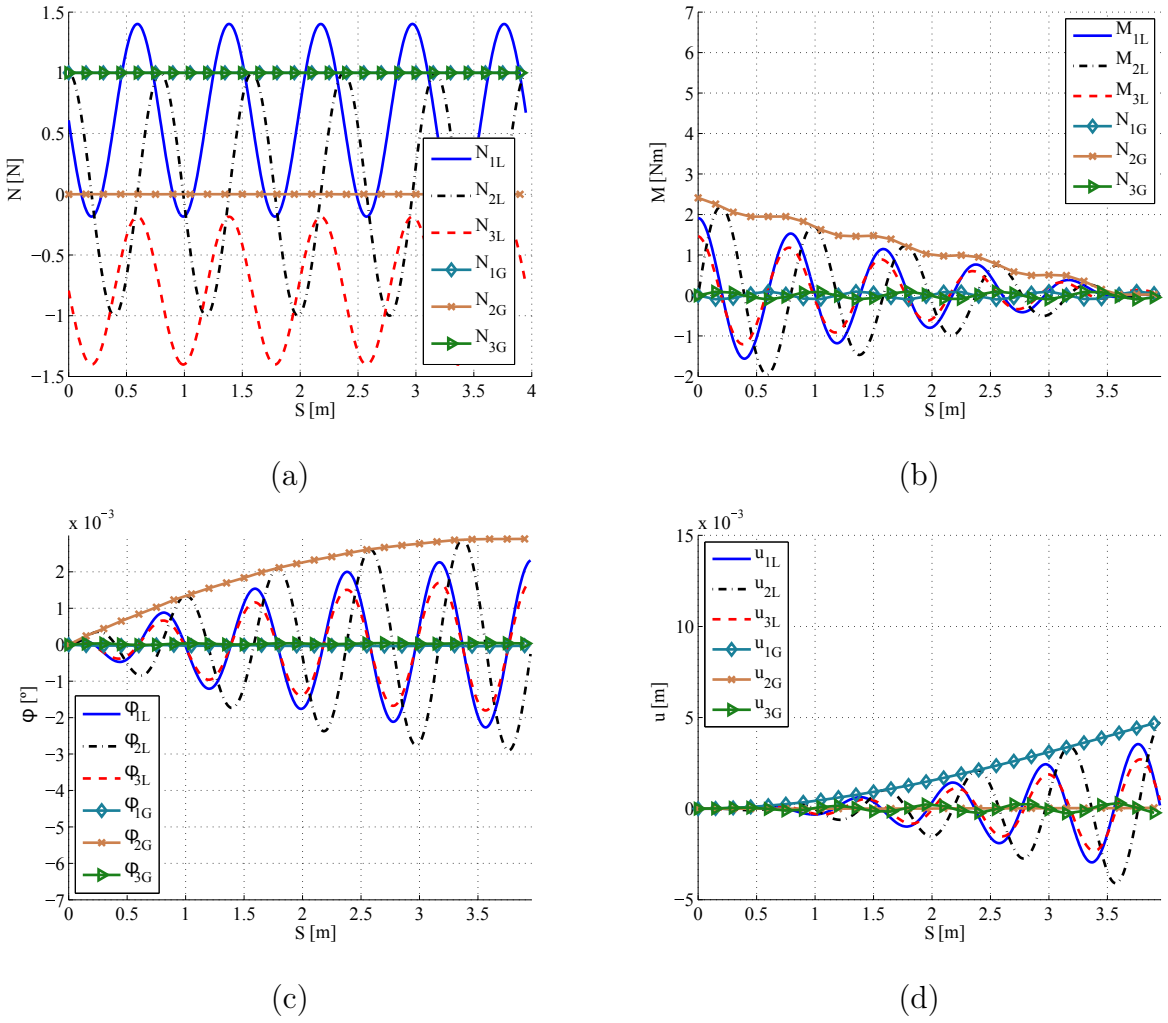

Figure 5.22 – Global and local effects considering V_x and V_z applied together for (a) forces, (b) moments, (c) rotations and (d) displacements.

As expected, the tensile effects are periodic (Figure 5.22 (a)). The consideration of more than one turn is irrelevant in the analysis. However, the bending effect produces components that increase with the structure which is explained by the distance between the applied load and the clamped end.

As it can be seen, the response from the local system is contained in the global. The global system involves the local effects, so that the higher values determined in the local basis are equal to the global ones and the

Figure 5.22 (a) represents the forces and although the local values are not explicit contained, the vector sum resultant must be observed, so that this property is observed.

An offspring result observed in Figure 5.22 is the envelope curves for forces and displacements. Apparently, these envelopes are not reported in the machine element literature, and their importance is related to the possibility of applying them as an aid to the designer. Once obtained, these curves can be used to retrieve the maximum values for a given number of twists, and allow for overall stiffness/flexibility and/or safety margin dimensioning.

Interestingly enough, these envelopes are not "*contaminated*" by the oscillatory behavior of the trigonometric functions presented in the individual components of forces and displacements.

6. FINAL REMARKS

The final remarks are exposed in this final chapter. The results conclusions are presented considering the proposed model. Also a verification of the objectives and suggestions for further analysis, considering the model upgrade, are introduced.

6.1 Conclusions

A mathematical model was proposed to obtain the mechanical response of a curved beam . Some simplifications were explored, were the wire was parameterized, by its center line, as an helix as in cable strands.

To explore the local and/or global results the Frenet-Serret triad was used along the parametric coordinate. A transformation matrix was defined and allowed the change in the coordinate system. Geometrical properties as curvature and torsion were also determined using differential geometry.

The differential equilibrium equations of forces and moments were determined. After applying the boundary conditions, geometry and constitutive relations, the strains and stresses expressions were also obtained.

Using the Principle of Virtual Work the equilibrium differential equations for rotations and displacements were determined. This system was also solved to produce results regarding the strand behavior.

The results were compared to numerical solutions from the Finite Element Method, showing good agreement. The validation concerning bending and tensile load was verified and a methodology to characterize the mechanical behavior of helical structures was presented.

6.2 Future Research

The proposed is not complete and must be further developed. Among the research developments which can follow from the present work, it is worthy to mention:

- Distributed loads were considered and could provide a mechanism to include contact between strand or from strand core;

- Different parametrizations to represent another geometry, since cables presents an enormous range of options, could be introduced. This means that the parameters curvature and torsion, here considered constants, could be presented as a function of S;
- Extend the formulation to constitutive relations other than the isotropic, in particular transversally isotropic material which is commonly used to model cables;
- Multi-layered cables are structures commonly used and could be analyzed in further research as well;
- To study the dynamic behavior of spatially oriented curved beams.

BIBLIOGRAPHICAL REFERENCES

ANSYS, R. **ANSYS Mechanical APDL Product Release 13.0**. Ansys Inc, Canonsburg, Pennsylvania, 2012.

Argatov, I. Response of a wire rope strand to axial and torsional loads: Asymptotic modeling of the effect of interwire contact deformations, **International Journal of Solids and Structures**, vol. 48(10), p. 1413–1423, 2011.

Bathe, K.-J.; Bolourchi, S. Large displacement analysis of three-dimensional beam structures, **International Journal for Numerical Methods in Engineering**, vol. 14(7), p. 961–986, 1979.

Cardou, A.; Jolicoeur, C. Mechanical models of helical strands, **Applied Mechanics Reviews**, vol. 50, p. 1–14, 1997.

Costello, G. Stresses in multilayered cables, **Journal of Energy Resources Technology**, vol. 105(3), p. 337–340, 1983.

Costello, G. A.; Phillips, J. W. Static response of stranded wire helical springs, **International Journal of Mechanical Sciences**, vol. 21(3), p. 171–178, 1979.

Do Carmo, M. P. **Differential geometry of curves and surfaces**. volume 2. Prentice-hall Englewood Cliffs, 1976.

Elata, D.; Eshkenazy, R.; Weiss, M. The mechanical behavior of a wire rope with an independent wire rope core, **International Journal of Solids and Structures**, vol. 41(5), p. 1157–1172, 2004.

Feyrer, K. **Wire ropes**. Springer, 2007.

Frikha, A.; Cartraud, P.; Treyssede, F. Mechanical modeling of helical structures accounting for translational invariance. Part 1: Static behavior, **International Journal of Solids and Structures**, vol. 50(9), p. 1373–1382, 2013.

Ghoreishi, S. R.; Cartraud, P.; Davies, P.; Messager, T. Analytical modeling of synthetic fiber ropes subjected to axial loads. Part I: A new continuum model for multilayered fibrous structures, **International Journal of Solids and Structures**, vol. 44(9), p. 2924–2942, 2007a.

Ghoreishi, S. R.; Messager, T.; Cartraud, P.; Davies, P. Validity and limitations of linear analytical models for steel wire strands under axial loading, using a 3D FE model, **International Journal of Mechanical Sciences**, vol. 49(11), p. 1251–1261, 2007b.

Jiang, W.; Yao, M.; Walton, J. M. A concise finite element model for simple straight wire rope strand, **International Journal of Mechanical Sciences**, vol. 41(2), p. 143–161, 1999.

Jiang, W.-G. A concise finite element model for pure bending analysis of simple wire strand, **International Journal of Mechanical Sciences**, vol. 54(1), p. 69–73, 2012.

Jiang, W.-G.; Warby, M. K.; Henshall, J. L. Statically indeterminate contacts in axially loaded wire strand, **European Journal of Mechanics-A/Solids**, vol. 27(1), p. 69–78, 2008.

Kobayashi, S.; Nomizu, K. **Foundations of differential geometry**. volume 1. New York, 1963.

Kreyszig, E. **Introduction to differential geometry and Riemannian geometry**. volume 16. University of Toronto Press, 1968.

Labrosse, M.; Nawrocki, A.; Conway, T. Frictional dissipation in axially loaded simple straight strands, **Journal of Engineering Mechanics**, vol. 126(6), p. 641–646, 2000.

Lee, W. An insight into wire rope geometry, **International journal of solids and structures**, vol. 28(4), p. 471–490, 1991.

Love, A. E. H. **A treatise on the mathematical theory of elasticity**. volume 1. Cambridge University Press, 2013.

Luongo, A.; Zulli, D. **Mathematical models of beams and cables**. John Wiley & Sons, 2013.

Nawrocki, A.; Labrosse, M. A finite element model for simple straight wire rope strands, **Computers & Structures**, vol. 77(4), p. 345–359, 2000.

Østergaard, N. H.; Lyckegaard, A.; Andreasen, J. H. A method for prediction of the equilibrium state of a long and slender wire on a frictionless toroid applied for analysis of flexible pipe structures, **Engineering Structures**, vol. 34, p. 391–399, 2012.

Páczelt, I.; Beleznai, R. Nonlinear contact-theory for analysis of wire rope strand using high-order approximation in the FEM, **Computers & Structures**, vol. 89(11), p. 1004–1025, 2011.

Pan, N. Development of a constitutive theory for short fiber yarns: Mechanics of staple yarn without slippage effect, **Textile research journal**, vol. 62(12), p. 749–765, 1992.

Pidaparti, R.; Jayanti, S.; Henkle, J.; El-Mounayri, H. Design simulation of twisted cord–rubber structure using ProE/ANSYS, **Composite structures**, vol. 52(3), p. 287–294, 2001.

Pressley, A. N. **Elementary differential geometry**. Springer Science & Business Media, 2010.

Ramsey, H. A theory of thin rods with application to helical constituent wires in cables, **International journal of mechanical sciences**, vol. 30(8), p. 559–570, 1988.

Ramsey, H. Analysis of interwire friction in multilayered cables under uniform extension and twisting, **International Journal of Mechanical Sciences**, vol. 32(8), p. 709–716, 1990.

Raoof, M. Free bending of spiral strands, **Journal of engineering mechanics**, vol. 116(3), p. 512–530, 1990.

Shigley, J. E.; Mischke, C. R.; Budynas, R. G. **Mechanical engineering design**. McGraw-Hill,, 2004.

Spillers, W. R.; Eich, E. D.; Greenwood, A. N.; Eaton, R. A helical tape on cylinder subjected to bending, **Journal of Engineering Mechanics**, vol. 109(4), p. 1124–1133, 1983.

Stanova, E.; Fedorko, G.; Fabian, M.; Kmet, S. Computer modelling of wire strands and ropes part II: Finite element-based applications, **Advances in Engineering Software**, vol. 42(6), p. 322–331, 2011.

Treyssède, F.; Frikha, A.; Cartraud, P. Mechanical modeling of helical structures accounting for translational invariance. Part 2: Guided wave propagation under axial loads, **International Journal of Solids and Structures**, vol. 50(9), p. 1383–1393, 2013.

Usabiaga, H.; Pagalday, J. Analytical procedure for modelling recursively and wire by wire stranded ropes subjected to traction and torsion loads, **International Journal of Solids and Structures**, vol. 45(21), p. 5503–5520, 2008.

Utting, W.; Jones, N. Tensile testing of a wire rope strand, **The Journal of Strain Analysis for Engineering Design**, vol. 20(3), p. 151–164, 1985.

Utting, W.; Jones, N. The response of wire rope strands to axial tensile loads—Part I. Experimental results and theoretical predictions, **International journal of mechanical sciences**, vol. 29(9), p. 605–619, 1987.

Velinsky, S. General nonlinear theory for complex wire rope, **International journal of mechanical sciences**, vol. 27(7), p. 497–507, 1985.

Zhu, L.-l.; Zhao, Y.-h. Exact solution for warping of spatial curved beams in natural coordinates, **Applied Mathematics and Mechanics**, vol. 29, p. 933–941, 2008.